Numerical Modeling of Hydrogen Ion Sources with the Radio Frequency Inductively Coupled Plasma

February 2018

Kenjiro Nishida

Numerical Modeling of Hydrogen Ion Sources with the Radio Frequency Inductively Coupled Plasma

by

Kenjiro Nishida

Supervisor: Prof. Akiyoshi Hatayama

Keio University

1858

CALAMVS GLADIO FORTIOR

Graduate School of Science and Technology

Keio University

A thesis submitted for the degree of
Doctor of Philosophy in Engineering

February 2018

Contents

List of Figures

List of Tables

Chapter 1

Introduction

The Radio Frequency (RF) Inductively Coupled Plasma (ICP) has long been utilized for ion sources in a wide range of fields. Despite its high versatility, the discharge process of the RF-ICP is so complex that it has been of scientific interest since it was generated for the first time more than 100 years ago. In this chapter, we briefly describe the physical property of the RF-ICP, some examples and issues of the RF-ICP application. The purpose of our study is also summarized in the last section in this chapter.

1.1 Physical Property of the RF-ICP

1.1.1 Typical geometries of RF discharges

As the name implies, the RF-ICP discharge is generated by electromagnetic induction made by an RF antenna adjacent to (or immersed in) its discharge region. There are several types of RF-ICP generator, which are reviewed in Ref. [1]:

- cylindrical discharge by a solenoid antenna,
- planar discharge by a spiral antenna,
- cylindrical/planar discharge by an immersed antenna.

The cylindrical discharge generated by a non-immersed solenoid antenna is presented here as an example.

Figure 1.1 shows the simplest form of the cylindrical RF-ICP generator. Fundamental equipments of the system are a discharge chamber filled by a gas, a solenoid antenna surrounds the chamber, an RF power source and a matching box inserted between the power source and the antenna.

The gas contained within the discharge chamber is ionized by the electric power delivered by the surrounding antenna current whose frequency is in an RF range. The discharge cham-
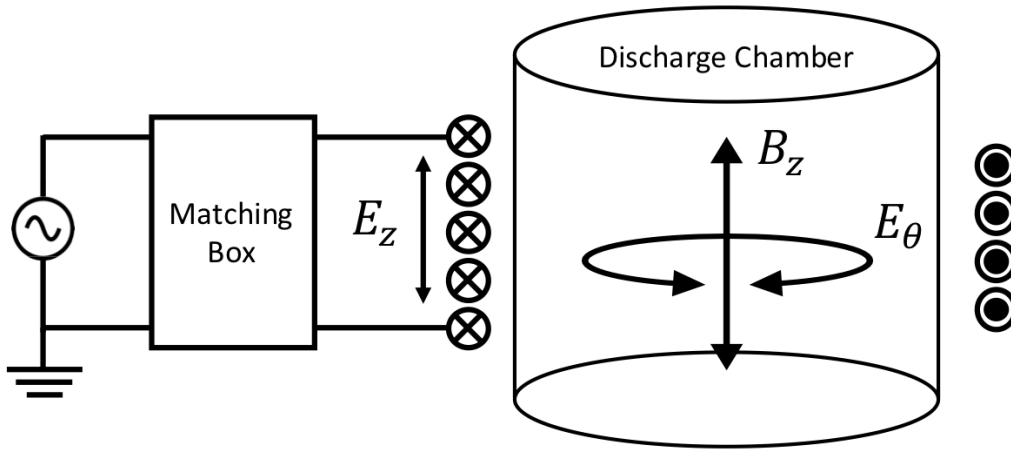
Fig. 1.1   Schematic view of a cylindrical RF-ICP discharge. This is a simplest version of the cylindrical discharge that is composed of only fundamental equipments. The discharge is sustained by the electromagnetic induction generated by the antenna adjacent to the discharge chamber.

ber is usually made of dielectric material in order to let the power, which is delivered in terms of electromagnetic wave, penetrate the discharge region.

The RF antenna current generates the axial magnetic field and the resultant azimuthal electric field (B_z and E_θ in Fig. 1.1, respectively) in accordance with the Maxwell-Faraday equation,

$$\nabla \times \mathbf{E} = -\frac{\partial \mathbf{B}}{\partial t}. \tag{1.1}$$

 Most of the electric power is coupled to electrons in the chamber because the other particles are too heavy to respond to the electromagnetic field in an RF time scale. The electrons, which are accelerated by the electric field, experience collisions with neutrals in the gas and some of them ionize the neutrals. Each ionization yields the secondary electron so that the electron density exponentially increases when the ionizations sufficiently occur. The reaction rate of the ionization and the electric field coupled to the electrons are then the key parameters which determine the plasma density. As this process is sustained by the circular inductive field, this RF-ICP discharge is usually referred to as ring discharge.

As the large amount of the RF power is delivered to the antenna and the plasma, one can expect that the high voltage is applied to the solenoid antenna. The high voltage applied to the antenna yields the electrostatic field along the antenna (E_z in Fig. 1.1), and this electric field also contributes to the RF-ICP discharge, which will be described in Section 1.1.2. Some RF-ICP generators employ a Faraday shield between the chamber wall and the solenoid antenna in order to mitigate the electrostatic field and to make the pure inductive discharge.

The amount of the RF power is an important parameter which determines the plasma density as mentioned above. The matching box inserted between the RF power source and the antenna, plays an important role in optimizing the power transfer efficiency. However, proper design for the efficient power transfer cannot readily be done because the RF-ICP acts as a variable load whose behavior is too complex to be predicted in advance. In Section 1.1.3, we describe the issues of the power transfer to the RF-ICP.

1.1.2   RF discharge modes

Since the electrode-less discharge was invented, it had been a controversial issue, whether the discharge is sustained by the inductive field E_θ or the electrostatic field E_z (see Fig. 1.1). Nowadays, it is widely known that either of the inductive or electrostatic fields can be the dominant one that sustains the discharge, which was noticed by Mackinnon for the first time [2]. The two different discharge modes are called E-mode and H-mode [3, 4]: The former is sustained by the electrostatic field, and the latter is done by the inductive field.

The E-mode exhibits when the plasma is operated in a low plasma density regime. The electrostatic field forces the charged particles within the plasma to move back and forth between the antenna edges, which makes the dynamics of the plasma similar to that of the plasma between the parallel capacitors. The field is therefore referred to as the capacitive field. As the origin of the field is the electrostatic potential, it can readily be reduced or eliminated by a conductive material (e.g., Faraday shield). The plasma itself also screens out the field by the Debye shielding, as the plasma density increases so that the inductive field (H-mode) dominates the discharge in turn. The electric fields inside RF antennae (the capacitive against the inductive) have been investigated in Refs. [5–7].

As described above, the operational plasma density determines the dominant discharge mode. Therefore, the discharge mode transition between the E- and H-mode has frequently been observed in one operation. The transition usually makes the RF-ICP more difficult to handle as the dynamics of the plasma changes largely in response to the transition. In order to obtain insight into such complex discharge process, numerous studies have been carried out [8–21].

For example, it is well known that the RF-ICP discharge exhibits a hysteresis phenomenon during the mode transition, and it has been actively investigated [11,13,17]. Figure 1.2 shows the hysteresis of an argon RF-ICP: the emission from the argon 419.8 and 420.0 nm lines, which corresponds roughly to the plasma density, has been measured as a function of the RF input current. When the RF current is increased in order to change the discharge mode from E- to H-mode, a sudden jump of the plasma density is observed when the current exceeds about 3.5 A while the sudden jump during the H- to E-mode transition does not occur at the
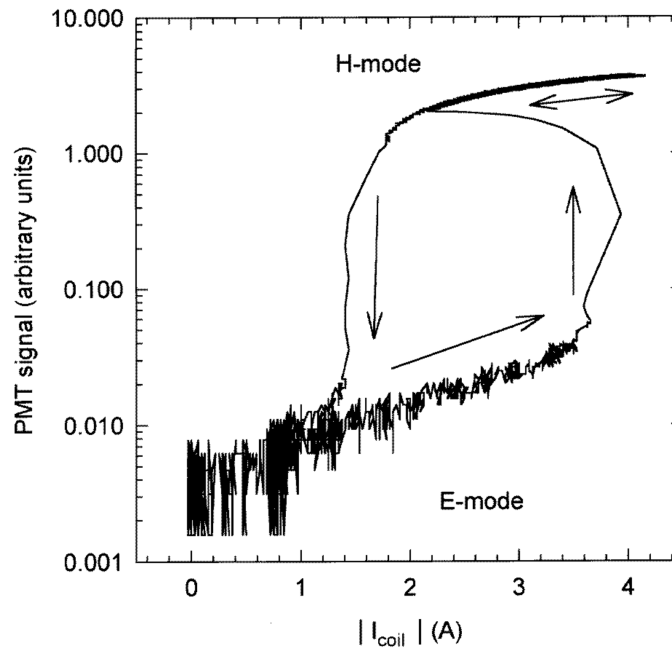
Fig. 1.2   Emission from the argon 419.8 and 420.0 nm lines during a transition from the E-mode to the H-mode in a pure argon discharge at 0.1 Torr as a function of the RF coil current amplitude. The arrows denote the time evolution of the trace, starting from the E-mode at low RF coil currents [11].

same point but the lower current, about 1.8 A. This investigation is important in order to find the minimum current which is required to operate the plasma in the high density regime, the H-mode. Not only the hysteresis phenomenon, but also instability of the plasma during the transition (for electronegative plasmas, especially) has been reported and investigated [10].

The RF-ICP discharge is usually accompanied by non-equilibrium phenomena. For example, the plasma does not reach to a thermal equilibrium state in the low pressure regime. In addition, plasma sheath is of importance to investigate the dynamics of the ions because ions obtain the direct kinetic energy easily by the sheath acceleration. These non-equilibrium phenomena are difficult to analyze by conventional theoretical approaches or fluid models, and most of the relating parameters are laborious to obtain by experimental methods. Although it is desirable to understand the non-equilibrium features of the RF-ICP, especially during the mode transition, it has not been studied well from a kinetic point of view.

1.1.3   Power transfer to the RF-ICP

In the RF system that includes the RF-ICP as a load, the power transfer efficiency tends to be an issue for the operation of the system. As mentioned in Section 1.1.1, the matching box inserted between the power source and the antenna (see Fig. 1.1 again) plays an important

role in improving the power transfer efficiency.

The RF power is properly sent from the power source to the load only when all the equipments installed in the system have the same impedance (the most standard value is 50 Ω). Otherwise, a portion of the RF power is reflected back so that one might end up failing to ignite the RF-ICP in the worst case. The mathematical description of the power reflection due to the impedance mismatch is provided in Chapter 2.

Since the antenna and the RF-ICP inside the chamber almost never be a 50 Ω load by themselves, the matching box is inserted before the load so that they play as a 50 Ω load in total. The matching box is usually an LC circuit which comprises a combination of a few inductances and capacitances, which is tuned to resonate in the operational frequency range. Although the matching box is to be designed properly, an optimum design is difficult to define when the system includes the RF-ICP as a load. It is because the estimation of the impedance of the RF-ICP is not easy even when all the discharge parameters are given. In addition, those parameters are time-varying parameters so that the plasma impedance also changes in time.

Basically, impedance of a circuit element can be defined when one can estimate the power dissipation and the stored electromagnetic energy of the element, which represent the real and imaginary part of the impedance, respectively. Some theoretical approaches model the RF-ICP as a lumped circuit element (a 0D model) and estimate the impedance assuming that the plasma is a conductive material whose permittivity ε_p is constant with respect to time and space. The assumption makes it easy to calculate the electromagnetic field inside the RF-ICP so that one can estimate the stored and dissipated power. Such a 0D approach is useful for the qualitative analysis of the RF system including the plasma as a load.

As we mentioned in the previous section, the microscopic approach is mandatory to discuss the power transfer to the RF-ICP in detail because the behavior of the actual RF-ICP is too complex to be predicted by simple theoretical approaches. In particular, there are few methods that are able to analyze the power transfer while taking into account the complex RF-ICP discharge processes, e.g., E-H discharge mode transition, kinetic behaviors of the RF-ICP. Those phenomena are closely related to the power dissipation of the plasma and cannot be taken into account in the absence of the microscopic perspective. On the other hand, it is also important to notice that a sophisticated method that is able to analyze such complex phenomena tends to be a time-and-labor-consuming process. Hence not only the microscopic approach but also the macroscopic approach is mandatory in order to contribute to the development of the RF system that includes the RF-ICP.

1.2   Hydrogen Ion Source for Particle Accelerator

1.2.1   CERN

The European Organization for Nuclear Research (CERN: Conseil Européen pour la Recherche Nucléaire) is a leading research institute for particle physics. Their research activity is dedicated to clarifying the fundamental constituent of matter. The basic concept of their research is to observe the collision reaction between two proton beams that are accelerated close to the light speed. The proton beams with the extraordinary speed are obtained by using the CERN's accelerator complex (shown in Fig. 1.3), whose scale is the largest in the world. The acceleration is done by the following accelerators:

1. Linac2: Protons are obtained/extracted from the *hydrogen ion source* and accelerated to 50 MeV, which is described more in detail in the next section.
2. Proton Synchrotron Booster (PSB): 1.4 GeV acceleration of the proton beams injected from Linac2.
3. Proton Synchrotron (PS): 25 GeV acceleration. This instrument is capable of the acceleration of either protons from the PSB or heavy ions from the Low Energy Ion Ring (LEIR).
4. Super Proton Synchrotron (SPS): This is the second largest accelerator in CERN's accelerator complex and is capable of accelerating up to 450 GeV. Not only the protons but also the different type of the particles are handled by this instrument, e.g., electron, positron, antiproton, etc.
5. Super Proton Synchrotron (SPS): generates 450 GeV proton beams from the ones supplied from PS.
6. Large Hadron Collider (LHC): This world's largest accelerator accelerates the proton beams to 7 TeV, where the beams are split into two. One is delivered in the clockwise direction and the other is done in the opposite direction so that they collide with each other.

The experiment carried out at LHC is indispensable for modern particle physics research, one of which leads to the discovery of Higgs boson. It is therefore desirable to improve the CERN's experiment for the further progress of particle physics. The hydrogen ion source, which is the very beginning stage for the proton beams, is one of the key components for the further improvement of the CERN's accelerator complex.
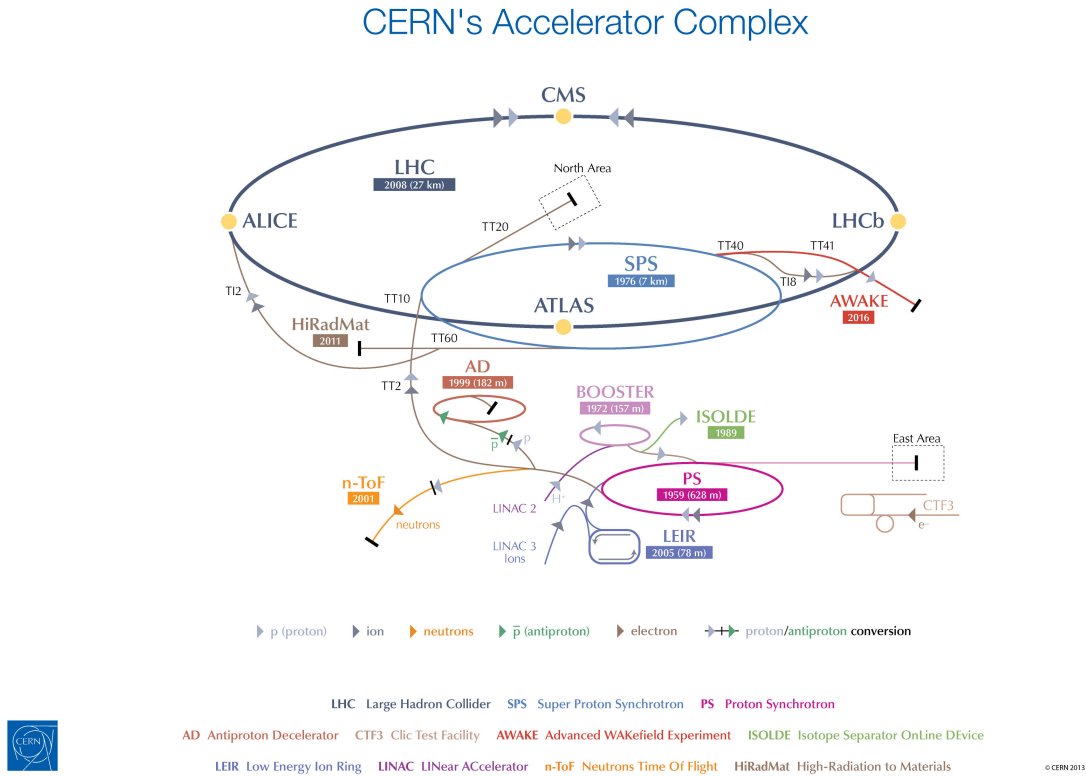
Fig. 1.3   Schematic drawing of CERN's accelerator complex [22].

1.2.2   CERN's Linac4 and H⁻ ion source

The linear accelerator is the first stage of the particle acceleration. Its reliability must be the highest in all other accelerators because a fault of the linear accelerator leads to shutdown of the whole accelerator complex. The present CERN's accelerator complex employs Linac2 (linac is named after the acronym of linear accelerator) as a particle injector. The Linac2 extracts protons from its hydrogen ion source, and they are accelerated up to 50 MeV.

Aiming to deliver a higher energy beam, CERN has decided to develop a new linear accelerator Linac4 [23], which shall replace Linac2. The replacement is desirable also because of its obsolete design. Some components of the Linac2 have already gone out of production.

The schematic of the Linac4 is shown in Fig. 1.4. In contrast to the Linac2, the Linac4 handles negative hydrogen (H⁻). The H⁻ ions are extracted as a beam from the H⁻ source and will be injected to Low-Energy Beam Transport (LEBT) line. The beam will be accelerated to 3 MeV at Radio Frequency Quadrupole (RFQ) located after LEBT line. The beam is separated into several bunches in the chopper line. Those bunches are injected to PSB after being accelerated to 160 MeV by Drift Tube Linac (DTL), Coupled DTL (CDTL) and Side
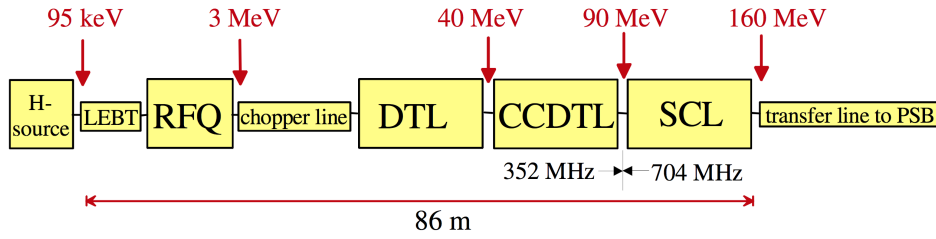
Fig. 1.4   Schematic drawing of Linac4 [23].

Coupled Linac (SCL).

1.2.3   Linac4 H^- source and H^- production

The Linac4 H^- source, shown in Fig. 1.5, is designed to produce a 50 mA, 45 keV H^- beam within the transverse RMS emittance of 0.25 π·mm·mrad that is the RFQ acceptance [24–27]. The plasma chamber of the Linac4 H^- source is surrounded by solenoid antenna, and the plasma is heated by a 100 kW, 2 MHz, 10% bandwidth RF system.

The processes of H^- production are categorized into two; volume production and surface production. The volume-produced H^- requires following two reactions:

$$H_2(\nu) + e_{high} \rightarrow H_2(\nu') + e_{high}, \tag{1.2}$$

$$H_2(\nu') + e_{low} \rightarrow H^- + H. \tag{1.3}$$
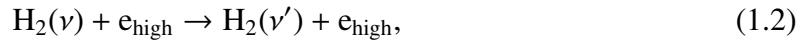
The hydrogen molecule H_2 experiences the collision with fast electrons and will be in a vibrationally exited state as shown in the first reaction (1.2). On the other hand, low energy electrons are also important for the production of H^- by the reaction (1.3), the dissociative attachment process.

The Linac4 H^- source mainly uses on the surface-produced H^-, which is produced by the bombardment on the low work function metal surface (the cesiated molybdenum electrode, Cs-Mo shown in Fig. 1.5) by H, H^+ or H_2^+:

$$H, H^+ \text{or } H_2^+ + (wall) \rightarrow H^-. \tag{1.4}$$

These heavy particles, which are related to the surface-production of H^-, are produced from the following reactions;

$$H + e_1 \rightarrow H^+ + e_1 + e_2, \tag{1.5}$$

$$H_2 + e_1 \rightarrow H_2^+ + e_1 + e_2, \tag{1.6}$$
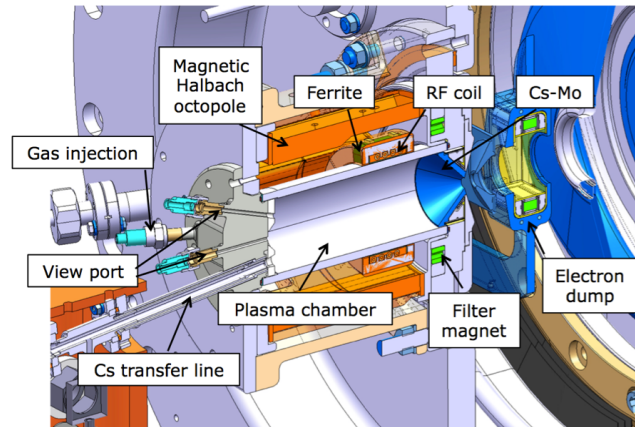
Fig. 1.5   Schematic drawing of the Linac4 H$^-$ source.

$$H_2 + e \rightarrow H + H + e, \tag{1.7}$$

$$H_2^+ + e \rightarrow H^+ + H + e. \tag{1.8}$$

The point here is that the electron is of importance for both the volume- and surface-produced H$^-$. The behavior of the electron during the discharge (shown in Fig. 1.6) is therefore to be investigated.

As the RF power coupled to the H$^-$ source plasma is dominantly consumed by the electrons, the power transfer efficiency between the RF generator and the plasma plays an important role in controlling the electron and also the production of H$^-$ consequently. It has been indicated that the extracted H$^-$ current is proportional to the RF power coupled to the plasma in Ref. [28].

As we have discussed in Section 1.1.3, however, the control of the power transfer efficiency is not an easy issue because the system includes the RF-ICP which acts as a time-varying load. In the previous work at CERN, it has been shown that the tuning of RF frequency dynamically (within the range of 1.9 - 2.1 MHz) during the discharge is useful to cope with the improvement of RF-coupling to the plasma [29]. The tuning is by now automatized. However, the complex relation between the power transfer efficiency, discharge parameters, hydrogen pressure and plasma impedance deserves further investigation.

1.2.4   Other applications of the RF-ICP

Originally, the RF-ICP discharge under high gas pressure condition has long been investigated for the applications such as spectra-chemical analysis, plasma-aided chemical synthesis, and so on [30]. The interest in the RF-ICP discharge was renewed several decades ago as the low pressure ICP started to attract the researchers attention. The advantage of the
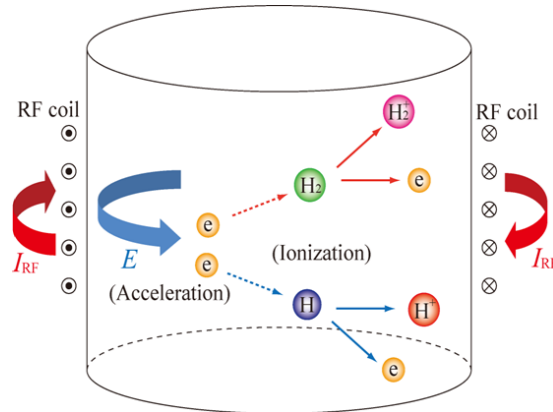
Fig. 1.6   Acceleration of electron.

low pressure ICP discharge is the independent control of the ion energy and the plasma density [4]. Such ion sources with the low pressure RF-ICP are applied to the industrial field such as plasma-aided manufacturing of integrated circuits [1].

Recently, the importance of the low pressure RF-ICP has been getting noticed again in other fields because of the increasing demand of RF driven type H$^-$ sources. They are applied not only to accelerators of high energy particle physics, which we mentioned in the previous sections, but also to the heating of magnetically confined fusion plasmas [31–35].

The RF driven type H$^-$ source is an important component in the Neutral Beam Injection (NBI) system, which is for the heating of the fusion plasmas. The H$^-$ beam extracted from the source is neutralized after the sufficient acceleration. The highly accelerated neutral beams are injected into the fusion plasma as an energy input. The NBI systems for ITER [36], the world's largest fusion experiment, are required to produce a 1 MeV neutral beams by each.

It has been decided to use the RF driven type H$^-$ source as it is required to provide high energy/density H$^-$ beam with less maintenance. The RF driven type H$^-$ source requires less maintenance than conventional ion sources because it does not use any filament to ignite the plasma. The filaments get damaged easily, especially when the ion source is operated with the high electric power to produce high dense plasma, and exchange of filaments tends to be a time-and-labor-consuming process.

Figure 1.7 shows the H$^-$ source which is developed at Max-Planck Institute for Plasma Physics (IPP). The H$^-$ source is dedicated to the study on the ion source development for the ITER NBI. The RF system of the H$^-$ source delivers a 150 kW RF power at 1 MHz. The IPP H$^-$ source is composed of three parts; the driver region, where the RF-ICP is generated, the expansion region and the extraction region. The latter two is magnetically separated in order to filter electrons and to extract H$^-$ only.

As the H$^-$ source for the ITER NBI are required to be delivered a high density H$^-$ beam
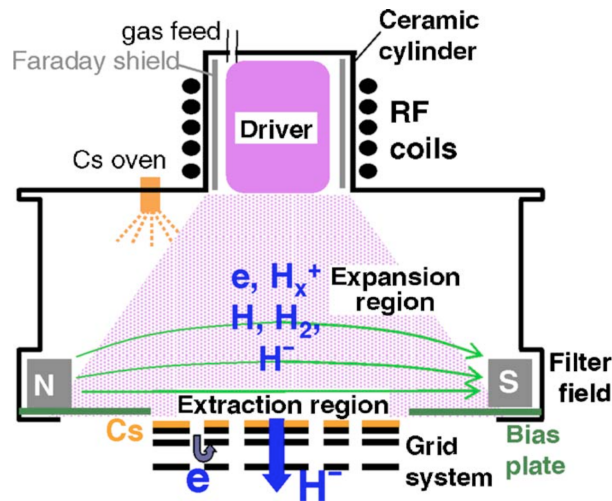
Fig. 1.7   Schematic drawing of the standard size IPP rf source [33].

under a long-pulse operation, the efficiency of the power transfer to the plasma and its relia-bility are severe issues. The IPP R&D, which is dedicated to the improvement of the power coupling efficiency, is summarized in Ref. [35], and still on-going.

1.3   Purpose of the Thesis

In this thesis, our numerical studies on the hydrogen ion sources with the RF-ICP are pre-sented. Those studies have been carried out with an attempt to obtain insight into the oper-ation of the RF-ICP. In particular, we have studied the RF-ICP from 1. macroscopic and 2. microscopic points of view:

1. An equivalent circuit model of the RF-ICP

    The power transfer to the RF-ICP is one of the key parameters for the operation of the hydrogen ion sources. The optimization of the power transfer cannot readily be achieved because the RF-ICP acts as a variable electrical circuit in the RF system. By using a 0D equivalent circuit model of the RF-ICP, we have investigated the optimiza-tion of the power transfer to the RF-ICP.

2. Particle-based modeling of the RF-ICP discharge

    A particle-based model of the RF-ICP has been developed in order to analyze its discharge process from a kinetic point of view. The model is able to analyze the discharge mode transition between the E- and H-modes, where the physical property of the RF-ICP suddenly changes. We discuss the kinetic behavior of the RF-ICP during

the mode transition, which is too complex to investigate by conventional fluid models.

This thesis is organized as follows:

Chapter 1 is an introduction of this thesis. The purpose and the aim of this study have been described with the brief summary of the physics of the RF-ICP discharges, applications and issues of RF-ICPs.

In Chapter 2, the equivalent circuit model of the RF-ICP will be explained, which has been developed for the study on impedance matching. This model describes RF-ICP inside the ion source and the matching network including the external coil which surrounds the plasma chamber. All the elements have been modeled as lumped elements, which means this model is based on the 0D model. By using this model, optimization of the power transfer and impedance matching between the RF system and the RF-ICP has been investigated.

In Chapter 3, the analysis of the impedance matching in the RF system of the hydrogen ion source of CERN's linear accelerator, LINAC4, will be given by using the model introduced in Chapter 2. From the results, it has been confirmed that the control of the RF signal frequency is useful to increase the efficiency of the power transfer to the RF-ICP, which have empirically been found in the experiment carried out at CERN.

In Chapter 4, the numerical model of the hydrogen RF-ICP discharge will be described. The model is based on the EM Particle In Cell (PIC) method, whose governing equations are Maxwell's equations and the equation of motion for the charged particles. This model is superior to conventional fluid or other simple numerical models of RF discharge: particle-based modeling enables the model to analyze the discharge process from a kinetic point of view. The RF-ICP has hardly been studied by such a kinetic model so far.

In Chapter 5, the discharge process of hydrogen RF-ICP will be numerically analyzed by using the model introduced in Chapter 4. It has been confirmed that the model is able to reproduce the E-to-H discharge mode transition. In addition, Energy Distribution Functions (EDFs) of electron and ions is analyzed from a kinetic view of point. The EDFs deviate from the Maxwell distribution in the thermal equilibrium. This indicates the importance of the kinetic perspective to investigate the RF-ICP discharge. It is expected that this model enables us to calculate the impedance of RF-ICP with the non-equilibrium EDFs. This model will be the basis for the further study the impedance matching between RF system and RF-ICP, which takes the kinetic effect into account.

Chapter 6 is the summary of this thesis.

Chapter 2

Equivalent Circuit Model of RF-ICP

The characteristics of plasma impedance has been analyzed by using analytic model. Although the analytic model is not suitable for quantitative prediction of the plasma due to its simplified description, it is still useful to know the basic features of the RF ICP as a circuit element. In this chapter, overview of the analytic modeling is presented.

2.1 Introduction: Impedance Matching and Plasmas

Basic theory of impedance matching is introduced in this section. In electronics, impedance matching is to design input impedance of a load or output impedance of a signal source to be the same value with each other. This practice is mandatory to avoid the reflection of sending signal at a discontinuous point between the load and the signal source. Now we consider the reflection of a signal at a discontinuous point d between input impedance Z_1 and Z_2 as shown in Fig. 2.1.

At the point d, signals of voltage and current satisfy continuity conditions as follows:

$$v_i + v_r = v_t, \tag{2.1}$$

$$i_i + i_r = i_t, \tag{2.2}$$
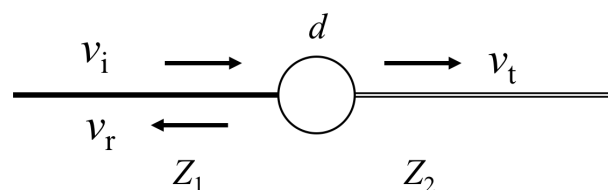
Fig. 2.1   Reflection of signal at discontinuous point.

where v_i, i_i, v_r, i_r, v_t and i_t are forward voltage/current, reflected voltage/current and transmitted voltage/current, respectively. Voltage and current can be related to each other using Ohm's law:

$$v_i = i_i Z_1, \tag{2.3}$$

$$v_r = i_r Z_1, \tag{2.4}$$

$$v_t = i_t Z_2. \tag{2.5}$$

Combining Eqs. (2.1) - (2.5) leads to the following relations,

$$v_r = \frac{Z_2 - Z_1}{Z_2 + Z_1} v_i, \tag{2.6}$$

$$v_t = \frac{2Z_2}{Z_2 + Z_1} v_i, \tag{2.7}$$

$$i_r = -\frac{Z_2 - Z_1}{Z_2 + Z_1} i_i, \tag{2.8}$$

$$i_t = \frac{2Z_1}{Z_2 + Z_1} i_i. \tag{2.9}$$

From above relations, one can find that reflected signal does not exist where $Z_1 = Z_2$. In that case, signal are sent to the load without any loss, which is ideal condition for efficient power supply to the load. The following parameters are also of importance to describe the impedance matching:

$$\Gamma_v = \frac{v_r}{v_i} = \frac{Z_2 - Z_1}{Z_2 + Z_1}, \tag{2.10}$$

$$T_v = \frac{v_t}{v_i} = \frac{2Z_2}{Z_2 + Z_1} = 1 + \Gamma_v, \tag{2.11}$$

$$\Gamma_i = \frac{i_r}{i_i} = -\frac{Z_2 - Z_1}{Z_2 + Z_1} = -\Gamma_v, \tag{2.12}$$

$$T_i = \frac{i_t}{i_i} = \frac{2Z_1}{Z_2 + Z_1} = 1 - \Gamma_v, \tag{2.13}$$

where Γ_v, Γ_i, T_v and T_i are the reflection coefficients of voltage and current, the transmission coefficients of voltage and current, respectively.

Common practice for the impedance matching is installation of matching circuit which is composed of capacitor and inductor. Configuration of matching circuit is determined by the operational signal frequency and the impedance of signal source and the load. In general, resistor is not used for matching circuits because it causes undesirable power loss.

In an RF system of the RF driven type ion source, however, the output impedance includes that of plasma whose features as circuit element is difficult to define. This causes the difficulty of designing RF system. In the next section, we present the analytic description of impedance of the RF ICP. This approach is mandatory to understand the basic features of RF system with the plasma load.

2.2   The Transformer Model

The transformer model [4] is a model to describe RF plasmas as a circuit element. We describe the principle of the transformer model in the following sections.

Note that an arbitrary parameter A which varies sinusoidally will be expressed by following rules hereafter:

$$A = \mathrm{Re}[\tilde{A}e^{i\omega t}],$$

$$\tilde{A} = A_\mathrm{r} + iA_\mathrm{im}.$$

Since the transformer model uses a linear harmonic analysis to model the RF ICP, this expression is convenient to describe.

The complex impedance of an arbitrary circuit element Z can be defined from the relation between the complex power input $\tilde{P}$ and the magnitude of the current $\tilde{I}$ flowing in the element:

$$\tilde{P} = \frac{1}{2}Z\tilde{I}^2. \tag{2.14}$$

The impedance of the RF ICP can also be calculated by the above relation. Therefore, when the dissipated power and the current in the plasma have been defined, the plasma impedance can also be defined. The main part of the impedance calculation is then to solve the Maxwell's equation to calculate the power dissipation and the current in the plasma.

2.2.1   Overview of the transformer model

The transformer model which we describe here is the model that defines the impedance of the cylindrical RF ICP. The cylindrical RF ICP is ignited by the surrounding solenoid coil (see Fig. 2.2 (a)). As for the Linac4 H$^-$ source, for example, the geometric features of the system are as follows: the radius of the chamber $r_0 = 24$ mm, coil length, $l = 28.5$ mm, the number
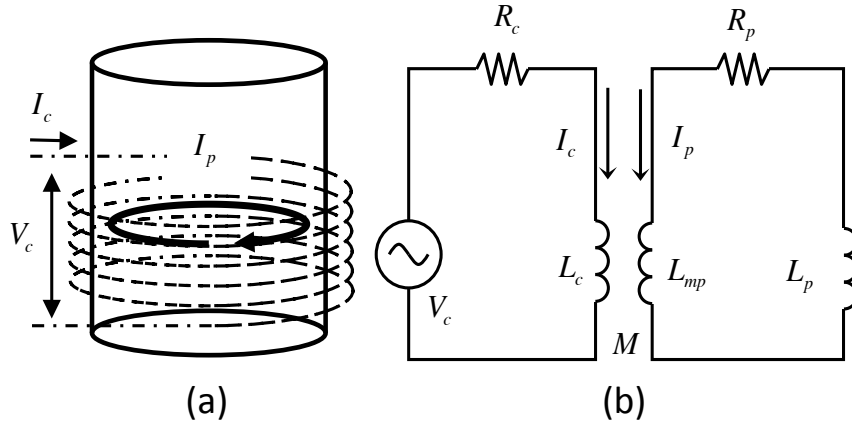
Fig. 2.2   The transformer model: (a) schematic of the ion source chamber and (b) the equivalent circuit of RF plasma inside the chamber and the antenna.

of turns of the coil $N = 5.5$.

The coil current I_{coil} induces azimuthal electric field and the resultant the plasma current I_{p}. In the RF range, note that the plasma current is dominantly composed of electrons because other charged particles are too heavy to respond to the RF field. The RF ICP can be described as an LR series circuit coupled inductively with the primary circuit (see Fig. 2.2 (b)). The symbol R_{p} denotes the resistance of plasma and L_{p} is the inductance due to electron inertia which is known to be $L_{\text{p}} = R_{\text{p}}/\nu_{en}$, where ν_{en} is collision frequency of electrons. The neutral gas pressure for Linac4 operation is relatively high (a few Pa) so that the collision process with neutrals are assumed to be dominant for ν_{en}. Plasma inductance L_{mp} is due to magnetic flux, which is created by the circular shaped plasma current. When plasma skin depth is thin enough, the current channel can be seen the same as the solenoid antenna. Hence L_{mp} can be defined in the same manner as that of solenoid antenna.

In the following sections, we derive the mathematical expressions of above circuit parameters.

2.2.2   Plasma as a conductive material

The permittivity and conductivity of plasma can be derived from the momentum conservation. For simplicity, we assume that:

- The RF electromagnetic wave propagates in the z-direction and its electric field has only the component E_x in the x-direction.
- Electron is only the particle specie which responds to RF electromagnetic fields.
- Spatial distributions of the electron density n_{e} and temperature T_{e} are uniform.

- There is no steady current, which means no net current flows when it is averaged over an RF cycle.

The above assumptions allow us to linearize the momentum conservation equation for electron as follows,

$$n_{\mathrm{e}} m i \omega \tilde{u}_x = -n_{\mathrm{e}} e \tilde{E}_x - n_{\mathrm{e}} m \nu_{\mathrm{en}} \tilde{u}_x, \tag{2.15}$$

where ω is the frequency of electromagnetic wave, ν_{en} is the collision frequency between electrons and neutral particles, and m, e and u_x are the mass, the charge and the velocity of electron, respectively. From Eq.(2.15), the relation between the magnitudes of the perturbation in velocity and electric field amplitude can be written as

$$\tilde{u}_x = \frac{-e}{m(i\omega + \nu_{en})} \tilde{E}_x. \tag{2.16}$$

The net current $\tilde{J}_x$ is a sum of the displacement current due to time varying electric field and the true current due to the motion of electron:

$$
\begin{aligned}
\tilde{J}_x = i\omega\varepsilon_0 \tilde{E}_x + n_e(-e)\tilde{u}_x &= i\omega\varepsilon_0 \left(1 + \frac{n_e e^2}{i\omega\varepsilon_0 m(i\omega + \nu_{en})} \right) \tilde{E}_x \\
&\equiv i\omega\varepsilon_0 \left(1 - \frac{\omega_{pe}^2}{\omega(\omega - i\nu_{en})} \right) \tilde{E}_x \\
&\equiv i\omega\varepsilon_0 \varepsilon_{\mathrm{p}}(\omega) \tilde{E}_x
\end{aligned}
\tag{2.17}
$$

where ω_{pe} is the electron plasma frequency and ε_{p} is the permittivity of plasma. The Maxwell's equations are simplified by using the permittivity ε_{p}, which are solved in the next section.

2.2.3   Maxwell's equations in the cylindrical RF-ICP

Suppose that the system is composed of the long cylindrical plasma chamber surrounded by a solenoidal coil as shown in Fig. 2.3. By assuming the axial symmetry of the system, the Maxwell's equations become

$$-\frac{\partial \tilde{H}_z}{\partial r} = i\omega\varepsilon_0\varepsilon \tilde{E}_\theta, \tag{2.18}$$

$$\frac{1}{r}\frac{\partial(r\tilde{E}_\theta)}{\partial r} = -i\omega\mu_0 \tilde{H}_{\mathrm{z}}, \tag{2.19}$$

where $\varepsilon = \varepsilon_p$ in the plasma and $\varepsilon = \varepsilon_t$ in the wall of the chamber. One can derive the Bessel equation for the magnetic field from Eqs. (2.18) and (2.19),

$$\frac{\partial^2 \tilde{H}_z}{\partial r^2} + \frac{1}{r}\frac{\partial \tilde{H}_z}{\partial r} + k_0^2 \varepsilon \tilde{H}_z = 0. \tag{2.20}$$

Therefore, the solutions of the Maxwell's equations are,

$$\tilde{H}_z = H_{z0} \frac{J_0(kr)}{J_0(kr_0)}, \tag{2.21}$$

$$\tilde{E}_\theta = \frac{ikH_{z0}}{\omega\varepsilon_0\varepsilon_p}\frac{J_1(kr)}{J_0(kr_0)}, \tag{2.22}$$

where $H_{z0} = \tilde{H}_z(r = r_0)$, J_n is the Bessel function of the n-th order and $k = k_0\sqrt{\varepsilon}$ is the wave number of the wave inside the plasma. We assume H_{z0} to be the real number so that the phase of the magnetic fields at the edge of the plasma becomes the reference for the phase of all other complex parameters.

The electromagnetic field inside the chamber wall, on the other hand, can be assumed to be uniform because its wavelength is long enough compared to the width of the chamber wall ($\sim 10^{-2}$ m) within the frequency range of interest (a few MHz). Therefore,

$$\tilde{H}_z(r_0 < r < r_c) \approx H_{z0}. \tag{2.23}$$

Under this assumption, the electric field outside the wall can be derived from integral form of Faraday's law,

$$\oint \tilde{E}_\theta dl = -\frac{\partial}{\partial t}\iint \tilde{B}_z dS \tag{2.24}$$

$$\Rightarrow \tilde{E}_\theta(r_c) = \tilde{E}_\theta(r_0)\frac{r_0}{r_c} - i\omega\mu_0 H_{z0}\left(\frac{r_c^2 - r_0^2}{2r_c}\right). \tag{2.25}$$

In the next chapter, we discuss the relation among the coil/plasma currents and the electromagnetic field that has just been derived.

Fig. 2.3   Cross sectional view of the chamber.

2.2.4   Plasma current and coil current

The total current flowing in the plasma I_p can be calculated by integrating the current density from the center to the edge of the plasma:

$$\tilde{I}_p = l \int_0^{r_0} \tilde{J}_\theta \mathrm{d}r. \tag{2.26}$$

The current density on the right hand side and the electric fields we derived in the last section can be related by Eq. (2.17). By substituting Eqs. (2.17) and (2.22) into Eq. (2.26), the integral can be calculated as follows:

$$\tilde{I}_p = lH_{z0} \frac{1}{\mathrm{J}_0(kr_0)} \int_0^{kr_0} \mathrm{J}_1(kr)\mathrm{d}(kr) = lH_{z0} \left[\frac{1}{\mathrm{J}_0(kr_0)} - 1 \right]. \tag{2.27}$$

It is also a good practice to discuss the current I_p from Ampère's theorem. Figure 2.4 shows the integral paths for Ampère's theorem. Contour 1 gives the same result as Eq. (2.27):

$$\tilde{I}_p = l\tilde{H}_z(0) - lH_{z0} = lH_{z0} \left[\frac{1}{\mathrm{J}_0(kr_0)} - 1 \right]. \tag{2.28}$$

Likewise, contour 2 and 3 give the displacement current flowing in the dielectric tube $\tilde{I}_t$, and

the current flowing in the coil $\tilde{I}_{RF}$, respectively:

$$\tilde{I}_t = lH_{z0} - l\tilde{H}_z(r_c), \tag{2.29}$$

$$N\tilde{I}_{RF} = l\tilde{H}_z(r_c), \tag{2.30}$$

where N is the number of turns of the coil. The sum of these three currents therefore becomes

$$\tilde{I}_p + \tilde{I}_t + N\tilde{I}_{RF} = \frac{lH_{z0}}{J_0(kr_0)}. \tag{2.31}$$

With the assumption Eq. (2.23), the magnetic field in the chamber wall can be considered as uniform, which leads to $\tilde{I}_t = 0$. Combining Eqs. (2.31), (2.28) and $\tilde{I}_t = 0$, one obtains the relation between the current in the coil and the magnetic field as follows;

$$H_{z0} = \frac{N\tilde{I}_{RF}}{l}. \tag{2.32}$$

This relation explains that $\tilde{I}_{RF}$ is in phase with H_{z0} whose phase we defined as the reference in this analysis. Thus the current $\tilde{I}_{RF}$ is equivalent to the magnitude of the coil current I_{coil}. Then we express the relation as follows:

$$H_{z0} = \frac{NI_{coil}}{l}. \tag{2.33}$$

When the plasma density is high enough so that $kr_0 \ll 1$, the Bessel function of complex argument grows exponentially and consequently,

$$\tilde{I}_p + NI_{coil} \approx 0, \tag{2.34}$$

In this condition, the plasma current is localized at the periphery of the chamber at the edge of the chamber, which is to cancel the magnetic field induced by the coil current. This description is important to understand the basic concept of the transformer model.

2.2.5   Poynting theorem

As we have already pointed out in the overview of the transformer model, definition of impedance calls for calculation of the power dissipation and the current in the plasma. Now that the expressions of electromagnetic field inside the plasma has been obtained, we can derive the complex power input which is the sum of the power dissipated and stored in the
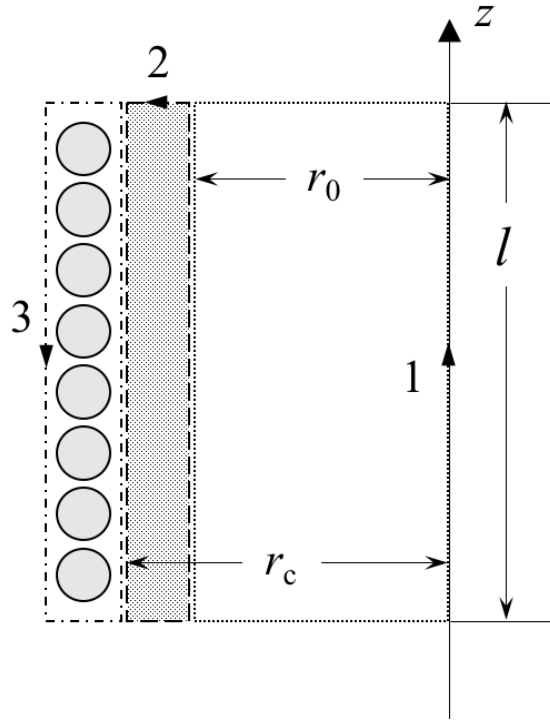
Fig. 2.4   Ampère contours for the current in the Plasma (1), in the dielectric tube (2) and in the coil (3).

plasma. Integrating the Poynting vector at the surface of the plasma, we obtain

$$\tilde{P} = -\frac{1}{2}\tilde{E}_\theta(r_c)\tilde{H}_z(r_c)2\pi r_c l = \frac{1}{2}Z_{ind}I_{coil}^2, \tag{2.35}$$

where Z_{ind} is the total complex impedance of the system including the plasma and the coil. By using Eqs. (2.23), (2.25) and (2.33), the input power can also be written as

$$\tilde{P} = i\frac{\pi N^2 I_{coil}^2}{l}\left[\frac{kr_0 J_1(kr_0)}{\omega\varepsilon_0\varepsilon_p J_0(kr_0)} - \frac{1}{2}\omega\mu_0(r_c^2 - r_0^2)\right]. \tag{2.36}$$

2.2.6   Plasma resistance R_p and inductance L_{mp}

The plasma resistance is defined from the relation

$$P_{abs} = \frac{1}{2}R_p|\tilde{I}_p|^2, \tag{2.37}$$

where P_{abs} is the dissipated power in the plasma, which corresponds to the real part of complex power input that we have derived as Eq. (2.36):

$$P_{abs} = \mathrm{Re}[\tilde{P}] = \frac{\pi N^2}{l\omega\varepsilon_0}\mathrm{Re}\left[\frac{ikr_0\mathrm{J}_1(kr_0)}{\varepsilon_p\mathrm{J}_0(kr_0)}\right]I_{coil}^2. \tag{2.38}$$

Then we obtain the definition of R_P from Eqs. (2.27)(2.33) and (2.38) as follows:

$$R_p = \frac{2P_{abs}}{|\tilde{I}_p|^2} = \frac{2\pi}{l\omega\varepsilon_0}\mathrm{Re}\left[\frac{ikr_0\mathrm{J}_1(kr_0)}{\varepsilon_p\mathrm{J}_0(kr_0)}\right]\left|\frac{1}{\mathrm{J}_0(kr_0)} - 1\right|^{-2}. \tag{2.39}$$

The transformer model uses the assumption that the plasma current is localized at the edge of the chamber so that the inductance of the plasma can simply be defined by the magnetic flux inside the circular plasma current channel. Hence it can be derived in the same manner as that of solenoidal coil:

$$L_{mp} = \frac{\mu_0\pi r_0^2}{l}. \tag{2.40}$$

2.2.7   Inertia inductance L_p

The inertia of the plasma can be regarded as the inductance since it produces a phase difference between the plasma current and the applied RF field. The difference can be derived from Eq. (2.15). What is to be derived here is the relation between the applied voltage and the plasma current. From Eq. (2.15), we can obtain

$$mn_e\frac{du}{dt}eS = -n_ee^2ES - n_emv_mueS, \tag{2.41}$$

$$-m\frac{dI}{dt} = -n_ee^2ES + mv_mI, \tag{2.42}$$

where S is the effective area where plasma current flows. The Assuming that the applied electric field and the voltage can be related by $V = \oint E \cdot dl = El$, Eq. (2.42) becomes

$$E = \frac{m}{n_ee^2S}\frac{dI}{dt} + \frac{mv_m}{n_ee^2S}I. \tag{2.43}$$

$$\Rightarrow V = \frac{ml}{n_e e^2 S} \frac{dI}{dt} + \frac{mv_m l}{n_e e^2 S} I \tag{2.44}$$

$$\equiv L_p \frac{dI}{dt} + R_p I, \tag{2.45}$$

where l is the length of the integral path ($l = 2\pi r$ in the case of cylindrical ICP discharges). As we define the coefficients of dI/dt and I are the inertia inductance L_p and the plasma resistance R_p, respectively, those can be related as follows:

$$L_p = R_p/v_m. \tag{2.46}$$

2.2.8   Mutual inductance M

The mutual inductance M between coil and plasma can be derived from the circuit equation of the circuit which is shown in Fig. 2.2 (b):

$$\tilde{V}_p = i\omega L_{mp} \tilde{I}_p + i\omega M I_{coil} = -\tilde{I}_p \left[R_p + iR_p \left(\frac{\omega}{v_m} \right) \right]. \tag{2.47}$$

Assuming M to be the real number, one can obtain

$$M^2 \omega^2 = \left[R_p^2 + \left(\omega L_{mp} + R_p \left(\frac{\omega}{v_m} \right) \right)^2 \right] \frac{|\tilde{I}_p|^2}{I_{coil}^2}, \tag{2.48}$$

which is calculable since all the parameters on the right hand side have already been defined in the previous sections.

2.3   Impedance measurement and the transformer model

In the next section, the transformer model is applied to analyze the impedance matching in the CERN's Linac4 RF system. The results are compared with the previous work which was carried out at CERN [29]. In the previous work, the impedance of the plasma has experimentally been investigated in accordance with an equivalent circuit. Figure 2.5 shows the matching circuit which is installed in the Linac4 RF system and the equivalent circuit of the plasma. Table. 3.1 shows the typical values of each components.

One can find that the equivalent circuit model which is shown in Fig. 2.5 is different from the one we have derived so far. While we choose the transformer model to describe the RF ICP, its description can be reformulate so that the impedance becomes comparable with
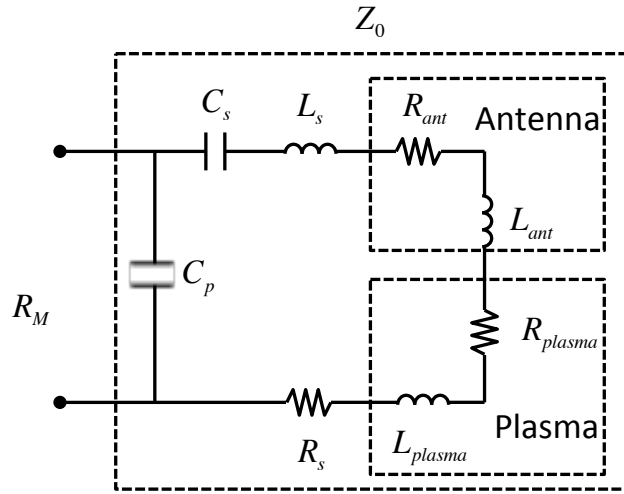
Fig. 2.5   Antenna and matching circuit.
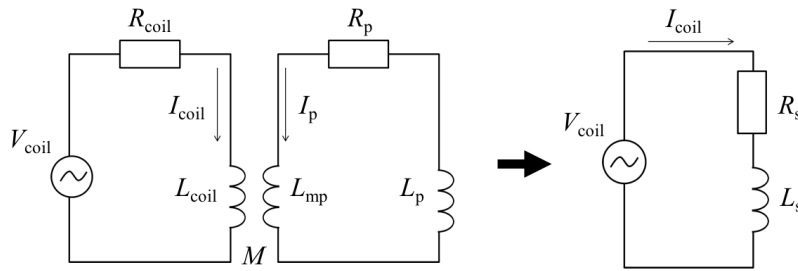
Fig. 2.6   The transformer model of an inductive discharge. On the right, the secondary circuit has been transformed into its series equivalent in terms of the primary circuit current.

R_{plasma} and L_{plasma} shown in Fig. 2.5. The reformulation can be done by transforming the circuit equations of the transformer model into that of a series circuit. Figure 2.6 shows a series circuit model which is equivalent to the transformer model. As for the primary coil shown on left hand side of Fig. 2.6, the circuit equation becomes

$$\tilde{V}_{\text{coil}} = i\omega L_{\text{coil}} I_{\text{coil}} + R_{\text{coil}} I_{\text{coil}} + i\omega M \tilde{I}_{\text{p}}, \tag{2.49}$$

while the circuit equation for the secondary coil is expressed in Eq. (2.47). As for the circuit shown on right hand side of Fig. 2.6,

$$\tilde{V}_{\text{coil}} = (i\omega L_{\text{s}} + R_{\text{s}}) I_{\text{coil}}. \tag{2.50}$$

Combining Eqs. (2.47), (2.48) and (2.49), one can obtain

$$R_\mathrm{s} = R_\mathrm{coil} + R_\mathrm{p} \frac{|\tilde{I}_\mathrm{p}|^2}{I_\mathrm{coil}^2} \equiv R_\mathrm{ant} + R_\mathrm{plasma}, \tag{2.51}$$

$$L_\mathrm{s} = L_\mathrm{coil} - \left(L_\mathrm{mp} + \frac{R_\mathrm{p}}{\nu_\mathrm{m}} \right) \frac{|\tilde{I}_\mathrm{p}|^2}{I_\mathrm{coil}^2} \equiv L_\mathrm{ant} + L_\mathrm{plasma}. \tag{2.52}$$

This shows that R_plasma and L_plasma which are measured at CERN's measurement are also calculable from the transformer model.

Chapter 3

Experimental & Theoretical Study on Plasma Impedance

3.1 Publication-1: Equivalent Circuit of Radio Frequency-Plasma with the Transformer Model [37]

3.1.1 Abstract

LINAC4 H⁻ source is radio frequency (RF) driven type source. In the RF system, it is required to match the load impedance, which includes H⁻ source, to that of final amplifier. We model RF plasma inside the H⁻ source as circuit elements using transformer model so that characteristics of the load impedance become calculable. It has been shown that the modeling based on the transformer model works well to predict the resistance and inductance of the plasma.

3.1.2 Introduction

RF driven type H⁻ source is used as an injector of LINAC4. In the LINAC4 H⁻ source, the plasma is heated by a 100 kW, 2 MHz, 10 % bandwidth RF system. It is required to match the load impedance, which includes H⁻ source, to that of final amplifier in order to maximize the power supplied to the plasma inside the source chamber. In the previous work at CERN, designing of the matching circuit has been done. The configuration of the load circuit is shown in Fig. 3.1. Capacitance C_p and C_s are determined to match the load impedance to that of final amplifier $R_m = 50\Omega$. In Ref. [29], frequency hopping (switching between two predefined frequencies $f_1 = 1946$ kHz, $f_2 = 2000$ kHz) is proved to be useful to cope with the wide load impedance change due to plasma formation. In this paper, we propose the analytic
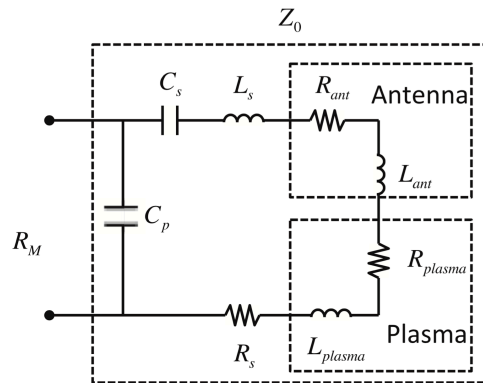
Fig. 3.1   Antenna and matching circuit [37].
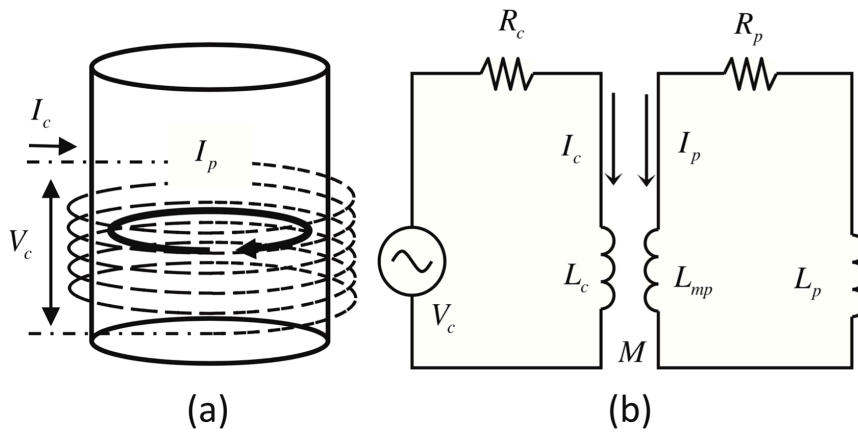
Fig. 3.2   The transformer model: (a) schematic of the ion source chamber and (b) the equivalent circuit of RF plasma inside the chamber and antenna [37].

model of RF plasma as circuit elements aiming the prediction of R_{plasma} and L_{plasma}. This work allows us to calculate frequency characteristics of the circuit, which is to be investigated for improvement of frequency hopping.

3.1.3   Equivalent circuit model

In this chapter, we present the modeling scheme of RF plasma, which is based on two models: electromagnetic model and the transformer model [4]. These two models of RF plasma allow us to define R_{plasma} and L_{plasma} analytically.

A. Overview of the transformer model

The source chamber that contains plasma is surrounded by coil (see Fig. 3.2(a)). The geometric features of the system are as follows: radius of chamber r_0 = 24 mm, coil length l = 28.5 mm, the number of turns of the coil N = 5.5. The coil current I_c induces the plasma current I_p, which is mainly composed of electrons. This inductively coupled plasma (ICP) can be described as RL series circuit coupled inductively with the primary circuit (see Fig. 3.2(b)). The symbol R_p denotes resistance of plasma and Lp is the inductance due to electron inertia which is known to be $L_p = R_p/\nu_{en}$, where ν_{en} is collision frequency of electrons. The neutral gas pressure for LINAC4 operation is relatively high (a few Pa) and collision process with neutrals are assumed to be dominant for ν_{en}. The collision frequency ν_{en} is chosen correctly based on this assumption. Plasma inductance L_{mp} is due to magnetic flux, which is created through the circular shaped plasma current. When plasma skin depth is thin enough, the current channel can be seen same as the solenoid antenna. Thus L_{mp} can be defined same manner as that of solenoid:

$$L_{mp} = \frac{\mu_0 \pi r_0^2}{l}. \tag{3.1}$$

In the following analysis, $\tilde{A}$ denotes the complex amplitude of arbitrary value A: $A = \text{Re}\left[\tilde{A}e^{i\omega t}\right]$, where ω is angular frequency of the RF system. We derive the expression of R_{plasma} and L_{plasma} based on this transformer model in the next section.

B. Modeling of R_{plasma} and L_{plasma}

While we choose the transformer model to describe RF plasma, the expressions of R_{plasma} and L_{plasma}, [29] which are modeled as series circuit elements, can be obtained by transforming the circuit equations of the transformer model into that of a series circuit (compare the model of plasma in Figs. 3.2(b) and 3.1):

$$\tilde{V}_c = (i\omega L_{tot} + R_{tot})I_c. \tag{3.2}$$

As a result, R_{tot} and L_{tot} are defined as follows:

$$R_{tot} = R_c + R_p \frac{|\tilde{I}_p|^2}{I_c^2} \equiv R_c + R_{plasma}, \tag{3.3}$$

$$L_{tot} = L_c - \left(L_{mp} + \frac{R_p}{\nu_{en}}\right)\frac{|\tilde{I}_p|^2}{I_c^2} \equiv L_c + L_{plasma}. \tag{3.4}$$
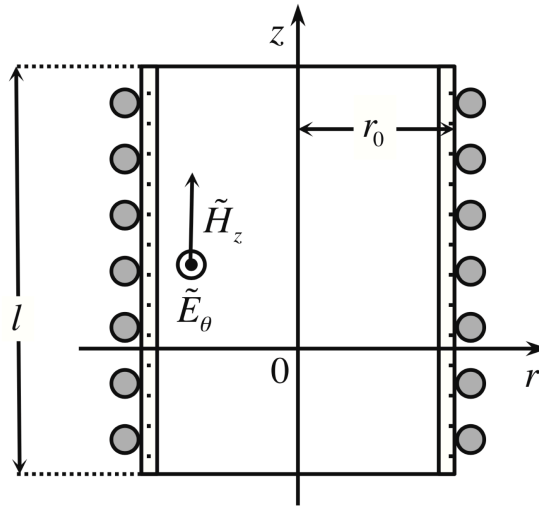
Fig. 3.3   Cross sectional view of the chamber [37].

Still the plasma resistance R_p is unknown value so that these definitions of R_{plasma} and L_{plasma} are not calculable for the circuit analysis. We introduce the derivation of plasma resistance based on electromagnetic model in the next section.

C. Electromagnetic model

The concept of the electromagnetic model [4] is to model the plasma resistance from the basic relation with the dissipated power in the plasma P_{abs} and the current (i.e., $P_{\text{abs}} = R_p|\tilde{I}_p|^2/2$). In order to obtain the expressions of P_{abs} and $\tilde{I}_p$, it is necessary to know the electromagnetic field from the solutions of Maxwell's equations.

The plasma inside the chamber is described as a uniform medium whose permittivity ε_p is complex value:

$$\varepsilon_p = 1 - \frac{n_e e^2}{m_e \varepsilon_0} \frac{1}{\omega(\omega - iv_{\text{en}})}. \tag{3.5}$$

where n_e is the number density of electrons, e is the electric charge, m_e is the of electron (see Ref. [4] for more detailed explanation). Then the solutions of Maxwell's equations can be obtained readily in the cylindrically symmetric coordinate system (see Fig. 3.3): the electric field and the magnetic field are composed of only θ-component $\tilde{E}_\theta$ and z-component $\tilde{H}_z$. Coming back to the expressions of P_{abs} and $\tilde{I}_p$, these are obtained by integrating the Poynting vector at the surface of the plasma or applying Ohm's law.

Consequently, the plasma resistance can be derived as follows:

$$R_{\text{plasma}} = \frac{2P_{\text{abs}}}{I_c^2} = \frac{2\pi N^2}{l\omega\varepsilon_0}\text{Re}\left[\frac{ikr_0 \text{J}_1(kr_0)}{\varepsilon_p \text{J}_0(kr_0)}\right], \tag{3.6}$$

$$R_p = \frac{2P_{\text{abs}}}{|\tilde{I}_p|^2} = \frac{2\pi}{l\omega\varepsilon_0}\text{Re}\left[\frac{ikr_0 \text{J}_1(kr_0)}{\varepsilon_p \text{J}_0(kr_0)}\right]\left|\frac{1}{\text{J}_0(kr_0)} - 1\right|^{-2}, \tag{3.7}$$

where J_n and $k = k_0\sqrt{\varepsilon}$ are the Bessel function of the n-th order and the wave number of the plasma, respectively.

Now that calculable definition of R_{plasma} and L_{plasma} has been obtained, the calculation results of some characteristics of the matching circuit are introduced in the next section.

3.1.4   Results and Discussion

We calculate R_{plasma} and L_{plasma} from Eqs. (3.4), (3.5) and (3.7) with two variables, i.e., frequency of the RF system f and electron density n_e. The other parameters are constant values, which are listed in Table 3.1. Note that the electron temperature is assumed to be 10 eV, which is the typical temperature of RF plasmas. From the calculation results of R_{plasma} and L_{plasma}, voltage reflection coefficient Γ_V of the matching circuit (Fig. 3.1) has also been calculated whose definition is,

$$\Gamma_V = \frac{R_M - Z_0}{R_M + Z_0}. \tag{3.8}$$

Table 3.1   Calculation condition.

Parameters	Value	Parameters	Value
H_2 gas pressure	3.0 Pa	R_m	50Ω
H_2 gas tempetature	300 K	L_{ant}	3.2μH
Dissociation rate of H_2	0.1	R_{ant}	0.4Ω
Electron temperature T_e	10 eV	L_s	1.98μH
Chamber radius r_0	24 mm	R_s	0.5Ω
Coil length l	28.5 mm	C_p	6.5nF
Turns of the coil N	5.5	C_s	1.61nF
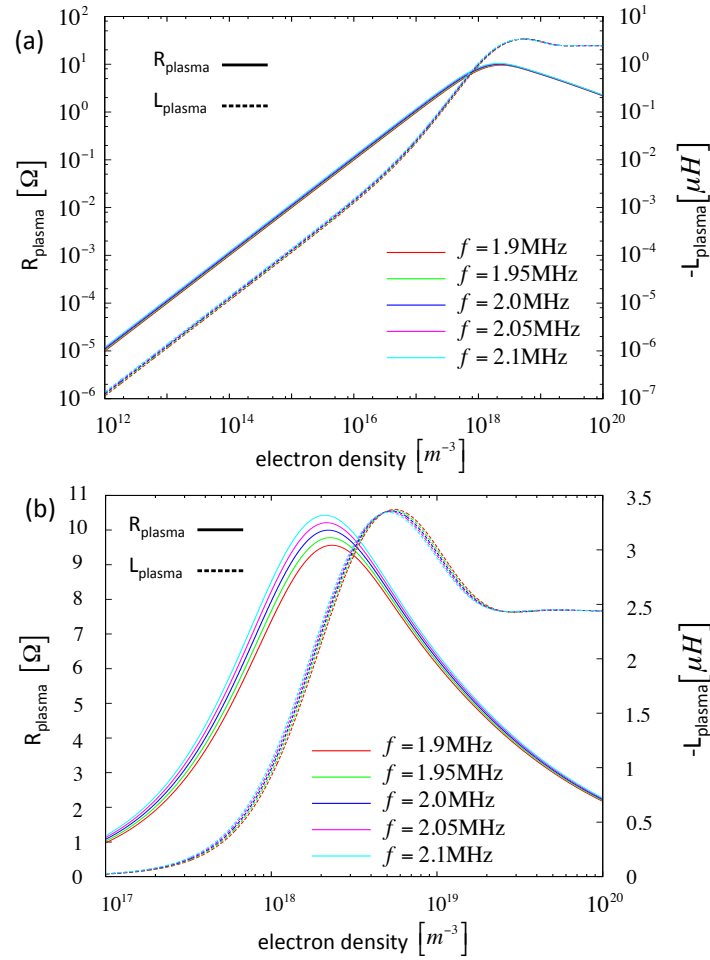
Fig. 3.4   Calculation of R_{plasma} and L_{plasma} as functions of the electron density, where (a) $10^{12}\text{m}^{-3} \leq n_{\text{e}} \leq 10^{20}m^{-3}$, (b) $10^{17}\text{m}^{-3} \leq n_{\text{e}} \leq 10^{20}m^{-3}$, for various frequencies [37].

A. Calculation results

The electron density dependence of R_{plasma} and L_{plasma} has been shown in Fig. 3.4. Each line indicates the difference due to the frequency of the system. From Fig. 3.4 (a), one can fined that the magnitude of R_{plasma} and L_{plasma} increase in the low electron density regime and take the maximums where $n_{\text{e}} \approx 10^{18}\text{m}^{-3}$. Similar tendency has been provided by the 3 dimensional numerical simulation [38]. According to the measurement results, it has been shown that the magnitudes of R_{plasma} and L_{plasma} increase in the initial phase and reach $R_{\text{plasma}} \approx 2.5\Omega$ and $L_{\text{plasma}} \approx -0.4\mu\text{H}$. Suppose that the electron density range of the typical RF plasma in a steady state is $10^{17}\text{m}^{-3} \leq n_{\text{e}} \leq 10^{18}\text{m}^{-3}$, the calculation values are the same order as these experimental results. Also, as shown in Fig. 9 in Ref. [29], the values of R_{plasma} and L_{plasma} in the steady state do not significantly depends on the frequency changes. This tendency of
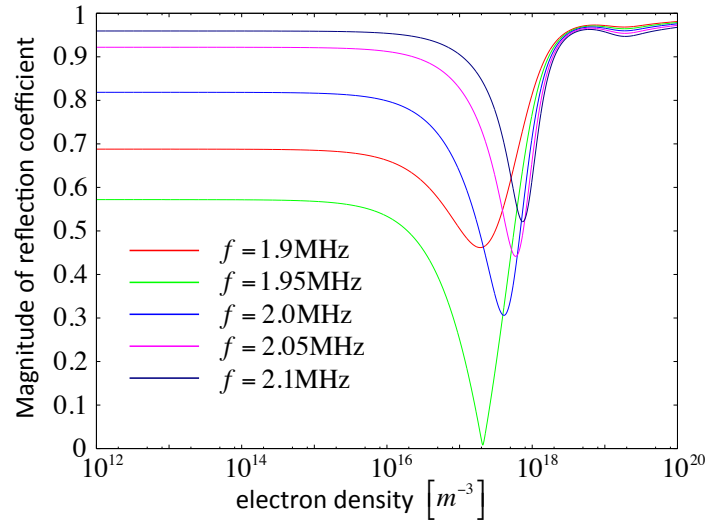
Fig. 3.5   Reflection coefficient as a function of the electron density for various frequencies [37].

experimental results agrees well with our calculation results.

The magnitude of voltage reflection coefficient $|\Gamma_v|$ of the circuit has been shown in Fig. 3.5. The response of the circuit can be characterized as follows:

1. When the electron density is low, the circuit shows the least reflection where $f = 1.95$MHz.

2. The electron density where the reflection takes minimum becomes higher as the frequency becomes higher.

3. When the electron density is high ($n_e \geq 10^{18}\text{m}^{-3}$), the reflection has small frequency dependence.

From these characteristics, it is suggested the frequency of the system be 1.95 MHz in the initial phase. That is because the resonant frequency f_r of the matching circuit without plasma corresponds to 1.95 MHz:

$$f_r = \sqrt{\frac{1}{L_T}\left(\frac{1}{C_p} + \frac{1}{C_s}\right)}, \tag{3.9}$$

where $L_T = L_{ant} + L_s + L_{plasma}$ ($L_{plamsa} = 0$ in this case). As seen from Fig. 3.4, the total inductance L_T becomes smaller as the electron density increases. The decrease in L_T causes increase in the resonant frequency especially in the density range $n_e \geq 10^{17}\text{m}^{-3}$ (see Fig. 3.4 and Eq. (3.9)), which leads to detuning effect. In order to overcome this detuning effect, it is necessary to increase the frequency of RF driver. In the experiments, frequency hopping, i.e., frequency changes from 1.95 MHz to 2.0 MHz, has been employed for this reason. On

the other hand, if the higher electron density is required ($n_e \geq 10^{18} \mathrm{m}^{-3}$), we may need to redesign the matching circuit because the reflection is close to unity with any frequencies.

B. Summary and discussion

The calculation results of the impedance of RF plasma and the frequency characteristics have been shown in this paper. The impedance of the plasma shows good agreement with the measurement and also the simulation results. Moreover, our calculation reproduces the usability of frequency hopping, which has already been found experimentally. These agreements show that the transformer model works well to predict the impedance of the plasma. However, the transformer model may not be quantitative in some cases because of the some assumptions for simplification of the model. For example, antenna solenoid is assumed to be ideal. This assumption causes the overestimation of the electromagnetic field inside the chamber, which leads to overestimation of R_{plasma} and L_{plasma}. Moreover, when electron density is low, the results may have less reliability. That is because Eq. (3.1) holds only when skin effect is strong enough to let plasma current channel be narrow. Since more sophisticated modeling is required for more quantitative analysis, now we are planning to improve the transformer model, which is available to the general conditions.

3.2   Publication-2: Experimental Investigation of Plasma Impedance in Linac4 H⁻ Source [39]

3.2.1   Abstract

CERN's new particle accelerator Linac4 is part of the upgrade of the LHC accelerator chain. Linac4 is required to deliver 160 MeV H⁻ beam to improve the beam brightness and luminosity in the Large Hadron Collider (LHC). The Linac4 H⁻ source must deliver 40-50 mA, 45 keV H⁻ beam in the RFQ acceptance. Since the RF power coupled to the H⁻ source plasma is one of the important parameters that determines the quality of the H⁻ beam, the experimental investigation of the dependence of the load impedance on the operational parameters is mandatory. In this study, we have measured the impedance of the H⁻ source plasma varying the RF power coupled to the plasma and the condition of the hydrogen gas. Also, optical emission spectroscopy (OES) measurements have been carried out simultaneously with the impedance measurement in order to determine the plasma parameters. The determination of the plasma parameters allows us to compare the experimental results with the analytic model of the plasma parameters, which is useful to discuss the results from a physical point of view.

3.2.2   Introduction

CERN's new particle accelerator Linac4 is part of the upgrade of the LHC accelerator chain. Linac4 is required to deliver 160 MeV H⁻ beam to improve the beam brightness and luminosity in the Large Hadron Collider (LHC). The cesiated surface Linac4 ion source must deliver 40-50 mA, 45 keV H⁻ beam in the RFQ acceptance.

The power transfer efficiency between the RF generator (100 kW from 1.9 MHz to 2.1 MHz) and the ion source plasma is one of the most important parameters that determine the extracted H⁻ beam current [28]. The optimization of the power transfer to an ordinary load can readily be achieved by equalizing the impedance of the load to that of the RF generator, which is realized by the insertion of a matching circuit between the load and the generator. In the case of the Linac4 H⁻ source RF system, however, the optimization during the plasma pulse cannot be done by the matching circuit alone and is achieved by variation of the RF-frequency because the impedance of the load depends on plasma parameters evolution during the pulse.

In the previous work at CERN, it has been shown that the tuning of RF frequency dynamically during the discharge is necessary to improve RF-coupling to the plasma [29]. The tuning is by now automatized, [40] however, the complex relation between the power transfer

efficiency, discharge parameters, hydrogen pressure and plasma impedance deserves further investigation. The aim of our study is to clarify the dependence of the plasma impedance on the operational parameters (RF power coupled to the plasma and hydrogen gas pressure). The dependence will be experimentally investigated varying RF-power and H2 gas pressure. Also the results will be discussed with the analytic model [4, 37], which requires the plasma parameters (electron density n_e and electron temperature T_e) as inputs. Thus optical emission spectroscopy (OES) measurements have been simultaneously carried out in order to measure the plasma parameters.

3.2.3   Experimental Setup

RF Low-Level Control System

The RF low-level control system of Linac4 H$^-$ source is shown in Fig. 3.6. The three-level amplifier chain is capable of delivering the power up to 100 kW. Both the amplitude and the frequency of the RF signal are programmable over the plasma pulse by the automatic voltage control system (AVC). The AVC controls the signal referring the return signal from a high directivity directional coupler (> 30 dB). The forward and reflected signals from the directional coupler are acquired by a high speed digitizer. The digitized signals are processed numerically to calculate the amplitude of the signal and the phase difference between the forward and reflected signals. Those calculated data are used to calculate the impedance of the load (the sum of the matching circuit and the plasma inside the ion source), which is mentioned in the next section.

The typical pre-programmed waveform of the RF signal and the response of the RF system (the forward power P_{fwd}, the reflected power P_{ref})are shown in Fig. 3.7. In the present measurements, only the signal acquired from $t = 0.2$ms to $t = 0.3$ms has been analyzed while the frequency is fixed as shown in Fig. 3.7 for the simplification of the measurement. The frequency is programmed to be larger in steady state than in the ignition phase in order to compensate the change of the load impedance due to the plasma formation [29]. The more detailed description of the RF low-level control system can be found in Ref. [41].

Ion Source and Gas Injection

The schematic of the ion source is shown in Fig. 3.8. The source chamber that contains the plasma is surrounded by RF coil. The geometric features of the system are as follow: the radius of chamber r_c= 24 mm, l_c = 136 mm, the length of the chamber the coil length l_{ant} = 28.5 mm and the number of turns of the coil N= 5. The magnetic configuration inside the chamber comprises a magnetic octopole field in Halbach configuration and a dipole filter
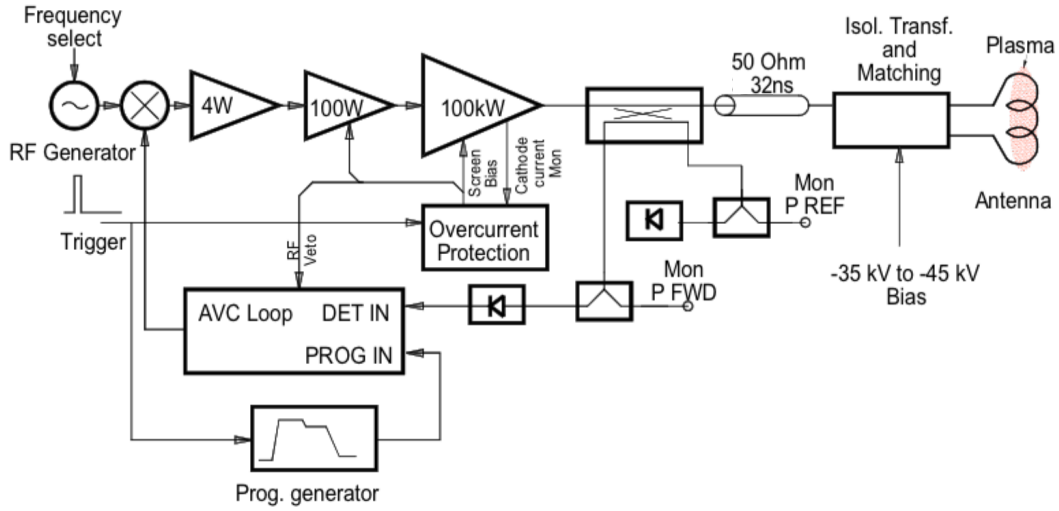
Fig. 3.6   The RF system comprising the RF source, the three-level amplifier chain, the directional coupler and the matching network up to the antenna [29, 41].
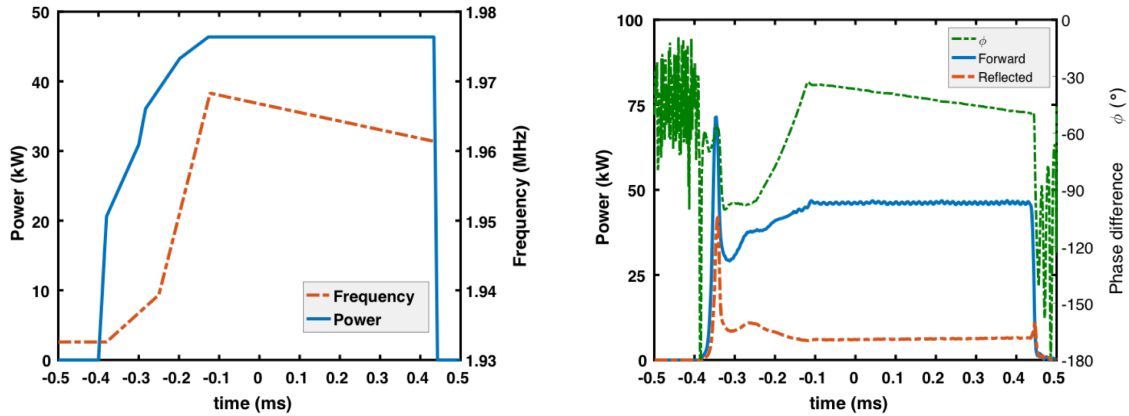
Fig. 3.7   Left: The pre-programmed waveform of amplitude and frequency of signal. Right: the response RF system (the forward and reflected RF power and the phase difference) [39]

field [42]. The port of the gas injection is equipped at the back end of the plasma chamber, which is controlled by a piezo valve. The total amount of the gas injected N_{H_2} through the valve can be controlled by a pulsed voltage signal whose repetition rate $f_p = 1/1.2$ s^{-1}. Four parameters, i.e., the timing of the gas injection t_s, the pulse width w_p, the pulse height V_p and the DC offset of the voltage signal V_{DC}, can be varied to control the gas injection. The front end pumping port equips a turbo molecular pump (pumping speed $S = 500$ l/s) and a vacuum gauge in order to monitor the pressure $p_{H_2}(t)$.

   The measured pressure curve allows us to estimate the total amount of gas N_{H_2}. The gas
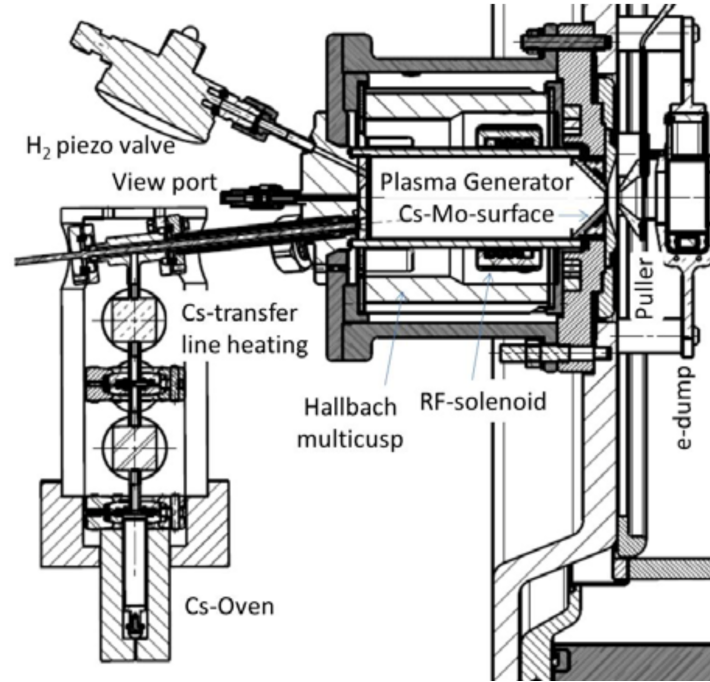
Fig. 3.8   The schematic drawing of the Linac4 H⁻ source [39].

balance equation can be written as:

$$V_{\text{p.p.}} \frac{dp_{H_2}}{dt} = k_B T (Q_{H_2} - S\, p_{H_2}),\tag{3.10}$$

where k_B is the Boltzman constant, $V_{\text{p.p.}} = 0.07 \text{m}^3$ is the volume of the front end vacuum, Q_{H_2} is the number of hydrogen molecules flowing in to the front end vacuum per unit of time and the gas temperature T is assumed to be 300 K. By integrating Eq. (3.10) over a gas cycle, the integration of the pressure curve is found to be representation of N_{H_2}:

$$S \int_0^{1/f_p} p_{H_2} = \int_0^{1/f_p} Q_{H_2} \equiv N_{H_2}.\tag{3.11}$$

In the measurements, the timing of the gas injection t_s and the pulse width w_p are set to be -2.5 ms and 0.5 ms respectively while the pulse height V_p and the DC offset of the voltage signal V_{DC} are the variables to control the gas injection. The dependence of N_{H_2} on the valve setting is shown in Fig. 3.9.
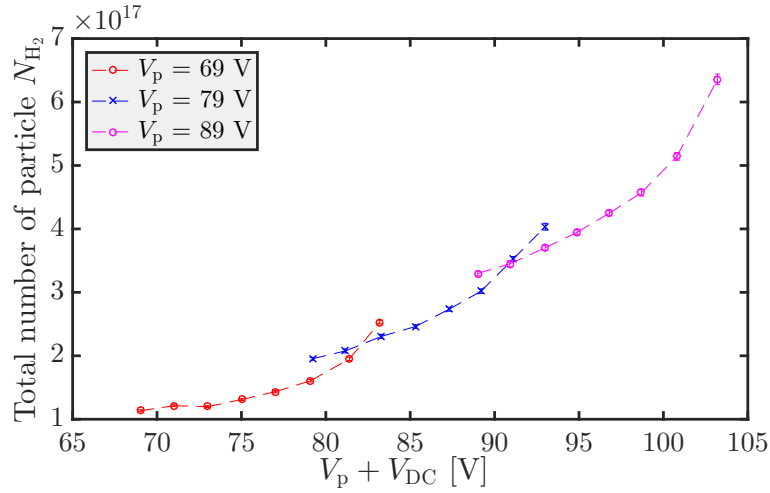
Fig. 3.9   The dependence of N_{H_2} on the valve setting [39].

3.2.4   Measurement Methods

Determination of Plasma Impedance

The impedance of the load and the plasma can be determined by the forward and reflected voltage signals. The reversed/forward voltage signals are expressed as follows:

$$\tilde{V}_r = V_r \exp\left[i(\omega t + \phi_r)\right], \tag{3.12}$$

$$\tilde{V}_f = V_f \exp\left[i(\omega t + \phi_f)\right]. \tag{3.13}$$

where V_r and V_f are the amplitude of the signals and $\phi_r - \phi_f = \phi$ gives the phase differences between the reflected and forward signals. Since those reflected and forward signals are obtained at directional coupler, the electrical delay θ due to the coaxial cable installed between the directional coupler and the matching box is to be taken into account in order to calculate the total impedance Z_M (sum of the matching box and the plasma). Therefore the reflection coefficient between the cable and the matching box Γ_M can be written as

$$\Gamma_M = \frac{\tilde{V}_r e^{-i\omega\theta}}{\tilde{V}_f e^{i\omega\theta}} \tag{3.14}$$

$$= \frac{V_r}{V_f} \exp\left[i(\phi - 2\omega\theta)\right] \tag{3.15}$$

$$= \frac{Z_M - Z_{\text{cable}}}{Z_M + Z_{\text{cable}}}, \tag{3.16}$$

where the impedance of the cable Z_{cable} is 50 Ω. Thus the total impedance Z_M can be defined as

$$Z_M = Z_{\text{cable}} \frac{V_f + V_r\exp\left[i(\phi - 2\omega\theta)\right]}{V_f - V_r\exp\left[i(\phi - 2\omega\theta)\right]}. \tag{3.17}$$

The plasma can be modeled as the sum of the inductance $L_{\text{pl.}}$ and resistance $R_{\text{pl.}}$ connected to the antenna in series as shown in Fig. 3.2.4. Since the total impedance of the matching box Z_M is calculable as mentioned above, the complex impedance of the plasma $Z_{\text{pl.}}$ also can be calculated by subtracting the impedances of other components in matching box. The inductance and the resistance of the plasma are defined by the complex impedance $Z_{\text{pl.}}$:

$$R_{\text{pl.}} = \text{Re}\left[Z_{\text{pl.}}\right], L_{\text{pl.}} = \text{Im}\left[Z_{\text{pl.}}\right]/\omega, \tag{3.18}$$

where $\omega = 2\pi_{\text{RF}}$.

The measured plasma impedance $R_{\text{pl.}}$ and $L_{\text{pl.}}$ will be discussed with the equivalent circuit model of the plasma. The model enables us to calculate the analytic plasma impedance R_{ind} and L_{ind}, which are correspond to the measurable impedance $R_{\text{pl.}}$ and $L_{\text{pl.}}$ respectively. The model which is called the transformer model will be briefly summarized in this paper. The detailed description of the model can be found elsewhere [4, 37]. For the modeling, we assume that the plasma inside the chamber is described as a uniform medium whose permittivity ε_p is complex value:

$$\varepsilon_p = 1 - \frac{n_e e^2}{m_e \varepsilon_0} \frac{1}{\omega(\omega - i\nu_{\text{en}})}. \tag{3.19}$$

where e, m_e and ν_{en} are the charge, the mass and the collision frequency of electron, respectively. The collision process with neutrals is assumed to be dominant for ν_{en} because the neutral gas pressure for LINAC4 operation is relatively high. On the basis of the transformer model, the resistance R_{ind} and the inductance L_{ind} are defined as follows:

$$R_{\text{ind}} = \frac{2\pi N^2}{l_{\text{ant}}\omega\varepsilon_0}\text{Re}\left[\frac{ikr_0 J_1(kr_0)}{\varepsilon_p J_0(kr_0)}\right], \tag{3.20}$$

$$L_{\text{ind}} = \frac{\mu\pi r_0 N^2}{l_{\text{ant}}}\left|\frac{1}{J_0(kr_0) - 1}\right|^2 - \frac{R_{\text{plasma}}}{\nu_{\text{en}}}, \tag{3.21}$$

where J_n, $k = k_0\sqrt{\varepsilon_p}$ and r_0 are Bessel function of n-th order, the wave number of the plasma and the outermost radius where the plasma current can flow, respectively. In the case without any external cusp magnets the radius r_0 is considered to be r_c. In our case, however, the radius r_0 is assumed to be smaller than r_c due to the cusp magnets which prevent plasma from flowing in the vicinity of the wall. Although the radius is found to be about half of the

Parameter	Value
C_p	5.1 nF
C_s	1.46 nF
L_s	4.1 μH
L_{ant}	1.7 μH
$R_{ant} + R_s$	1.1 Ω
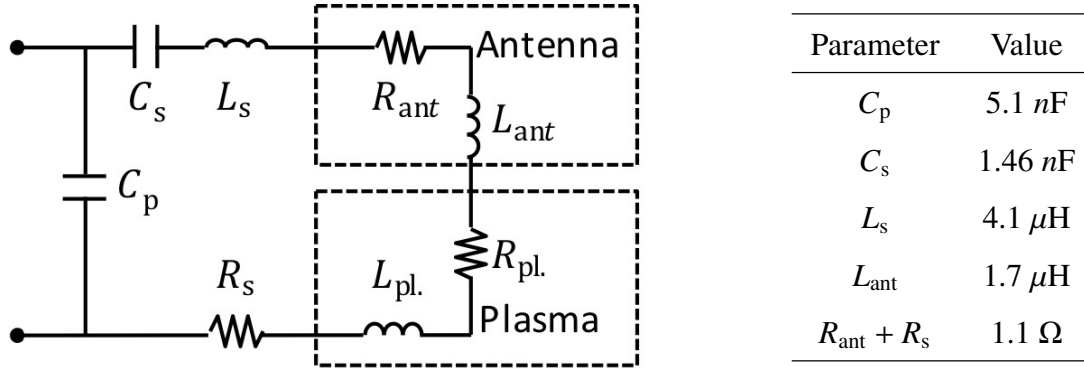
Fig. 3.10 The matching box and the measured parameters.

radius of the chamber under a particular discharge condition by a numerical simulation [14], r_0 is treated as a variable for the parametric survey presented in this paper.

Determination of Plasma Parameters

The plasma parameters are important parameters which determines the impedance of the plasma, which can be evaluated by the OES measurements. The Linac4 H$^-$ source has three view ports at the back end in order to observe the plasma light (see Fig. 3.8). Those view ports are tilted on-axis, 19° and 26° with respect to the cylindrical coordinate axis and the on-axis view port has been used in the measurement. For the evaluation, the Balmer series of atomic hydrogen (the line ratios $R_{\alpha\beta} = H_\alpha/H_\beta$ and $R_{\beta\gamma} = H_\beta/H_\gamma$) have been recorded. The line ratios are acquired from $t = 0.2$ms to $t = 0.3$ms in order to avoid the ignition phase.

The recorded line ratios are analyzed by the collisional radiative (CR) model Yacora H [43]. Yacora H allows to calculate the line ratios for given plasma parameters. Yacora H has been run for many different sets of plasma parameters. The evaluated plasma parameter is defined as the parameters that fit the measured two line ratios. For the sake of simplicity, only the direct excitation due to electron impact has been taken into account to calculate the line ratios (the full evaluation of the discharge parameters can be found in Ref. [44]). Also one has to keep in mind that the evaluated plasma parameters represent axial averaged value.

3.2.5 Results and Discussion

Dependence of Plasma Impedance on Operational Parameters

The plasma impedance is presented in Fig. 3.11 as a function of the RF power coupled to the plasma $P_{pl.}$ ($= P_{fwd} - P_{ref}$). The voltage applied to the piezo valve is set to be $V_p + V_{DC} = 75 + 4$ V in this measurement. The total amount of gas for this setting can be found in Fig. 3.9. From left hand side of Fig. 3.11, it can be seen that the resistance of the plasma $R_{pl.}$ increases as

$P_{\mathrm{pl.}}$ increases. As for the plasma inductance $L_{\mathrm{pl.}}$, it shows negative value. This is because the inductance of an antenna generally decreases with a presence of ICP due to the plasma current which cancels the stored magnetic field inside the antenna. The trend of $L_{\mathrm{pl.}}$ is similar to that of $R_{\mathrm{pl.}}$: it monotonically increases as $P_{\mathrm{pl.}}$ increases. The right hand side of Fig. 3.11 shows the frequency characteristics of the reflection coefficient $|\Gamma_{\mathrm{M}}|$ of the matching box for some $P_{\mathrm{pl.}}$ settings. It has been calculated on the assumption that $R_{\mathrm{pl.}}$ and $L_{\mathrm{pl.}}$ is constant in such small frequency range shown in the figure. The result indicates that the frequency modulation is able to reduce the reflection to 15 % at least. Also it has been found that the effect of the frequency modulation is more significant for higher $P_{\mathrm{pl.}}$ setting. This is because the resistance $R_{\mathrm{pl.}}$ becomes larger when $P_{\mathrm{pl.}}$ increases, which leads to the reduction of the load impedance Z_{M} at the resonant frequency.

The dependence of the plasma impedance has been measured by varying the total amount of gas $N_{\mathrm{H_2}}$. The total amount of gas has been varied by changing the setting of $V_{\mathrm{p}} + V_{\mathrm{DC}}$ from 76 V to 88 V while the power coupled to the plasma $P_{\mathrm{pl.}}$ is fixed to be 40 kW. We define the pressure during the plasma pulse p_{pp} from $N_{\mathrm{H_2}}$ by assuming that the gas temperature is 300 K and the number density of the hydrogen molecule $n_{\mathrm{H_2}} = N_{\mathrm{H_2}}/V_{\mathrm{sc}}$ where V_{sc} denotes the volume of plasma source chamber. In doing so, we can assume that $N_{\mathrm{H_2}}$ shown in Fig. 3.12 correspond to the pressure range from 3.5 Pa to 8 Pa. Although this estimation gives reasonable value compared to the previous pressure measurement [45], please note that this is the simple estimation that may lead to overestimation of the pressure.

The plasma impedance $Z_{\mathrm{pl.}}$ as a function of $N_{\mathrm{H_2}}$ is shown in the left hand side of Fig. 3.12. The tendency of both $R_{\mathrm{pl.}}$ and $L_{\mathrm{pl.}}$ is similar to Fig. 3.11. The right hand side of Fig. 3.12 shows the reflection coefficient $|\Gamma_{\mathrm{M}}|$ for each gas setting. The reflection coefficient has been calculated in the same manner as we mentioned above. It has been found that the reflection can be reduced 16 % at least for the highest gas pressure setting. The result indicates that the frequency modulation is more significant for higher gas pressure setting. This is also because the plasma impedance becomes resistive as the amount of gas increases.

Dependence of Plasma Impedance on Plasma Parameters

The plasma impedance measured in the measurement (Fig. 3.11) is presented in Fig. 3.13 as a function of the electron density n_{e}. Both the electron density n_{e} and the temperature T_{e} have been determined by the line ratio method as mentioned above. As for the electron temperature, however, we only mention that T_{e} is about 5 eV during the measurement because the plasma impedance does not depend on T_{e} as much as n_{e} according to the equivalent circuit model of the plasma. In the measurement, it has been found that the electron density n_{e} is in the range from $0.8 \times 10^{19}/\mathrm{m}^3$ to $1.8 \times 10^{19}/\mathrm{m}^3$. Also the analytic plasma resistance R_{ind} and
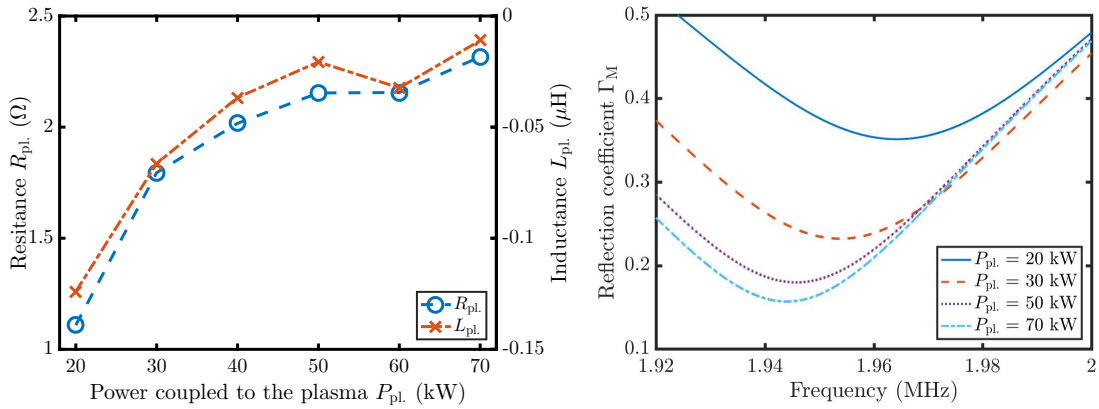
Fig. 3.11   Left: The plasma impedance $R_{pl.}$ and $L_{pl.}$ as a function of the power coupled to the plasma $P_{pl.}$. Right: The frequency characteristics of $|\Gamma_M|$ for the different $P_{pl.}$ settings [39].
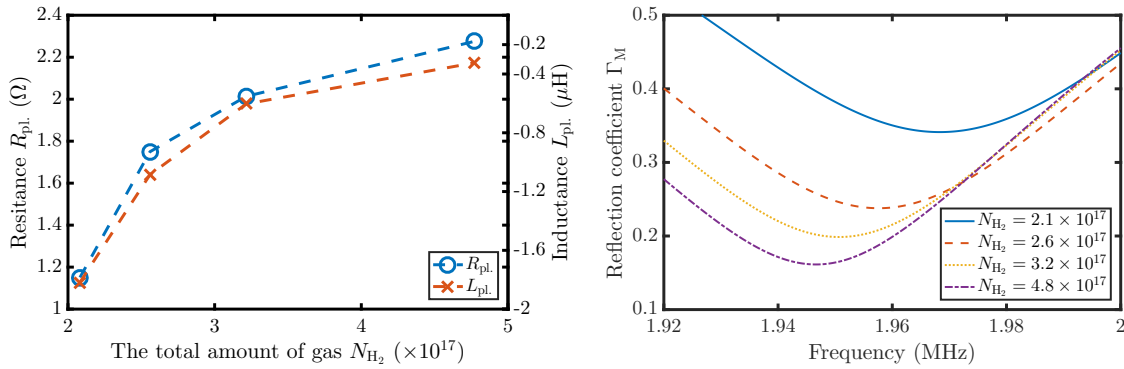
Fig. 3.12   Left: The plasma impedance $R_{pl.}$ and $L_{pl.}$ as a function of the total amount of gas N_{H_2}. Right: The frequency characteristics of $|\Gamma_M|$ for the different N_{H_2} settings [39].

the inductance L_{ind} which is calculated by using Eqs. (3.21) and (3.21) is shown in Fig. 3.14. The results is calculated with a condition that $T_e = 5$ eV, $n_{H_2} = N_{H_2}/V_{sc} = 8.3 \times 10^{20}/m^3$ and the dissociation rate of hydrogen molecules assumed to be 0.5 [46] while the radius r_0 is a variable as we do not have enough information to specify it for each discharge conditions. The calculation result where $r_0 = 14$ mm is shown in the right hand side of Fig. 3.14 as R_{ind} shows qualitative agreement with the measurement. The inductance L_{ind}, however, does not show the peak in the density regime.

From the results shown in Fig. 3.13, one can find that both the resistance $R_{pl.}$ and the inductance $L_{pl.}$ reach their peak where $n_e = 1.1 \times 10^{19}/m^3$. The peaks correspond to the point where the plasma becomes the most resistive load. According to the results of R_{ind}, it can be expected that the plasma shows less resistivity as the plasma density goes higher. As we discussed above, the reflection coefficient cannot be reduced sufficiently only by the frequency modulation when the plasma resistance is low. Thus the results indicates that
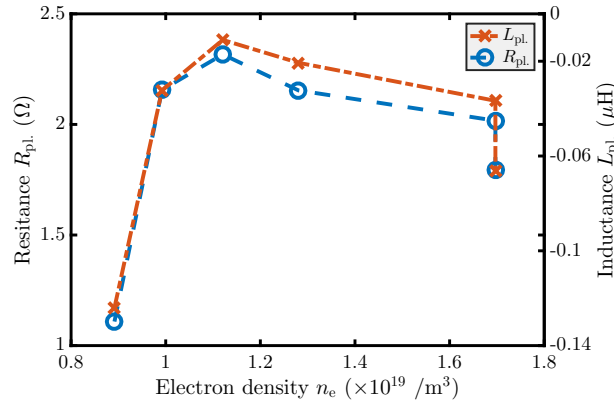
Fig. 3.13   The dependence of the plasma impedance on the electron density n_e [39].
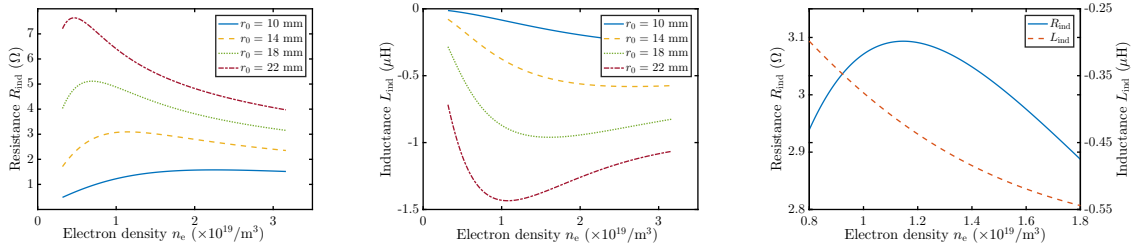
Fig. 3.14   Left: The resistance and center: the inductance of the plasma calculated by the transformer model. Right: the resistance and inductance when $r_0 = 14$mm [39].

the matching box is to be redesigned in order to make the coupling efficiency higher even when the resistance of the plasma is low, which may allow us to produce a denser plasma. Although the analytic model of the plasma that we use is useful to discuss the experimental results, the calculation results strongly depend on the radius r_0 which is difficult to measure as one can see from the center and the left hand side of Fig. 3.14. Thus the model of the plasma impedance which is able to take the realistic distribution of the plasma into account is mandatory for more practical comparison with the measurement.

3.2.6   Conclusion

The measurement of the RF signals and the amount of the hydrogen gas have been carried out in the Linac4 H$^-$ source system in order to investigate the dependence of the load impedance on the operational parameters. Both the RF power coupled to the plasma and the amount of hydrogen gas affect the impedance of plasma impedance. The larger amount of gas and the higher RF power increase the resistance of the plasma while the magnitude of the plasma inductance decreases. Also the results indicate that the effect of frequency modulation on the reflection reduction is more significant when the plasma resistance is higher.

Also the OES measurement have been carried out in order to interpret the results above as

a function of the electron density. It has been found that the resistance and the inductance of the plasma reach their peak where the electron density $n_e = 1.1 \times 10^{19}/m^3$. It has been found that the plasma resistance R_{ind} calculated from the transformer model shows qualitative agreement with the measurement when we assume that the outermost radius of the region where the plasma current can flow is $r_0 = 14$ mm, while the calculated plasma inductance L_{ind} is about an order of magnitude out. According the calculation results, it can be expected that the plasma resistance monotonically decreases in the higher plasma density regime. This indicates that the coupling efficiency cannot be improved only by the frequency modulation. Although the transformer model is the useful tool to discuss the experimental results from analytic point of view, the calculation results strongly depend r_0 which is difficult to obtain from the measurement. Thus the model of the plasma impedance which is able to take the realistic distribution of the plasma into account is mandatory for more practical comparison with the measurement.

Chapter 4

Numerical Modeling of Hydrogen RF-ICP

4.1 Introduction:RF-Code

We have developed a particle-based numerical model of a hydrogen RF ICP (RF-code), which allows us to analyze its discharge process from a kinetic point of view. RF-code is composed of two models, (1) electromagnetic (EM) field model and (2) plasma dynamics model. The former solves the propagation of the EM field around the RF antenna, and the latter solves the motion of the charged particles enforced by the EM field. Those two models are coupled together so that the dynamics of the plasma and the EM field are solved self-consistently. The coupling concept is shown in Fig. 4.1.

As for (1) EM field model, it calculates Maxwell's equation in accordance with the Finite-Difference Time-Domain (FDTD) method [47], which is described in Section 4.2. The EM field is induced by the plasma current and the RF antenna current, which is responsible for the H-mode discharge. In addition, the model takes the electrostatic (ES) field into account. Especially, the ES field due to the RF voltage applied to the antenna (the capacitive field) is responsible for the E-mode discharge.

As for (2) plasma dynamics model, it solves the equation of motion for charged particles, namely e^-, H^+ and H_2^+. The charged particles are tracked while taking various collision processes into account by the Monte Carlo, Null Collision method [48]. This plasma dynamics model is described in Section 4.3.

The coupling of the models (1) and (2) is explained in Section 4.4.
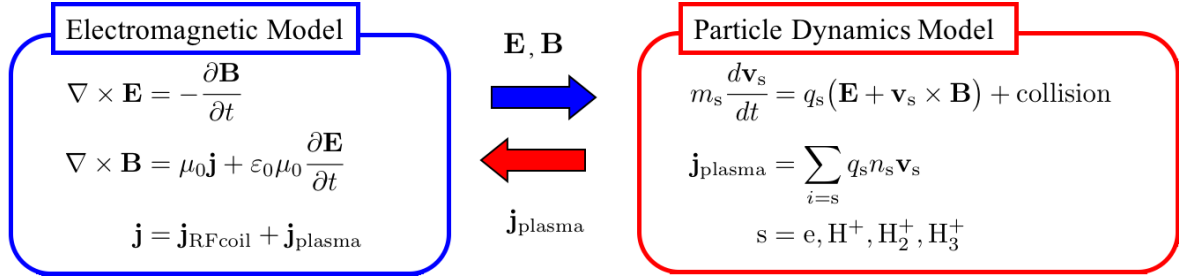
Fig. 4.1   The governing equations of RF code and the coupling of two models.
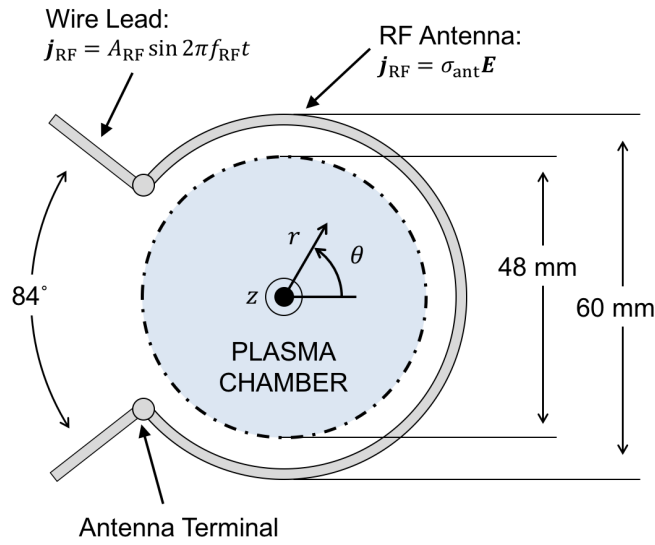
Fig. 4.2   Schematic view of simulation model.

4.2   Electromagnetic Field Model

4.2.1   Geometry of the calculation domain

The schematic drawing of the plasma chamber and the RF antenna is shown in Fig. 4.2. The radii of the plasma chamber r_c and the surrounding RF antenna r_{ant} are determined with reference to that of the CERN's Linac4 H$^-$ source. [24–27] The width of the RF antenna wire is 2 mm. Although the plasma chamber of the H$^-$ source is made of ceramic, its electromagnetic property has been neglected for the simplicity. The EM field due to RF antenna current therefore penetrates to the plasma chamber without any disturbance. Our model assumes that the physical quantities are uniform in the longitudinal direction in the cylindrical coordinates ($\partial/\partial z = 0$) so the plasma chamber and the RF coil are infinitely long in the z-direction. The particle loss in the z-direction may be underestimated compared to the actual plasma.

4.2.2   Finite-Difference Time-Domain method

The Finite-Difference Time-Domain (FDTD) method [47] is the numerical scheme for
EM field analysis in real time domain. The governing equations of the FDTD method are
Maxwell's equations, namely Faraday's law and Ampére's law:

$$\nabla \times \boldsymbol{E} = -\frac{\partial \boldsymbol{B}}{\partial t}, \tag{4.1}$$

$$\nabla \times \boldsymbol{B} = \mu_0 \boldsymbol{j} + \varepsilon_0 \mu_0 \frac{\partial \boldsymbol{E}}{\partial t}. \tag{4.2}$$

These two equations are to be integrated so as not to violate Gauss's law for electricity and
magnetism,

$$\nabla \cdot \boldsymbol{E} = \frac{\rho}{\varepsilon_0}, \tag{4.3}$$

$$\nabla \cdot \boldsymbol{B} = 0. \tag{4.4}$$

Gauss's law for magnetism is satisfied automatically as far as the initial condition is appro-
priately chosen: Since an arbitrary vector $\boldsymbol{a}$ satisfies

$$\nabla \cdot (\nabla \times \boldsymbol{a}) = 0, \tag{4.5}$$

taking divergence of Eq. (4.1) leads to

$$\frac{\partial}{\partial t}(\nabla \cdot \boldsymbol{B}) = 0. \tag{4.6}$$

As for the satisfaction of Gauss's law for electricity is described later.

The RF-code solves the Maxwell's equations in the r-θ plane. Maxwell's equations we

solve for $\boldsymbol{E} = (E_r, E_\theta, E_z)$, $\boldsymbol{B} = (B_r, B_\theta, B_z)$ are therefore written as,

$$\frac{\partial B_r}{\partial t} = -\frac{1}{r}\frac{\partial E_z}{\partial \theta}, \tag{4.7}$$

$$\frac{\partial B_\theta}{\partial t} = \frac{\partial E_z}{\partial r}, \tag{4.8}$$

$$\frac{\partial B_z}{\partial t} = -\frac{\partial E_\theta}{\partial r} - \frac{E_\theta}{r} + \frac{1}{r}\frac{\partial E_r}{\partial \theta}, \tag{4.9}$$

$$\frac{\partial E_r}{\partial t} = -\frac{1}{\varepsilon_0}j_r + \frac{1}{\varepsilon_0\mu_0}\cdot\frac{1}{r}\frac{\partial B_z}{\partial \theta}, \tag{4.10}$$

$$\frac{\partial E_\theta}{\partial t} = -\frac{1}{\varepsilon_0}j_\theta - \frac{1}{\varepsilon_0\mu_0}\cdot\frac{\partial B_z}{\partial r}, \tag{4.11}$$

$$\frac{\partial E_z}{\partial t} = -\frac{1}{\varepsilon_0}j_z + \frac{1}{\varepsilon_0\mu_0}\left(\frac{\partial B_\theta}{\partial r} + \frac{B_\theta}{r} - \frac{1}{r}\frac{\partial B_r}{\partial \theta}\right). \tag{4.12}$$

The current density $\boldsymbol{j} = (j_r, j_\theta, j_z)$ in the above equations is the one flowing in the RF antenna $\boldsymbol{j}_{\mathrm{RF}}$ and the plasma current density $\boldsymbol{j}_{\mathrm{pl.}}$. The plasma current density is calculated by the plasma dynamics model described in Section 4.3. The current I_{RF} is inputted to the RF antenna and defined as,

$$I_{\mathrm{RF}} = I_0 \sin 2\pi f_{\mathrm{RF}} t, \tag{4.13}$$

where I_0 and f_{RF} are the amplitude of the current and the frequency of the RF current, respectively. The current density in the RF antenna $\boldsymbol{j}_{\mathrm{RF}}$ is calculated by Ohm's law so that the voltage drop between the antenna terminals and the resultant electric field can be taken into account self-consistently:

$$j_{\mathrm{RF}} = \begin{cases} \sigma_{\mathrm{ant}}E, & \text{on the antenna} \\ \pm A_{\mathrm{RF}} \sin 2\pi f_{\mathrm{RF}} t, & \text{on the wire leads} \end{cases} \tag{4.14}$$

here σ_{ant} is the conductivity of the RF antenna and A_{RF} is the coefficient corresponds to the amplitude of input current I_0. It can be assumed that σ_{ant} is constant in the RF range as long as the antenna is made of a typical metal ($\sigma \approx 10^7$ S/m) since the charge in the antenna relaxes within much shorter time than one RF cycle.

We derive the discretization form of Eqs. (4.7) - (4.12). Those partial differential equations are discretized by using central-difference approximations to the space and time. The resulting differential equations are solved by a leap-frog method [49] both in space and time as shown in Figs. 4.3 and 4.4. The resulting form of differential equation of Maxwell's
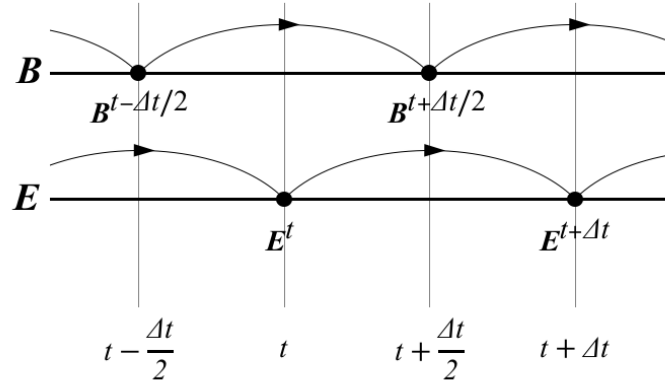
Fig. 4.3   Time lines used in FDTD method.

equations can be written as follows:

$$B_r^{n+1/2}(i, j) = B_r^{n-1/2}(i, j) - \frac{\Delta t}{i \Delta r \Delta \theta} \left[E_\theta^n(i, j + \frac{1}{2}) - E_\theta^n(i, j - \frac{1}{2}) \right], \tag{4.15}$$

$$
\begin{aligned}
B_\theta^{n+1/2}(i + \frac{1}{2}, j + \frac{1}{2}) &= B_\theta^{n-1/2}(i + \frac{1}{2}, j + \frac{1}{2}) \\
&+ \frac{\Delta t}{\Delta r} \left[E_z^n(i + 1, j + \frac{1}{2}) - E_z^n(i, j + \frac{1}{2}) \right],
\end{aligned}
\tag{4.16}
$$

$$
\begin{aligned}
B_z^{n+1/2}(i + \frac{1}{2}, j) &= B_z^{n-1/2}(i + \frac{1}{2}, j) \\
&- \frac{\Delta t}{\Delta r} \left[E_\theta^n(i + 1, j) - E_\theta^n(i, j) \right] \\
&- \frac{\Delta t}{(2i + 1)\Delta r} \left[E_\theta^n(i + 1, j) + E_\theta^n(i, j) \right] \\
&+ \frac{2\Delta t}{(2i + 1)\Delta r \Delta \theta} \left[E_r^n(i + \frac{1}{2}, j + \frac{1}{2}) - E_r^n(i + \frac{1}{2}, j - \frac{1}{2}) \right],
\end{aligned}
\tag{4.17}
$$
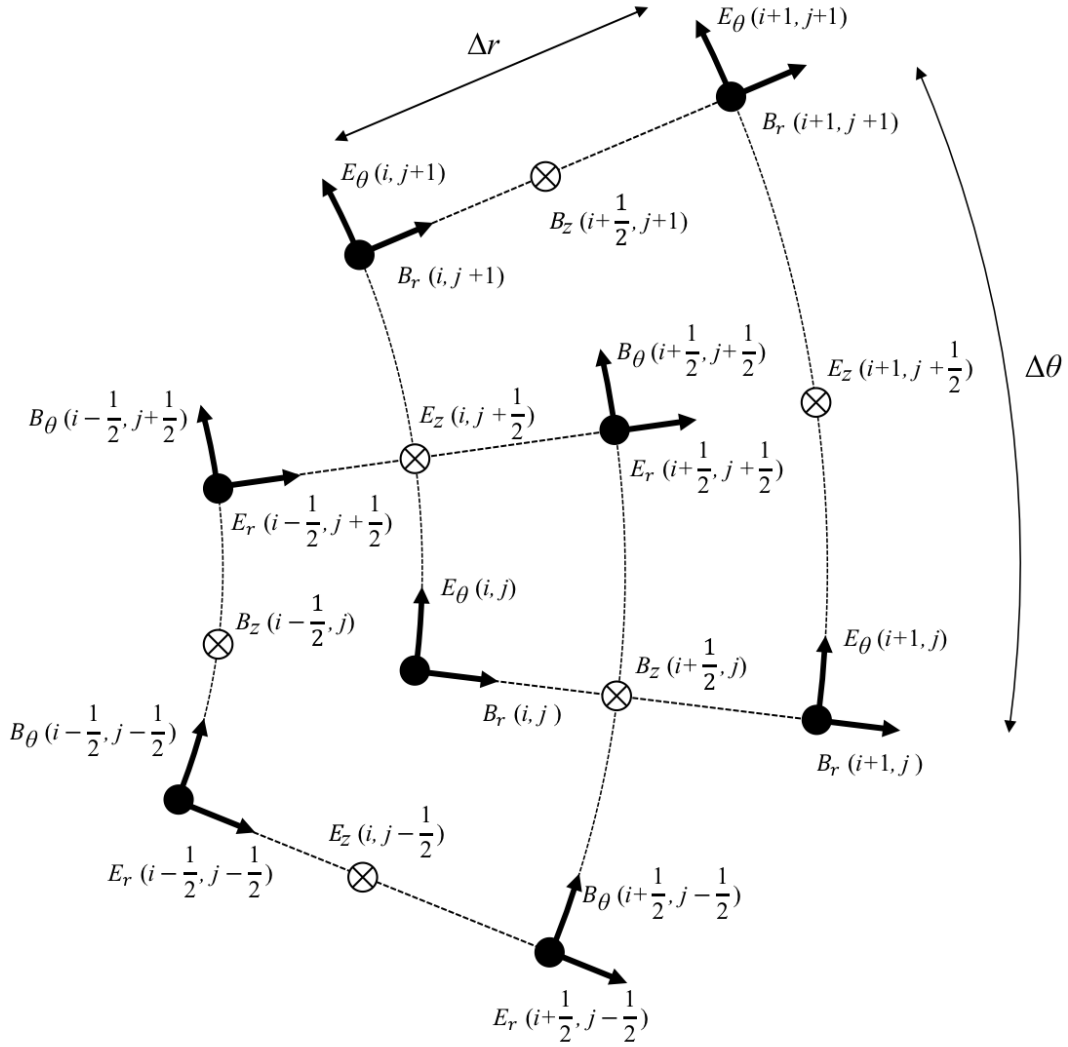
Fig. 4.4   Space configuration of electromagnetic field used in FDTD method.

$$
E_r^{n+1}(i + \frac{1}{2}, j + \frac{1}{2}) = E_r^n(i + \frac{1}{2}, j + \frac{1}{2}) - \frac{\Delta t}{\varepsilon_0} j_r^{n+1/2}(i + \frac{1}{2}, j + \frac{1}{2})
$$

$$
- \frac{1}{\varepsilon_0 \mu_0} \frac{2\Delta t}{(2i + 1)\Delta r \Delta\theta} \left[B_z^{n+1/2}(i + \frac{1}{2}, j + 1) - B_z^{n+1/2}(i + \frac{1}{2}, j) \right],
$$

(4.18)

$$E_\theta^{n+1}(i, j) = E_\theta^n(i, j) - \frac{\Delta t}{\varepsilon_0} j_\theta^{n+1/2}(i, j)$$

$$- \frac{1}{\varepsilon_0 \mu_0} \frac{\Delta t}{\Delta r} \left[B_z^{n+1/2}(i + \frac{1}{2}, j) - B_z^{n+1/2}(i - \frac{1}{2}, j) \right], \tag{4.19}$$

$$E_z^{n+1}(i, j + \frac{1}{2}) = E_z^n(i, j + \frac{1}{2}) - \frac{\Delta t}{\varepsilon_0} j_z^{n+1/2}(i, j + \frac{1}{2})$$

$$+ \frac{\Delta t}{\varepsilon_0 \mu_0} \left[\frac{1}{\Delta r} \left(B_\theta^{n+1/2}(i + \frac{1}{2}, j + \frac{1}{2}) - B_\theta^{n+1/2}(i - \frac{1}{2}, j + \frac{1}{2}) \right) \right.$$

$$+ \frac{1}{2i\Delta r} \left(B_\theta^{n+1/2}(i + \frac{1}{2}, j + \frac{1}{2}) + B_\theta^{n+1/2}(i - \frac{1}{2}, j + \frac{1}{2}) \right)$$

$$\left. - \frac{1}{2i\Delta r \Delta \theta} \left(B_r^{n+1/2}(i, j + 1) - B_r^{n+1/2}(i, j) \right) \right], \tag{4.20}$$

where the index n stands for time $t = n\Delta t$ and (i, j) stands for the location in space $(r, \theta) = (i\Delta r, j\Delta \theta)$.

The time step and the cell size are determined in accordance with the Courant-Friedrichs-Lewy (CFL) condition [50],

$$v\Delta t \leq \frac{1}{\sqrt{\left(\frac{1}{\Delta r} \right)^2 + \left(\frac{1}{\Delta r \Delta \theta} \right)^2}}. \tag{4.21}$$

where v is the speed of light in the case of the Maxwell's equations. The time step and the cell size are chosen so as to satisfy Eq. (4.21) and resolve the phenomena which are of interest.

4.2.3 Gauss's law for electricity

Since Eqs. (4.1) and (4.2) do not include the Gauss's law for electricity, an additional correction process is required so as to calculate the electrostatic field properly [49]. The model corrects the calculated electric field $\tilde{E}$ to E_c which accurately satisfies Gauss's law.

When the potential due to E_c differs from $\tilde{E}$ by $\delta\phi$,

$$E_c = \tilde{E} - \nabla \delta\phi. \tag{4.22}$$

As $\boldsymbol{E}_c$ satisfies Gauss's law,

$$\nabla \cdot \boldsymbol{E}_c = \frac{\rho}{\varepsilon_0},$$ (4.23)

where ρ is the charge density of the plasma. Combining Eqs. (4.22) and (4.23), we obtain the Poisson's equation for the potential difference $\delta\phi$,

$$\nabla^2 \delta\phi = \nabla \cdot \tilde{\boldsymbol{E}}_c - \frac{\rho}{\varepsilon_0}.$$ (4.24)

The Poisson's equation is also discretized in the same manner as Eqs. 4.1 and 4.2, and solved based on the Successive Over-Relaxation (SOR) method.

4.2.4   Boundary condition

In the EM field model, the antenna is located in open space. The present model employs the Bayliss-Turkel radiation boundary condition for the radial boundary [51]. The simulation domain is 5 times larger than the antenna radius so that the EM waves that are numerically reflected at the boundary of the domain diminishes before returning back to the antenna and plasma. At the boundary where $r = 0$, E_θ is assumed to be zero and the other components are calculated not to violate Gauss's law.

4.3   Plasma Dynamics Model

4.3.1   Leap-frog method

The equation of motion for charged particles can be written as

$$m\frac{d\boldsymbol{v}}{dt} = q(\boldsymbol{E} + \boldsymbol{v} \times \boldsymbol{B}) + \text{(collision)}, \tag{4.25}$$

$$\frac{d\boldsymbol{r}}{dt} = \boldsymbol{v}. \tag{4.26}$$

Treatment of the collision term is discussed in Sec. 4.3.2. This model solves Eqs. (4.25) and (4.26) for e^-, H^+ and H_2^+, by using leap-frog method [49]. Consequently, the RF-code is available to track each trajectories of all the charged particles in phase space. Each of them is tracked until they reach the chamber wall or is lost by the destructive collision process.

Figure 4.5 shows the concept of the leap-frog method. The method is to update the positions $\boldsymbol{r}(t)$ and velocities $\boldsymbol{v}(t + \Delta t/2)$ at interleaved time points in the manner similar to the FDTD method. Equations (4.25) and (4.26) are discretized using central-difference approximations:

$$\frac{\boldsymbol{v}^{t+\Delta t/2} - \boldsymbol{v}^{t-\Delta t/2}}{\Delta t} = \frac{q}{m}\left(\boldsymbol{E}^t + \boldsymbol{v}^t \times \boldsymbol{B}^t\right)$$

$$= \frac{q}{m}\left(\boldsymbol{E}^t + \frac{\boldsymbol{v}^{t+\Delta t/2} + \boldsymbol{v}^{t-\Delta t/2}}{2} \times \boldsymbol{B}^t\right), \tag{4.27}$$

$$\frac{\boldsymbol{r}^{t+\Delta t} - \boldsymbol{r}^t}{\Delta t} = \boldsymbol{v}^{t+\Delta t/2},$$

$$\boldsymbol{r}^{t+\Delta t} = \boldsymbol{r}^t + \boldsymbol{v}^{t+\Delta t/2} \cdot \Delta t. \tag{4.28}$$

Note that the velocity $\boldsymbol{v}^t$ on the RHS of Eq. (4.27) is calculated by interpolating using $\boldsymbol{v}^{t+\Delta t/2}$ and $\boldsymbol{r}^{t+\Delta t}$.

RF-code employs the Boris-Buneman version of the leap-frog method [49]. The method treats the motion due to the electric field and rotation due to the magnetic field seperately. Hereafter, we newly define $\boldsymbol{v}^-$ and $\boldsymbol{v}^+$ as follows:

$$\boldsymbol{v}^{t-\Delta t/2} = \boldsymbol{v}^- - \frac{q\boldsymbol{E}^t}{m} \cdot \frac{\Delta t}{2}, \tag{4.29}$$
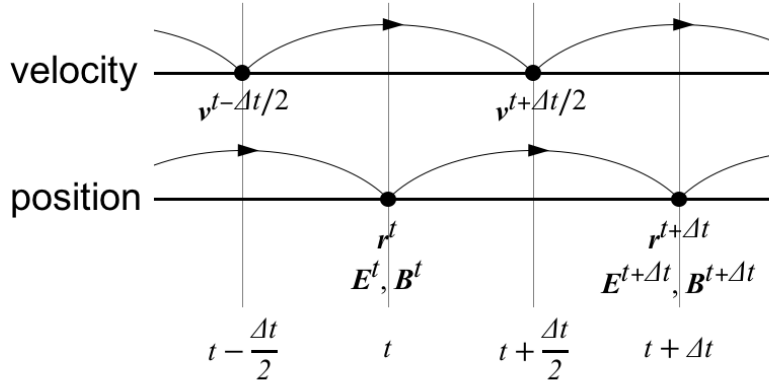
Fig. 4.5   Conceptual diagram of Leap frog method.

$$v^{t+\Delta t/2} = v^+ + \frac{qE^t}{m} \cdot \frac{\Delta t}{2}. \tag{4.30}$$

By using the newly defined velocities, Eq. (4.27) becomes

$$\frac{v^+ - v^-}{\Delta t} + \frac{qE}{m} = \frac{q}{m}\left(E + \frac{v^+ + v^-}{2} \times B\right). \tag{4.31}$$

Therefore,

$$\frac{v^+ - v^-}{\Delta t} = \frac{q}{2m}(v^+ + v^-) \times B. \tag{4.32}$$

Multiplying Eq. (4.32) by $(v^+ + v^-)$, one can find that it expresses the rotational motion due to magnetic field:

$$\frac{|v^+|^2 - |v^-|^2}{\Delta t} = \frac{q}{2m}[(v^+ + v^-) \times B] \cdot (v^+ + v^-) = 0, \tag{4.33}$$
$$\therefore |v^+| = |v^-|.$$

The magnitude of velocity is constant, while only the direction has been changed. As shown in Fig. 4.6, its rotation angle can be calculated by the equation,

$$\left|\tan\frac{\theta}{2}\right| = \left|\frac{v_\perp^+ - v_\perp^-}{v_\perp^+ + v_\perp^-}\right|, \tag{4.34}$$

where $v_\perp^-, v_\perp^+$ are the velocities perpendicular to magnetic field before and after the rotation,
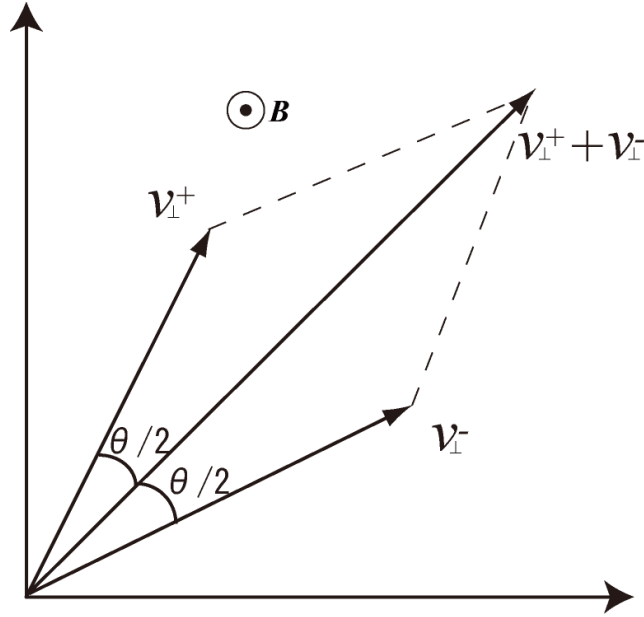
Fig. 4.6   Diagram of velocity rotation in space, showing how $\tan(\theta/2)$ is obtained.

respectively. Taking the magnitudes of Eq. (4.33) leads to

$$\frac{|v^+ - v^-|}{\Delta t} = \frac{q}{2m}\left|(v^+ + v^-) \times B^t\right| \tag{4.35}$$

$$= \frac{q}{2m}\left|v_\perp^+ + v_\perp^-\right|\left|B^t\right|.$$

By using the relation $|v^+ - v^-| = \left|v_\perp^+ - v_\perp^-\right|$, the equation can also be written as

$$\left|\frac{v_\perp^+ - v_\perp^-}{v_\perp^+ + v_\perp^-}\right| = \frac{qB}{m}\frac{\Delta t}{2}, \tag{4.36}$$

$$B \equiv \left|B^t\right|.$$

From Eqs. (4.34) and (4.36), the rotation angle θ obtain simplified form:

$$\left|\tan\frac{\theta}{2}\right| = \frac{qB}{m}\frac{\Delta t}{2} \tag{4.37}$$

$$= \omega_c\frac{\Delta t}{2},$$

where ω_c is the cyclotron frequency of the particle.

The update of the velocity v^+ from v^- can be simplified by introducing vectors s, t which
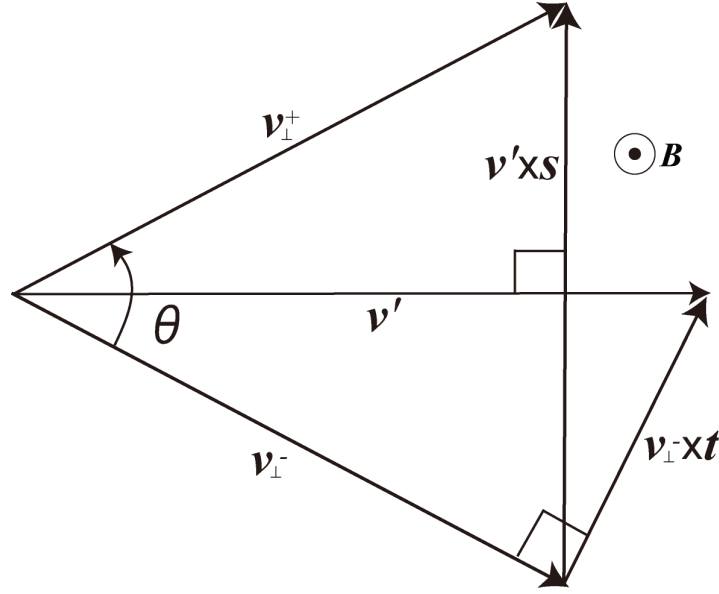
Fig. 4.7   Diagram of velocity rotation in velocity space.

are shown in Fig 4.7. From the definition of t, the vector v' can be expressed as

$$v' = v^- + v^+ \times t. \tag{4.38}$$

Since the angle between the vectors v' and v^- is $\theta/2$,

$$\left| \tan \frac{\theta}{2} \right| = \frac{|v^- \times t|}{|v^-|} = \frac{|v^-|}{|v^-|}|t| = |t| \,. \tag{4.39}$$

Hence, $t = -\tan \dfrac{\theta}{2}$. By using a vector b whose direction is the same as that of magnetic field B, the relation can also be expressed in vector form,

$$t = b \tan \frac{\theta}{2} = \frac{qB}{m} \frac{\Delta t}{2}. \tag{4.40}$$

On the other hand, from Fig. 4.7, one can find that $v^+ = v' + v' \times s$. Therefore the relation between the vectors t and s is

$$s = \frac{2t}{1 + t^2}. \tag{4.41}$$

By substituting Eq. (4.40), it becomes

$$
\begin{aligned}
s &= \frac{2t}{1 + t^2} \\[2ex]
&= \frac{2(-b \tan \frac{\theta}{2})}{1 + \tan^2 \frac{\theta}{2}} \\[2ex]
&= -2b \frac{\sin \frac{\theta}{2} \; \cos^2 \frac{\theta}{2}}{\cos \frac{\theta}{2} \sin^2 \frac{\theta}{2} + \cos^2 \frac{\theta}{2}} \\[2ex]
&= -2b \sin \frac{\theta}{2} \cos \frac{\theta}{2} \\[1ex]
&= -b \sin \theta.
\end{aligned}
\tag{4.42}
$$

In short, the update of the velocity can be calculated by the four equations:

$$
\boldsymbol{t} = \frac{q\boldsymbol{B}^t}{m} \frac{\Delta t}{2},
\tag{4.43}
$$

$$
\boldsymbol{v}' = \boldsymbol{v}^- + \boldsymbol{v}^+ \times \boldsymbol{t},
\tag{4.44}
$$

$$
\boldsymbol{s} = \frac{2t}{1 + t^2},
\tag{4.45}
$$

$$
\boldsymbol{v}^+ = \boldsymbol{v}^- + \boldsymbol{v}^- \times \boldsymbol{s}.
\tag{4.46}
$$

Since the RF-code uses the cylindrical coordinate, these update scheme of position is slightly modified in our code. Figure 4.8 shows the position advance in the cylindrical coordinate. We define variables L_1, L_2, α as follows:

$$
L_1 = r^t + v_r^{t+\Delta t/2} \cdot \Delta t,
\tag{4.47}
$$

$$
L_2 = v_\theta^{t+\Delta t/2} \cdot \Delta t,
\tag{4.48}
$$

$$
\alpha = \arctan\left(\frac{L_2}{L_1}\right),
\tag{4.49}
$$
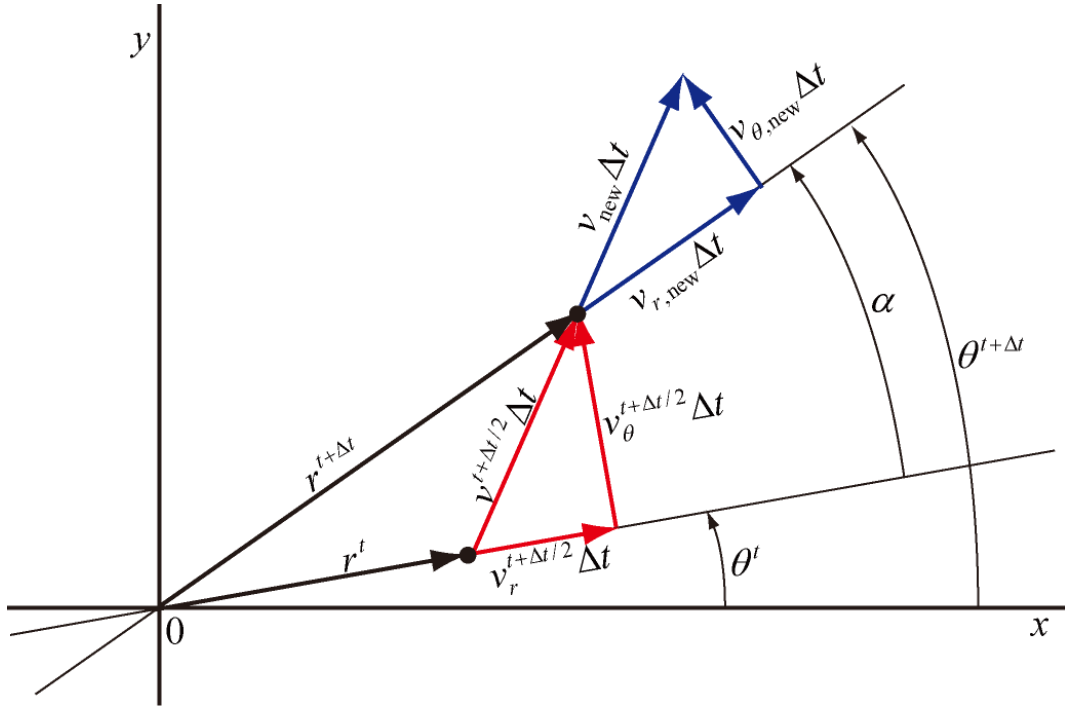
Fig. 4.8   Position advance in cylindrical coordinate.

so that the updated position $r^{t+\Delta t/2} = (r^{t+\Delta t/2}, \theta^{t+\Delta t/2}, z^{t+\Delta t/2})$ can be written as

$$r^{t+\Delta t} = \sqrt{L_1 + L_2}, \qquad (4.50)$$

$$\theta^{t+\Delta t} = \theta^t + \alpha, \qquad (4.51)$$

$$z^{t+\Delta t} = z^t + v_z^{t+\Delta t/2}\Delta t. \qquad (4.52)$$

In the cylindrical coordinates, it is also to be noted that additional velocity update is required due to the update in position. As shown in Fig. 4.8, the relation between the velocity v_{new} and v_{old} is

$$\begin{pmatrix} v_{r,\text{new}} \\ v_{\theta,\text{new}} \end{pmatrix} = \begin{pmatrix} \cos\alpha & \sin\alpha \\ -\sin\alpha & \cos\alpha \end{pmatrix} \begin{pmatrix} v_{r,\text{old}} \\ v_{\theta,\text{old}} \end{pmatrix},$$

$$v_{z,\text{new}} = v_{z,\text{old}}. \qquad (4.53)$$

One has to be careful not to use v_{old} for velocity update and to use v_{new} instead.

4.3.2   Collision processes

The momentum change of a charged particle due to elastic/inelastic collisions is evaluated every Δt_{coll} s. The collision processes are modeled based on the Monte Carlo, Null-Collision method. Tables 4.1, 4.3 and 4.2 show the collision processes of each charged particle species. The electron-electron (e^--e^-) Coulomb collision process, on the other hand, is not taken into account. It may play an important role in the RF-ICP discharges [52, 53]. Therefore, one has to note that the present model is not applicable to a specific plasma parameter range where the e^--e^- Coulomb collision occurs enough to affect the plasma parameter.

4.3.3   Null collision method

The collision processes in the hydrogen RF-ICP has been modeled in accordance with the null collision method [48]. The null collision method has been proposed by Skullerud in 1968 for the first time [59], which samples a smaller number of the particles to evaluate the collision processes so that its computational cost is faster than the direct Monte-Calro method. The basic concept of the null collision method is described here.

Suppose that test particles would experience N types of collision with the target particles of interest. As the i-th test particle has a kinetic energy ε_i, the total cross section of the possible collision processes is,

$$\sigma_{\text{T}}(\varepsilon_i) = \sigma_1(\varepsilon_i) + \cdots + \sigma_{\text{N}}(\varepsilon_i). \tag{4.54}$$

Then the i-th test particle experiences a collision process with a probability P_i,

$$P_i = 1 - \exp(-n\sigma_{\text{T}} v_i(\varepsilon_i)\Delta t), \tag{4.55}$$

where n is the density of the target particle and $v_i(\varepsilon_i)$ is the velocity of the i-th test particle. The presence of the collision is judged by using the uniform random variable $\xi_1 (0 \leq \xi_1 \leq 1)$. As the judgment process is performed for all the particles at every time step, the computational cost would be expensive. In order to avoid the redundant judgment process, this method assumes that the i-th test particle does not experience any collision within the pseudo collision time τ, which is defined as,

$$\tau = -\frac{1}{v'} \log \xi_1, \tag{4.56}$$

where v' is the constant collision frequency. The constant collision frequency v' is the maxi-

Table 4.1   Collision processes of electron.

Collision partner	Collision type	Reaction	Ref.
H	Elastic	$e^- + H \rightarrow e^- + H$	[54]
	Electronic excitation	$e^- + H(1s) \rightarrow e^- + H(2s)$	[55]
		$e^- + H(1s) \rightarrow e^- + H(2p)$	[55]
	Ionization	$e^- + H(1s) \rightarrow 2e^- + H^+$	[55]
H_2	Elastic	$e^- + H_2 \rightarrow e^- + H_2$	[56]
	Vibrational excitation	$e^- + H_2(v=0) \rightarrow e^- + H_2(v=1)$	[55]
		$e^- + H_2(v=0) \rightarrow e^- + H_2(v=2)$	[55]
	Electronic excitation	$e^- + H_2(X^1\Sigma_g^+) \rightarrow e^- + H_2(B^1\Sigma_u^+ 2p\sigma)$	[55]
		$e^- + H_2(X^1\Sigma_g^+) \rightarrow e^- + H_2(C^1\Pi_u 2p\pi)$	[55]
		$e^- + H_2(X^1\Sigma_g^+) \rightarrow e^- + H_2(E,F^1\Sigma_g^+)$	[55]
	Dissociation	$e^- + H_2(X^1\Sigma_g^+) \rightarrow e^- + 2H$	[55]
	Dissociative ionization	$e^- + H_2(X^1\Sigma_g^+) \rightarrow 2e^- + H^+ + H$	[55]
	Non-dissociative ionization	$e^- + H_2(X^1\Sigma_g^+) \rightarrow e^- + H_2^+(v)$	[55]
	Dissociative attachment	$e^- + H_2(X^1\Sigma_g^+) \rightarrow H^- + H$	[55]
H_2^+	Dissociative excitation	$e_- + H_2^+ \rightarrow e^- + H^+ + H$	[55]
	Dissociative ionization	$e_- + H_2^+ \rightarrow 2e^- + 2H^+$	[55]
	Dissociative recombination	$e_- + H_2^+ \rightarrow 2H$	[55]

Table 4.2   Collision processes of molecular hydrogen ion H_2^+.

Collision partner	Collision type	Reaction	Ref.
H_2	Charge transfer	$H_2^+ + H_2 \rightarrow H_2 + H_2^+$	[57]
	Collision-Induced Dissociation (CID)	$H_2^+ + H_2 \rightarrow H^+ + H + H_2$	[57]

Table 4.3   Collision processes of atomic hydrogen ion H^+.

Collision partner	Collision type	Reaction	Ref.
H	Elastic	$H^+ + H \rightarrow H^+ + H$	[58]
	Charge transfer	$H^+ + H \rightarrow H + H^+$	[57]
H_2	Elastic	$H^+ + H_2 \rightarrow H^+ + H_2$	[58]
	Charge transfer	$H^+ + H_2 \rightarrow H + H_2^+$	[57]
	Vibrational excitation	$H^+ + H_2(v = 0) \rightarrow H^+ + H_2(v')$	[57]
	Dissociation	$H^+ + H_2(v) \rightarrow H^+ + 2H$	[57]

mum value with respect to the incident energy,

$$v' = n \cdot \max_\varepsilon(\sigma_T(\varepsilon)v). \tag{4.57}$$

This method saves the computational memory as only the particles that have flown more than τ s are sampled.

When the flight time of the test particle excess the pseudo collision time τ, the collision type is chosen by using the uniform random variable $\xi_2(0 \leq \xi_2 \leq 1)$ again. The schematic of the collision type judgment is shown in Fig. 4.9. The particle experiences the j-th collision
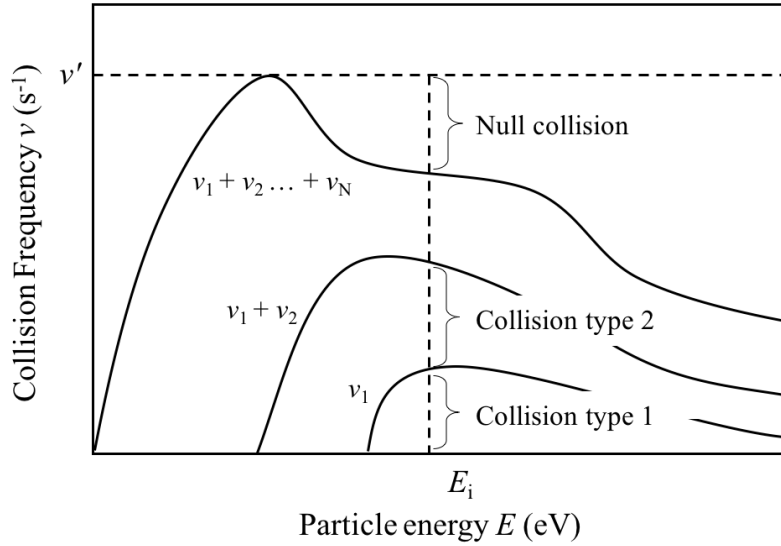
Fig. 4.9   Collision type judgment.

process when the variable ξ_2 satisfies,

$$\frac{\nu_1 + \cdots + \nu_{j-1}}{\nu'} \leq \xi_2 \leq \frac{\nu_1 + \cdots + \nu_{j-1} + \nu_j}{\nu'}, \tag{4.58}$$

where ν_j is the collision frequency of the j-th collision process. The null collision method literally includes the additional collision type, null collision. When the random variable ξ_2 satisfies

$$\frac{\displaystyle\sum_{i=1}^{N} \nu_i}{\nu'} \leq \xi_2, \tag{4.59}$$

the test particle experiences the null collision, which has no physical meaning. In any case, after the collision type judgment, the flight time of the test particle is set as zero, and the collision type judgment will be performed again when the flight time has excessed the pseudo collision time ν. The time step for this collision evaluation Δt_{coll} is determined to be smaller than $1/\nu'$.

4.3.4   Binary collision model

The momentum change of a test particle due to the collision processes are calculated based on the binary collision model, which we describe in this section.

When two particles α and β collide with each other, their momentum changes can be
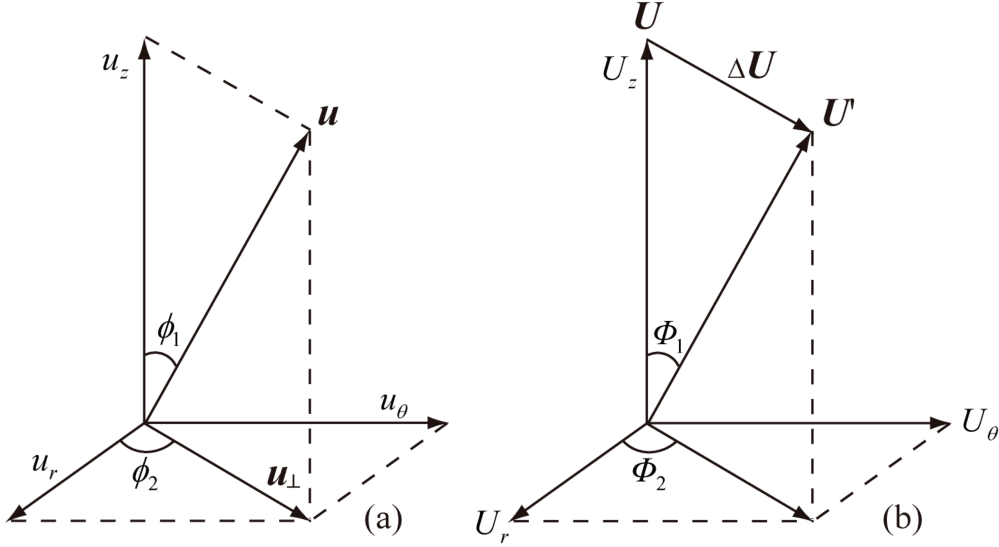
Fig. 4.10 Relative velocity (a) in cylindrical coordinates and (b) in relative velocity coordinates.

calculated as follows.

$$m_\alpha v_\alpha + m_\beta v_\beta = m_\alpha v'_\alpha + m_\beta v'_\beta. \tag{4.60}$$

where m_s, v_s and v'_s $(s = \alpha, \beta)$ are the mass, the velocity before/after the collision, respectively. The velocity v'_s after the collision can be expressed by introducing the relative velocity u $(= v_\alpha - v_\beta)$ and its change Δu $(= u' - u)$ due to the collision:

$$v'_\alpha = v_\alpha + \frac{m_\beta}{m_\alpha + m_\beta} \Delta u, \tag{4.61}$$

$$v'_\beta = v_\beta + \frac{m_\alpha}{m_\alpha + m_\beta} \Delta u. \tag{4.62}$$

The calculation of the change of the relative velocity Δu is simplified by mapping the relative velocity vector u to relative velocity coordinates. By doing so, the relative velocity $u = (u_r, u_\theta, u_z)$ in cylindrical coordinates is transformed to $U = (0, 0, u)$ defined by

$$
\begin{bmatrix} 0 \\ 0 \\ u \end{bmatrix} =
\begin{bmatrix}
\cos\phi_2 \cos\phi_1 & \sin\phi_2 \cos\phi_1 & -\sin\phi_1 \\
-\sin\phi_2 & \cos\phi_2 & 0 \\
\cos\phi_2 \sin\phi_1 & \sin\phi_2 \sin\phi_1 & \cos\phi_1
\end{bmatrix}
\begin{bmatrix} u_r \\ u_\theta \\ u_z \end{bmatrix}, \tag{4.63}
$$

where ϕ_1, ϕ_2 are the angle defined as shown in Fig. 4.10(a). The relative velocity after the collision $\boldsymbol{U'}$ in relative velocity coordinates (shown in Fig. 4.10(b)), can be expressed by the relative velocity $\boldsymbol{u'}$ in cylindrical coordinates,

$$
\boldsymbol{U} = \begin{bmatrix} 0 \\ 0 \\ u \end{bmatrix} \rightarrow \boldsymbol{U'} = \begin{bmatrix} u' \cos \Phi_2 \sin \Phi_1 \\ u' \sin \Phi_2 \cos \Phi_1 \\ u' \cos \Phi_1 \end{bmatrix}, \tag{4.64}
$$

where $|\boldsymbol{u'}| \equiv u'$, and Φ_1 and Φ_2 are the angle defined as shown in Fig. 4.10(b). Then we obtain the change of the relative velocity $\Delta \boldsymbol{U}$ in relative velocity coordinates,

$$
\Delta \boldsymbol{U} = \boldsymbol{U'} - \boldsymbol{U} = \begin{bmatrix} u' \cos \Phi_2 \sin \Phi_1 \\ u' \sin \Phi_2 \cos \Phi_1 \\ u' \cos \Phi_1 - u. \end{bmatrix}. \tag{4.65}
$$

Especially, in the case of the elastic collision where $\boldsymbol{u'} = \boldsymbol{u}$, the velocity change can be expressed as,

$$
\Delta \boldsymbol{U} = u \begin{bmatrix} \cos \Phi_2 \sin \Phi_1 \\ \sin \Phi_2 \cos \Phi_1 \\ \cos \Phi_1 - 1 \end{bmatrix}. \tag{4.66}
$$

As we obtained the change of the velocity in relative velocity coordinate, $\Delta \boldsymbol{u}$ is then to be calculated. When we define the matrix $\boldsymbol{A}$ as

$$
\boldsymbol{A} = \begin{bmatrix} \cos \phi_2 \cos \phi_1 & \sin \phi_2 \cos \phi_1 & -\sin \phi_1 \\ -\sin \phi_2 & \cos \phi_2 & 0 \\ \cos \phi_2 \sin \phi_1 & \sin \phi_2 \sin \phi_1 & \cos \phi_1 \end{bmatrix}, \tag{4.67}
$$

the velocity change of interest can be written as

$$
\Delta \boldsymbol{u} = \boldsymbol{A}^{-1} \cdot \Delta \boldsymbol{U}. \tag{4.68}
$$

In the case of the elastic collision, each component of $\Delta \boldsymbol{u}$ becomes

$$\Delta u_r = \left(\frac{u_r \cdot u_z}{u_\perp} \right) \sin \Phi_1 \cos \Phi_2 - \left(\frac{u \cdot u_\theta}{u_\perp} \right) \sin \Phi_1 \sin \Phi_2 - u_r (1 - \cos \Phi_1), \qquad (4.69)$$

$$\Delta u_\theta = \left(\frac{u_\theta \cdot u_z}{u_\perp} \right) \sin \Phi_1 \cos \Phi_2 - \left(\frac{u \cdot u_r}{u_\perp} \right) \sin \Phi_1 \sin \Phi_2 - u_\theta (1 - \cos \Phi_1), \qquad (4.70)$$

$$\Delta u_z = -u_\perp \sin \Phi_1 \cos \Phi_2 - u_z (1 - \cos \Phi_1). \qquad (4.71)$$

where $u_\perp \ (= \ \sqrt{u_x^2 + u_y^2} \ = \ u \sin \Theta)$ which is shown in Fig. 4.10(a). When $u_\perp \ = \ 0$, the components above become

$$\Delta u_r = u \sin \Phi_1 \cos \Phi_2, \qquad (4.72)$$

$$\Delta u_\theta = u \sin \Phi_1 \sin \Phi_2, \qquad (4.73)$$

$$\Delta u_z = -u(1 - \cos \Phi_1), \qquad (4.74)$$

On the other hand, in the case of inelastic collisions,

$$\Delta u_r = \left(\frac{u' \cdot u_r \cdot u_z}{u \cdot u_\perp} \right) \sin \Phi_1 \cos \Phi_2 - \left(\frac{u' \cdot u_\theta}{u_\perp} \right) \sin \Phi_1 \sin \Phi_2 - u_r (1 - \frac{u'}{u} \cos \Phi_1), \qquad (4.75)$$

$$\Delta u_\theta = \left(\frac{u' \cdot u_\theta \cdot u_z}{u \cdot u_\perp} \right) \sin \Phi_1 \cos \Phi_2 - \left(\frac{u' \cdot u_r}{u_\perp} \right) \sin \Phi_1 \sin \Phi_2 - u_\theta (1 - \frac{u'}{u} \cos \Phi_1), \qquad (4.76)$$

$$\Delta u_z = -\frac{u' \cdot u_\perp}{u} \sin \Phi_1 \cos \Phi_2 - u_z (1 - \frac{u'}{u} \cos \Phi_1). \qquad (4.77)$$

Again, in the case of $u_\perp = 0$,

$$\Delta u_r = u' \sin \Phi_1 \cos \Phi_2, \qquad (4.78)$$

$$\Delta u_\theta = u' \sin \Phi_1 \sin \Phi_2, \qquad (4.79)$$

$$\Delta u_z = -u + u' \cos \Phi_1. \qquad (4.80)$$

Using Eqs. (4.69) - (4.80), RF-code treats the velocity change due to the collision with holding the momentum/energy conservation law. The scattering angles Φ_1 and Φ_2 are determined

by assuming the isotropic scattering. Thereby those angle can be determined as

$$
\begin{aligned}
\Phi_1 &= 2\pi R_1, \\
\cos \Phi_2 &= 1 - 2R_2,
\end{aligned}
\tag{4.81}
$$

where R_1 and R_2 are the uniform random variables. Also, the magnitude of the relative velocity vector after the collision $|\boldsymbol{u}'|$ is to be determined in the case of inelastic collisions. The kinetic energy is consumed as an internal energy so that $|\boldsymbol{u}'|$ becomes

$$
u' = \sqrt{u^2 - \frac{2E_{\text{th}}}{m_{\alpha\beta}}},
\tag{4.82}
$$

where E_{th} is the threshold energy of the inelastic collision and $m_{\alpha\beta}$ is the reduced mass of the two particles of interest.

4.4   Coupling of Plasma Dynamics Model and EM Field Model

4.4.1   Interpolation of EM field and current weighing

The EM field calculated by using the FDTD method is discretized. Therefore, interpolation of the field is required to integrate the equation of motion for charged particles, Eqs (4.25) and (4.26).

As shown in Fig. 4.11, the EM field of a particle is calculated using interpolation from the four closest grid points. By dividing the cell into four area, $S_{11}, S_{12}, S_{21}, S_{22}$, the contributions of each field on the 4 grids are determined. For example, as for the radial component of electric field,

$$
E_\theta(r, z) = \frac{S_{22}}{S}E_\theta(i, j) + \frac{S_{12}}{S}E_r(i + 1, j) + \frac{S_{21}}{S}E_\theta(i, j + 1) + \frac{S_{11}}{S}E_\theta(i + 1, j + 1).
\tag{4.83}
$$

where S ($\equiv S_{11} + S_{12} + S_{21} + S_{22}$) is the total area of the cell. The other components are also calculated in the same manner.

Similarly, current due to the motion of charged particles is to be calculated to integrate Eqs. (4.1) and (4.2) while taken into account the plasma current. The contribution of the plasma
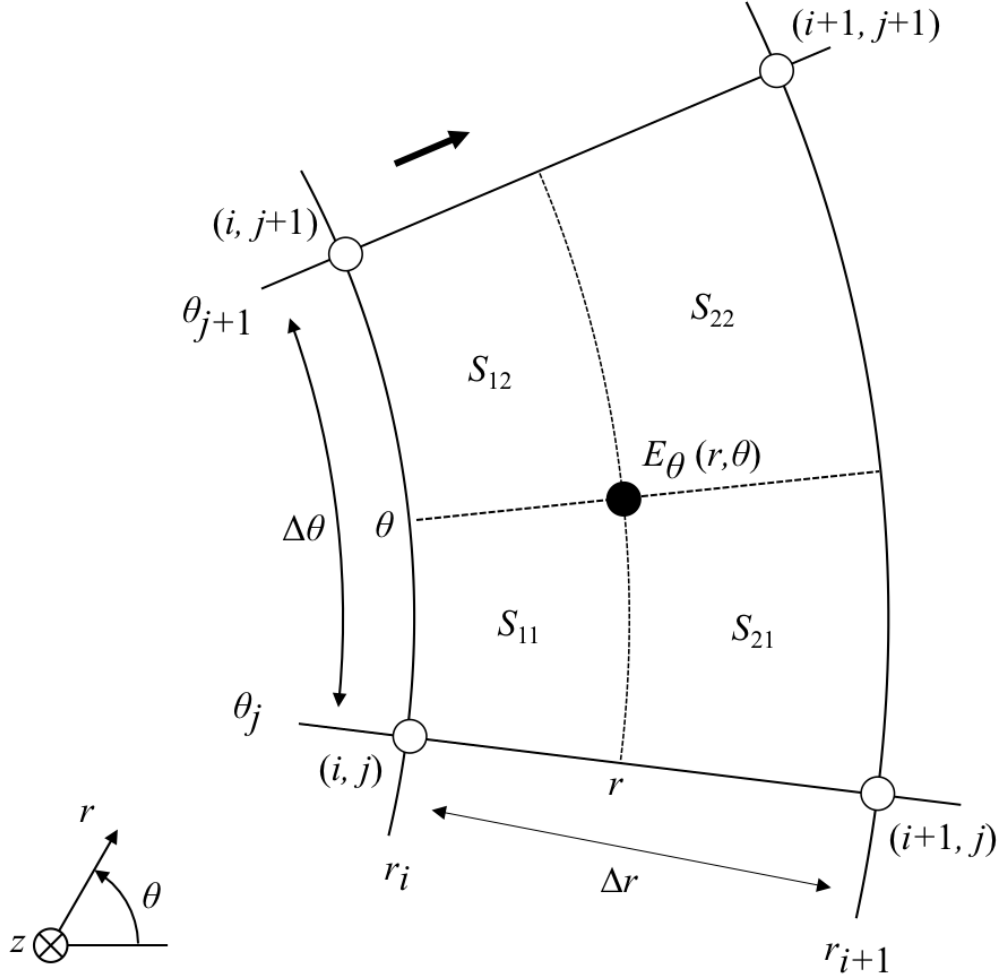
Fig. 4.11   Interpolation of electromagnetic fields and allocation of a charge.

current to a grid can also be calculated by using the four divided area, S_{11}, S_{12}, S_{21}, and S_{22}:

$$S_{11} = \frac{(r^2 - r_i^2)(\theta - \theta_j)}{2}, \tag{4.84}$$

$$S_{21} = \frac{(r_{i+1}^2 - r^2)(\theta - \theta_j)}{2}, \tag{4.85}$$

$$S_{12} = \frac{(r^2 - r_i^2)(\theta_{j+1} - \theta)}{2}, \tag{4.86}$$

$$S_{22} = \frac{(r_{i+1}^2 - r^2)(\theta_{j+1} - \theta)}{2}, \tag{4.87}$$

$$S = \frac{(r_{i+1}^2 - r_i^2)\Delta\theta}{2}. \tag{4.88}$$

For example, azimuthal current due to a charged particle l (whose velocity and electric charge are $\boldsymbol{v}$ and q, respectively) is allocated to each grids as follows:

$$
\begin{aligned}
j_{\theta,l}(i, j) &= \frac{V_{22}}{V} \frac{q_l v_{\theta,l}}{r_i \Delta r \Delta \theta}, \\
j_{\theta,l}(i + 1, j) &= \frac{V_{12}}{V} \frac{q_l v_{\theta,l}}{r_{i+1} \Delta r \Delta \theta}, \\
j_{\theta,l}(i, j + 1) &= \frac{V_{21}}{V} \frac{q_l v_{\theta,l}}{r_i \Delta r \Delta \theta}, \\
j_{\theta,l}(i + 1, j + 1) &= \frac{V_{11}}{V} \frac{q_l v_{\theta,l}}{r_{i+1} \Delta r \Delta \theta}.
\end{aligned}
\tag{4.89}
$$

Applying the allocation for all of the charged particles, one obtains the plasma current density on the grid which is calculated for the EM model at the next time step:

$$
\begin{aligned}
j_{\theta}(i, j) &= \sum_l j_{\theta,l}(i, j), \\
j_{\theta}(i + 1, j) &= \sum_l j_{\theta,l}(i + 1, j), \\
j_{\theta}(i, j + 1) &= \sum_l j_{\theta,l}(i, j + 1), \\
j_{\theta}(i + 1, j + 1) &= \sum_l j_{\theta,l}(i + 1, j + 1).
\end{aligned}
\tag{4.90}
$$

As for curvilinear coordinates, however, this simple allocation method yields the numerical error at the boundary or the singular point. Thus RF-code employs the Verboncoeur volume method [60] in order to lessen the error where $r = 0$, r_c.

4.4.2   Calculation procedure

The calculation scheme, which has been described so far, is summarized here. The governing equations are the equation of motion for charged particles and Maxwell's equations. Those are discritised by central-difference approximations:

$$
\frac{\boldsymbol{r}^{n+1} - \boldsymbol{r}^n}{\Delta t} = \boldsymbol{v}^{n+1/2},
\tag{4.91}
$$

$$
\frac{\boldsymbol{v}^{n+1/2} - \boldsymbol{v}^{n-1/2}}{\Delta t} = \frac{q}{m} \left(\boldsymbol{E}^n + \frac{\boldsymbol{v}^{n+1/2} - \boldsymbol{v}^{n-1/2}}{2} \times \boldsymbol{B}^n \right),
\tag{4.92}
$$

$$\frac{\boldsymbol{B}^{n+1/2} - \boldsymbol{B}^{n-1/2}}{\Delta t} = -\nabla \times \boldsymbol{E}^n, \tag{4.93}$$

$$\frac{\boldsymbol{E}^{n+1} - \boldsymbol{E}^n}{\Delta t} = \frac{1}{\varepsilon_0 \mu_0} \nabla \times \boldsymbol{B}^{n+1/2} - \frac{1}{\varepsilon_0} \boldsymbol{j}^{n+1/2}, \tag{4.94}$$

The calculation procedure is as follows:

1) Update of position $\boldsymbol{r}^{n+1}$ from $\boldsymbol{v}^{n+1/2}$ using Eq. (4.91).

$$\boldsymbol{r}^n \xrightarrow{\boldsymbol{v}^{n+1/2}} \boldsymbol{r}^n$$

2) Define the time average of position $\boldsymbol{r}^{n+1/2}$ from $\boldsymbol{r}^n, \boldsymbol{r}^{n+1}$.

$$\boldsymbol{r}^{n+1/2} = (\boldsymbol{r}^{n+1} + \boldsymbol{r}^n)/2$$

3) Calculation of current $\boldsymbol{j}^{n+1/2}$ from $\boldsymbol{r}^{n+1/2}, \boldsymbol{v}^{n+1/2}$.

$$(\boldsymbol{r}^{n+1/2}, \boldsymbol{v}^{n+1/2}) \rightarrow \boldsymbol{j}^{n+1/2}$$

4) Update of electric field $\boldsymbol{E}^{n+1}$ from $\boldsymbol{j}^{n+1/2}, \boldsymbol{B}^{n+1/2}$ using Eq. (4.94).

$$\boldsymbol{E}^n \xrightarrow{\boldsymbol{B}^{n+1/2}, \boldsymbol{j}^{n+1/2}} \boldsymbol{E}^{n+1}$$

5) Update of magnetic field $\boldsymbol{B}^{n+3/2}$ from $\boldsymbol{E}^{n+1}, \boldsymbol{B}^{n+1/2}$ using Eq. (4.93).

$$\boldsymbol{B}^{n+1/2} \xrightarrow{\boldsymbol{E}^{n+1}} \boldsymbol{B}^{n+3/2}$$

6) Dfine the time average of magnetic field $\boldsymbol{B}^{n+1}$ from $\boldsymbol{B}^{n+1/2}, \boldsymbol{B}^{n+3/2}$.

$$\boldsymbol{B}^{n+1} = (\boldsymbol{B}^{n+1/2} + \boldsymbol{B}^{n+3/2})/2$$

7) Update of velocity $\boldsymbol{v}^{n+3/2}$ from $\boldsymbol{E}^{n+1}, \boldsymbol{B}^{n+1/2}$ using Eq. (4.92).

$$\boldsymbol{v}^{n+1/2} \xrightarrow{\boldsymbol{E}^{n+1}, \boldsymbol{B}^{n+1}} \boldsymbol{v}^{n+3/2}$$

Chapter 5

Numerical Analysis of Hydrogen RF-ICP Discharge

5.1 Publication-3: Kinetic Modeling of E-to-H Mode Transition in Inductively Coupled Hydrogen Plasmas [61]

5.1.1 Abstract

Radio Frequency (RF) Inductively Coupled Plasmas (ICPs) are widely known for their two discharge modes, i.e., H-mode and E-mode, where the dynamics of the plasmas are completely different from each other. We have performed a kinetic simulation of a hydrogen plasma discharge in order to clarify the discharge mechanism and the E-to-H transition of the RF ICPs. The numerical simulation results, such as the time variations of spatial distribution of electron density and the power dissipated in the plasma, show the characteristic changes of the plasma dynamics due to E-to-H mode transition. Especially, the drastic change during the mode transition has been observed in the time evolution of the electron energy distribution function (EEDF). The EEDF deviates from a Maxwellian distribution before/after the transition and the deviation is more significant in the E-mode phase. These results indicate the importance of kinetic modeling for the physical understanding of E-to-H transition.

5.1.2 Introduction

The discharges of Radio Frequency (RF) Inductively Coupled Plasmas (ICPs) are made by an RF coil current which surrounds the plasma chamber to induce the electric field inside. It is

widely known that RF ICPs show two discharge modes depending on the operational plasma density, i.e., E-mode and H-mode [3, 4]. When the plasma density is low, the plasma is sustained by the electrostatic (ES) field which is due to the high RF voltage applied between the coil edges. Since the dynamics of the plasma is similar to that of the plasma between parallel capacitors, it is called capacitively coupled plasma and the discharge mode is called E-mode. In contrast to the E-mode, when the plasma density is high, the plasma is sustained by the electromagnetic (EM) field which is induced by the coil current. Thus the plasma is called inductively coupled plasma and the discharge mode is called H-mode. Due to these two distinct discharge modes, the RF ICP shows completely different characteristics depending on the plasma density. Since the RF ICP has long been used in the plasma processing field (RF ICPs for plasma processing are summarized in Ref. [1]), numerous experiments and theoretical studies have been reported to clarify the underlying physics of the two discharge modes and their transition [9, 11, 15, 17, 62].

On the other hand, negative hydrogen ion (H$^-$) sources with the RF ICP are recently getting noticed in other fields. They are applied to the heating of magnetically confined fusion plasmas [34] and to accelerators of high energy particle physics [26] due to their potential for the high density H$^-$ production and also for their high maintainability. In order to improve the operation of the H$^-$ source, a large number of experimental/numerical studies have been performed. [41, 63–68] As for numerical studies, for example, the transport process of the H$^-$ source plasma has been extensively analyzed on the basis of the self-consistent particle simulation in Ref. [65–67]. Although such studies have contributed to the understanding of the H$^-$ production and the extraction physics, the discharge mechanism in hydrogen plasmas has not been understood well because those numerical models neglect the process of RF coupling with the plasma. Further studies to clarify the discharge mechanism of the RF ICP in H$^-$ sources are mandatory to make the operations of hydrogen plasmas more controllable.

The aim of our work is to clarify the mechanism of the RF ICP discharge from a kinetic point of view. We have performed a kinetic simulation of the E-to-H mode transition of a hydrogen RF ICP. In this paper, we provide the simulation results and the discussion of the mode transition. We discuss the mode transition by examining the time evolution/spatial profile of parameters, i.e., plasma density, kinetic energy of plasma, power dissipated in the plasma, which are difficult to obtain experimentally or by simple theoretical/numerical analysis.

5.1.3   Model

Our simulation model has been developed on the basis of an electromagnetic Particle-in-Cell Monte Carlo Collisions method (PIC-MCC). Most part of our simulation model is described
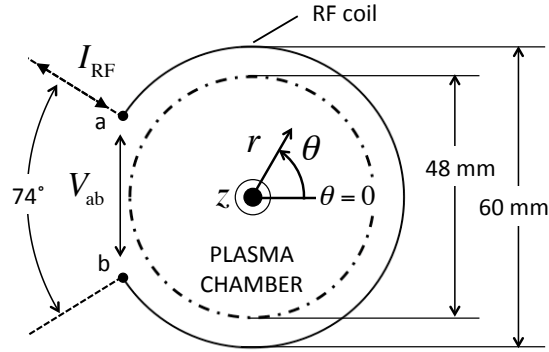
Fig. 5.1   Schematic of plasma chamber and RF coil [61].

in Ref. [69–71]. We summarize the overview of the model, the configuration of the system that we simulate and a few points modified from the previous model in order to take the effect of the capacitive coupling into account.

Our model consists of two parts: the 2D electromagnetic field model and the 2D3V plasma dynamics model. The 2D electromagnetic model employs the Finite Difference Time Domain (FDTD) method [47] to solve the Maxwell's equations, namely Faraday's law and Ampére's law,

$$\nabla \times \boldsymbol{E} = -\frac{\partial \boldsymbol{B}}{\partial t}, \tag{5.1}$$

$$\nabla \times \boldsymbol{B} = \mu_0 \boldsymbol{j} + \varepsilon_0 \mu_0 \frac{\partial \boldsymbol{E}}{\partial t}, \tag{5.2}$$

where j_{RF} and $j_{\mathrm{pl.}}$ are the coil current and the plasma current, respectively. The model of those currents will be described later.

The schematic drawing of the plasma chamber and the surrounding RF coil is shown in Fig. 5.1. For simplicity, this model assumes that the plasma chamber and the RF coil are infinitely long in z-direction. The assumption allows us to solve Maxwell's equations Eqs. (5.1) and (5.2) in the 2D r-θ plane.

Figure 5.2 shows the mesh the present model employs and the location of the electromagnetic field components follows the cylindrical version of the Yee cell [47]. The calculation domain is taken to be 5 times larger than the radius of the RF coil r_{c} so that the EM field reflected at the boundary are negligible. The present model employs Bayliss-Turkel radiation boundary condition for the radial boundary [51].

In addition to Maxwell's equations, the present model solves Poisson's equation because solving only Eqs. (5.1) and (5.2) does not ensure the satisfaction of Gauss's law [49]. Thus the static component of the calculated electric field $\tilde{E}$ must be corrected to that of the electric
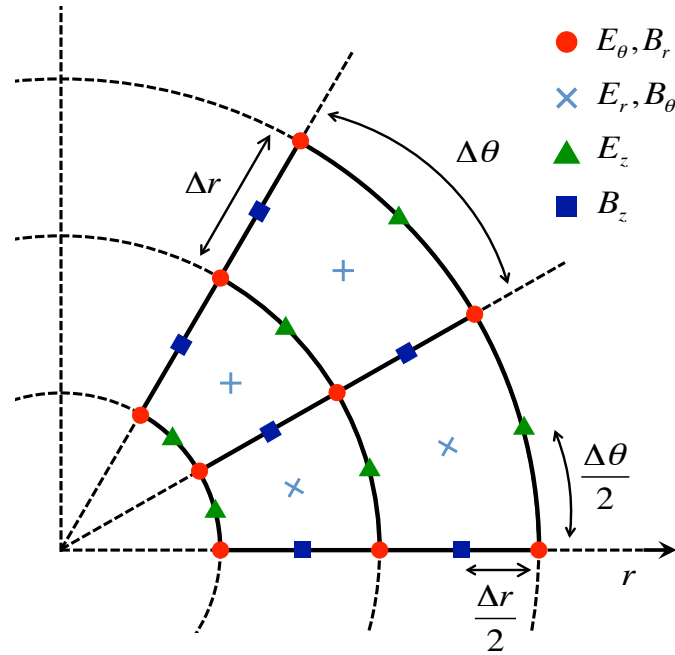
Fig. 5.2   Calculation mesh in the cylindrical coordinate [61].

field $\boldsymbol{E}_{\mathrm{c}}$, which holds Gauss's law, at every time step in the same manner as in Ref. [49]:

$$\boldsymbol{E}_{\mathrm{c}} = \tilde{\boldsymbol{E}} - \nabla \delta \phi, \tag{5.3}$$

$$\nabla \cdot \boldsymbol{E}_{\mathrm{c}} = \frac{\rho}{\varepsilon_0}, \tag{5.4}$$

where $\nabla \delta \phi$ is the difference between the static components of $\boldsymbol{E}_{\mathrm{c}}$ and $\boldsymbol{E}_{\mathrm{t}}$, and ρ is the charge density. Then one can obtain Poisson's equation for $\delta \phi$ by combining Eqs. (5.3) and (5.4),

$$\nabla^2 \delta \phi = \nabla \cdot \tilde{\boldsymbol{E}}_{\mathrm{c}} - \frac{\rho}{\varepsilon_0}. \tag{5.5}$$

The difference $\delta \phi$ is set to be zero at the radial boundary. The detail description of this correction scheme is provided in Ref. [49]. On the other hand, Gauss's law for magnetism is automatically satisfied as long as it holds at the initial condition.

The input coil current I_{RF} is given as a sinusoidal signal, whose frequency f is 13.56 MHz, on the wire leads indicated by broken line of the RF coil in Fig. 5.1. The wire leads are extended towards the boundary of calculation domain. The coil current which flows along the solid line of the RF coil is calculated in order to take into account the surface charge on the coil. We apply Ohm's law ($\boldsymbol{j}_{\mathrm{RF}} = \sigma \boldsymbol{E}$, where $\sigma = 1.0 \times 10^7$ S/m is the conductivity of

the coil) to the region where the RF coil conductor is located. The surface charge yields the voltage drop V_{ab} and the resultant capacitive field between the points a and b.

The plasma current in Eq. (5.2) is calculated by the plasma dynamics model, which solves the equation of motion using the Boris-Buneman method [49] in the 2D3V space in the cylindrical coordinate system:

$$\boldsymbol{j}_{\text{pl.}} = \sum_{s} \sum_{i=1}^{N_s} q_s \boldsymbol{v}_{s,i}, \tag{5.6}$$

$$m_s \frac{d\boldsymbol{v}_s}{dt} = q_s(\boldsymbol{E} + \boldsymbol{v}_s \times \boldsymbol{B}) + (\text{collision}), \tag{5.7}$$

where s ($= \text{e}^-, \text{H}^+, \text{H}_2^+$) are the particle species, m_s and q_s are the mass and the charge of the specie respectively, and N_s is the number of the particles. The motion of electrons is calculated by taking into account the collisions with hydrogen atoms and molecules modeled by the Monte Carlo, Null-Collision method [48]. The collision processes with hydrogen atoms and molecules for ions are to be modeled in the future work. The collision processes that the present model considers are listed in Table 4.1. The main reactions, which play an important role for the electron energy loss such as electronic/vibrational excitation of H_2, are taken into account. The present model will be improved in the future to include other reactions as the simulation model in Ref. [72]. The electron-electron (e^--e^-) Coulomb collisions are not taken into account because the electron-neutral collisions are much more frequent than the e^--e^- Coulomb collisions when the plasma is operated in the high pressure and low plasma density regime. [52] The H_2 gas is treated as a background, which means its pressure and temperature is temporary constant and spatially uniform. The pressure has been systematically varied and 15 Pa has been selected in order to ignite the plasma with the minimum required power. The dissociation degree of the H_2 gas is assumed to be 10 % in the same manner as Ref. [69–71]. The assumption of the dissociation degree is discussed in Section 5.1.5 A. The trajectory of the charged particles will be tracked until the particles reach the chamber wall or are lost by the inelastic collision processes. The input parameters are listed in Table 5.1. We assume that initially (at $t = 0$) the seed plasma is uniformly distributed in the plasma chamber and satisfies charge neutrality:

$$n_{0\text{e}} = n_{0\text{H}^+} + n_{0\text{H}_2^+}, \tag{5.8}$$

where $n_{0\text{e}}$, $n_{0\text{H}^+}$ and $n_{0\text{H}_2^+}$ denote the initial density of electron, H^+ and H_2^+ respectively. The ions are seeded the ratio of H^+ to H_2^+ to be 10 % (see Section 5.1.5 B). The time step Δt is 0.5 ps and the collisions are evaluated every ten time steps, which means $\Delta t_{\text{coll}} = 5$ ps. The time

step for collision evaluations is chosen to satisfy

$$\Delta t_{\text{coll}} \ll {\nu_{\text{max}}}^{-1} \tag{5.9}$$

where ν_{max} is the maximum of the total collision frequency that the present model considers. In our case, ${\nu_{\text{max}}}^{-1} = 1.40$ ns. It has been confirmed that a smaller collision time step than 5 ps does not change the simulation results.

5.1.4   Results

Time evolution of the total power dissipated in the plasma P_{diss}, volume averaged number density n_{s} and kinetic energies E_{s} of each particle species are shown in Figs. 5.3 (a), (b) and (c), respectively. The most notable point is that the trend of these parameters (P_{diss}, n_{s} and E_{s}) changes where $t = 0.15$ s $= t_{\text{EH}}$. This change in trend is the E-to-H discharge mode transition. We hereby define that the plasma is in the E-mode discharge where t < 0.15 μs and in H-mode discharge where t > 0.15 μs.

  Figure 5.4 shows the spatial distribution of the electron density at the phase where the voltage drop V_{ab} becomes the maximum (≈ 3 kV). From Figs. 5.4 (a) and (b) where t < 0.15 μs, one can find that the electrons are transported from one edge of the coil to the other one.

Table 5.1   Main input parameters.

Parameter	Symbol	Value
Radial cell size	Δr	2 mm
Azimuthal cell size	$\Delta \theta$	12°
Time step width	Δt	5×10^{-13} s
Time step width for collision	Δt_{coll}	5×10^{-12} s
Initial electron density	$n_{0\text{e}}$	$1 \times 10^{12}/\text{m}^3$
Initial electron temperature	$T_{0\text{e}}$	300 K
Weight of the test particle	-	5×10^5
Frequency of the antenna current	f	13.56 MHz
Amplitude of antenna current	I_0	$6.9 \times 10^3 \text{A/m}$
H_2 gas pressure	p_{H_2}	15 Pa
H_2 gas temperature	T_{H_2}	300 K
Dissociation degree	-	10 %
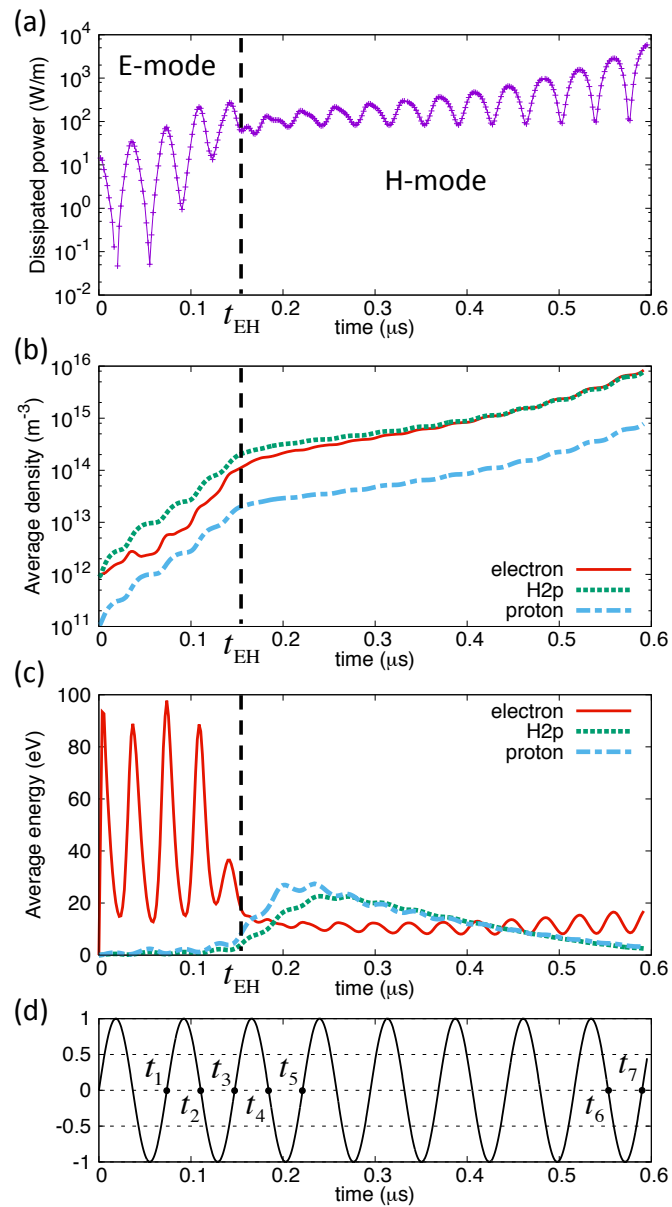
Fig. 5.3   Time evolution of (a) the total power dissipated in the plasma, (b) the volume averaged number density of each particle species and (c) the averaged kinetic energy of each particle species. Normalized input current has been shown in Fig. (d) as a phase reference [61].
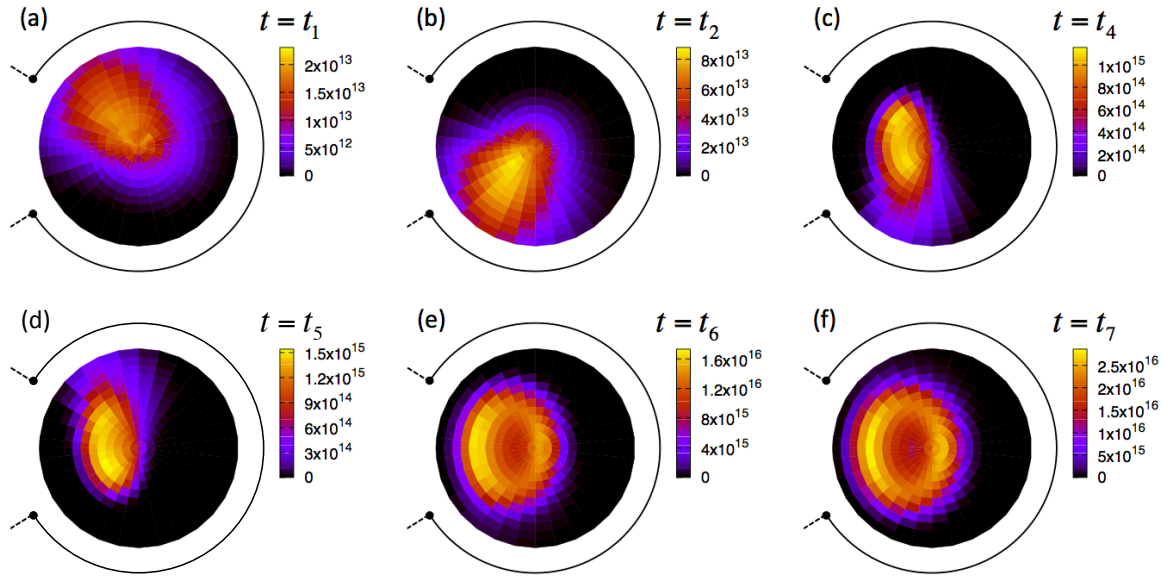
Fig. 5.4   Spatial profiles of electron density where (a) $t_1 = 0.074 \, \mu s$, (b) $t_2 = 0.111 \, \mu s$, (c) $t_4 = 0.184 \, \mu s$, and (d) $t_5 = 0.221 \, \mu s$, (e) $t_6 = 0.553 \, \mu s$, (f) $t_7 = 0.590 \, \mu s$ [61].

This means that the motion of the electrons is determined by the capacitive electric field built up between the coil edges a and b in Fig. 5.1. Hence we regard this phase as the E-mode.

On the contrary, the electrons do not respond to the capacitive field when the plasma is in the H-mode as one can see from Figs. 5.4 (c) - (f). In this phase, the capacitive field inside the plasma starts to decrease since the plasma has grown enough to show the Debye shielding effect. Instead of the capacitive field, the inductive field whose direction is parallel to the coil current dominates in the plasma. This explains why the electron profile starts to shape an arc like structure from $t = t_4$ (Figs. 5.4 (c) and (d)). As the density increases, a full circle has been completed. The profile gets closer to axisymmetric circular profile (Figs. 5.4 (e) and (f)). Hence we regard this phase as the H-mode.

The shielding of the capacitive field affects to the power dissipated in the plasma P_{diss} ($\equiv \int \boldsymbol{j}_{\text{pl.}} \cdot \boldsymbol{E} dV$). The amplitude of P_{diss} decreases once after the transition time t_{EH}. Since P_{diss} is determined by the plasma current and the electric field in the chamber, the shielding of the capacitive field causes the decrease in P_{diss}. As the plasma density increases after the transition, P_{diss} starts to increase again due to the increase in the plasma current. The increase in P_{diss} may continue until the plasma reaches the density regime where the inductive field starts to be shielded.

Figure 5.5 shows the spatial profile of the power density dissipated in the plasma ($p_{\text{diss}} \equiv \boldsymbol{j}_{\text{pl.}} \cdot \boldsymbol{E}$). It also explains the change in the trend of P_{diss} due to the mode transition. When the plasma is in E-mode (Figs. 5.5 (a) and (b)), the power deposition is localized around the edge of the coil where the capacitive field dominates.
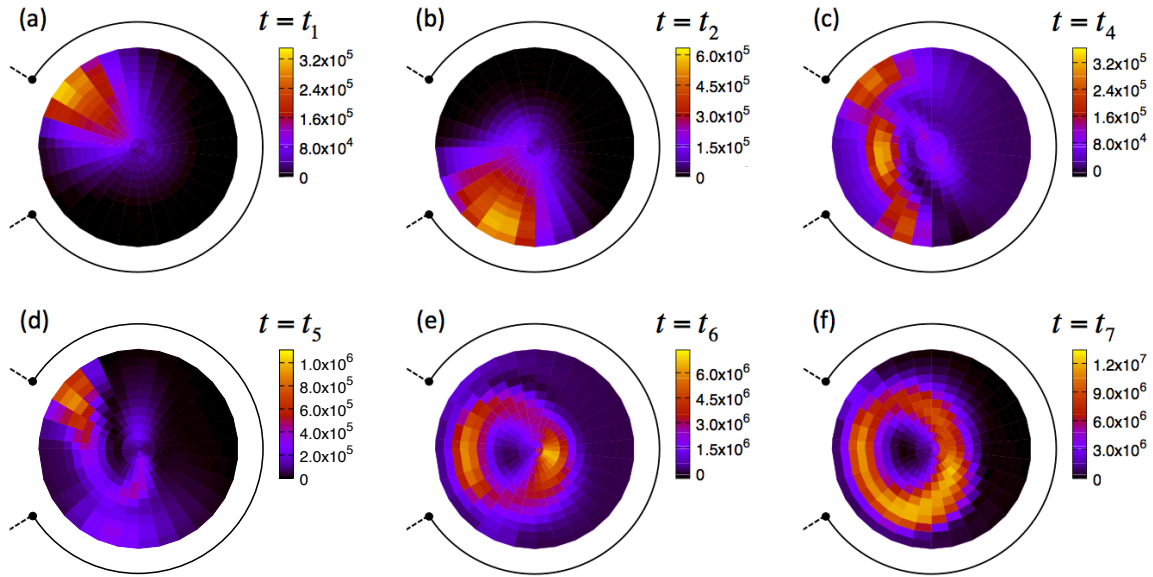
Fig. 5.5   Spatial profiles of power density where (a) $t_1 = 0.074$ μs, (b) $t_2 = 0.111$ μs, (c) $t_4 = 0.184$ μs, and (d) $t_5 = 0.221$ μs, (e) $t_6 = 0.553$ μs, (f) $t_7 = 0.590$ μs [61].

After the transition time t_{EH}, the capacitive field starts to diminish inside the plasma due to the Debye shielding. The Debye length λ_D after the transition, where the electron density $n_e \approx 10^{14}$ /m^3 and the electron temperature $T_e \approx 10$ eV, is 2.3 mm and is 1/10 shorter than the chamber radius r_c. Due to the Debye shielding, the circular current channel starts to form at the center of the discharge region (Figs. 5.5 (c) and (d)), which indicates that the inductive power deposition starts to dominate gradually instead of the capacitive one.

Figure 5.5(e) and (f) shows that the circular current channel has been completed, which means that the plasma is in purely H-mode. The inductive power deposition will increase until the skin effect appears. The skin depth of the plasma can be roughly estimated by assuming that the frequency of RF current f (= 13.56 MHz) is much lower than the maximum of the total collision frequency (= 0.71 GHz): in the high pressure limit, the skin depth of the plasma can be written as [4],

$$\delta = \sqrt{\frac{2m_e \nu_{max}}{\mu_0 \omega n_e q_e^2}} = 2.2 \times 10^7 \times n_e^{-1/2} \text{m}, \tag{5.10}$$

where μ_0 is the permeability of free space and $\omega = 2\pi f$. From Eq. (5.10), the skin depth δ is found to be 9 times larger than the chamber radius where $n_e = 10^{16}$/m^3 which corresponds to the electron density in the last stage of the simulation (see Fig. 5.3(b)). And the skin depth δ is larger for earlier stage. Thus the skin effect does not influence the power deposition during the ignition phase that this paper focuses.

The mode transition has also been observed in the slopes of the time evolution of the plasma densities (Fig. 5.3(b)). The slopes decrease around the transition time t_{EH}. This is simply because P_{diss} falls at t_{EH} as we discussed above. Due to the decrease in P_{diss}, the resultant ionization rate decreases and results in a slower increase in the plasma density.

The effect of mode transition on the averaged kinetic energy appears in a different way depending on the particle species (Fig. 5.3(c)). This can be explained by the existence of the plasma sheath. As for ions, their kinetic energy increases since they accelerate towards the wall due to the sheath potential drop. In the beginning of the transition, when the plasma density is low, the thickness of the sheath is comparable with the radius of the chamber so the large number of ions are accelerated by the sheath potential. As the density increases, the sheath thickness becomes smaller and it is localized close to the chamber wall. Only the ions in the vicinity of the chamber wall are accelerated by the thinner plasma sheath. Therefore the averaged kinetic energy of the ion increases around the transition time t_{EH} and decreases a few cycles after the transition. The decrease in the sheath thickness can be found by comparing Figs. 5.4 (c) and (d) with Figs. 5.4 (e) and (f): The distance from density peak of the electron from the chamber wall around $\theta = \pi$ becomes smaller as the time goes by.

On the other hand, the sheath helps to confine the bulk of the electrons. Due to its potential drop in the vicinity of the chamber wall, only the electrons whose energies are high enough to penetrate the potential drop can escape to the chamber wall. This energy-dependent loss of electrons explains the drastic fall in the averaged kinetic energy of electrons at the transition time t_{EH}.

The confinement by the plasma sheath leads to that the bulk of electrons is apart from the chamber wall (see Fig. 5.4 (c) and (d)). This means that the bulk of electrons starts to be accelerated by the inductive field instead of capacitive field and it can be seen from the distribution of power density dissipated in the plasma (see Figs 5.5 (c) and (d)). Since the magnitude of the inductive field is smaller than that of capacitive field, this replacement of the accelerating field also plays an important role for the decrease in the average energy of electrons.

The explanation of the effect of mode transition on the average kinetic energies can readily be justified by examining the time variation of the potential profile. Figure 5.6 shows the radial distribution of potential difference from the wall at $\theta = \pi$. In the beginning of the mode transition ($t = t_3, t_4, t_5$), the center-to-edge potential difference is more than 200 V and sheath thickness is around 1 cm. This long and large sheath drop accelerates the large number of ions towards the wall while confining the low energy electron. A few cycles after ($t = t_6, t_7$), the potential difference decreases to 150 V and the thickness becomes about 5 mm. This time variation of the potential profile does not contradict the explanation of the mode transition of the kinetic energy we mentioned above.
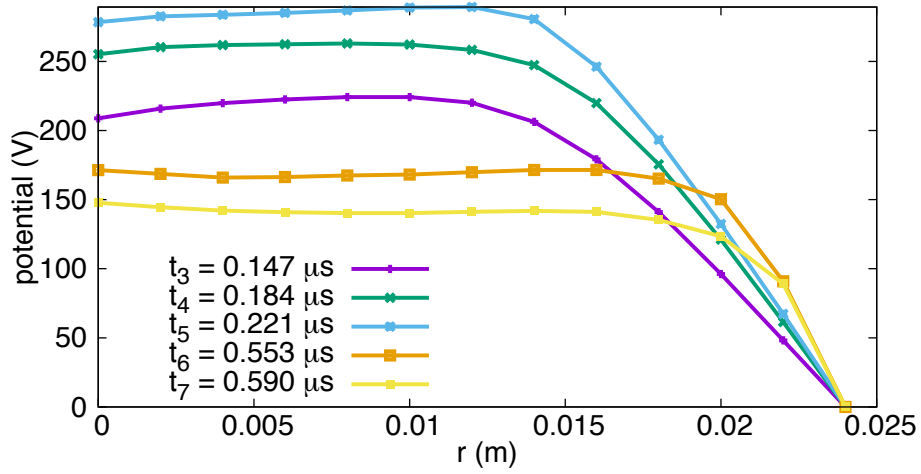
Fig. 5.6   Radial distribution of potential difference from the wall [61].

Figure 5.7 shows the EEDFs before ($t = t_2, t_3$) and after ($t = t_4$) the transition, which are normalized by volume averaged density at each time phase. Each solid line indicates the Maxwellian distribution whose temperature $T(t = t_2, t_3, t_4)$ is estimated by $k_B T(t) \equiv 2/3 E_e(t)$, where E_e is the averaged kinetic energy of electron and k_B is Boltzman constant. Figure 5.7 shows that the ratio of the high energy component to the low energy component decreases during the transition. This justifies our explanation above that the fall of electron energy is caused by the energy-dependent loss of electrons. The effect of the energy-dependence on the plasma dynamics can only be taken into account by the kinetic modeling.

The comparisons between Maxwellian distributions and calculated EEDFs, which are given in Fig. 5.7, have shown that the plasma has a non-equilibrium EEDF. Especially in the E-mode phase (lines (a) and (b)), both low energy and high energy components deviate from Maxwellian and the differences are significant. The fact indicates that the E-mode plasma in our case cannot be treated by the simple fluid model.

5.1.5   Discussion

A. Dissociation Degree of H_2

As mentioned in Section 5.1.3, the dissociation degree of H_2 is fixed to be 10 %. The dissociation degree has been determined based on the experimental results in Ref. [46]. The experiment by S. Briefi, et al., showed that the dissociation degree is approximately 50 % in steady state where the gas pressure is 5 Pa. Since our code simulates the ignition phase with higher pressure, the dissociation degree for our simulation is expected to be lower than 50
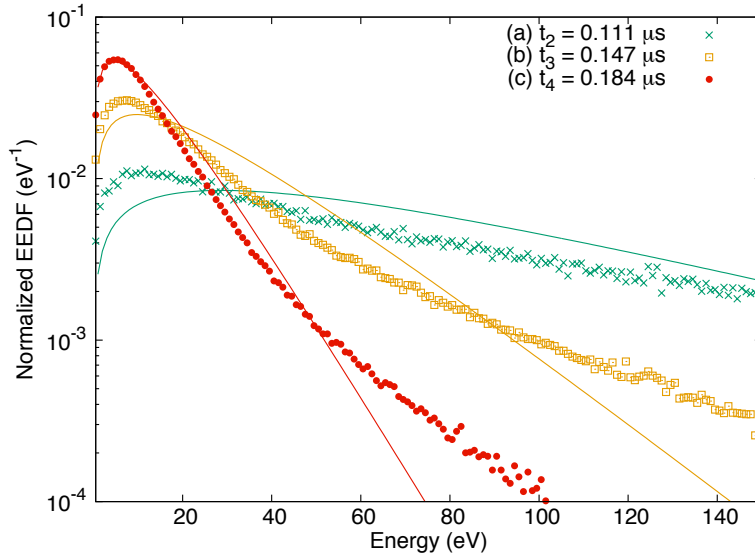
Fig. 5.7   Normalized electron energy distribution functions where (a) $t_2 = 0.111\,\mu s$, (b) $t_3 = 0.147\,\mu s$ and (c) $t_4 = 0.184\,\mu s$. The solid lines indicate the Maxwellian distributions whose average energies are assumed to be equal to those of each calculated EEDFs [61].

%. Furthermore our code doesn't simulate the very beginning of the ignition phase where the electron density is quite low and the dissociation degree is almost zero. Thus we assume that the ratio of atomic density to that of molecular is to be higher than zero, 10 %. However the value 10 % is rough estimation. We have simulated with lower dissociation degree, 0 %. As far as the results shown in Fig. 5.3 concerned, the results do not show any significant difference with the results of 10 % dissociation degree. Although the self-consistent modeling of neutrals coupled with present plasma model will be needed to simulate the RF plasma discharge consistently with the time variable dissociation degree, the main results provided in this paper seem to be valid where the dissociation degree is in the range of 0 -10 % from the above parametric change of the dissociation degree.

B. The initial density ratio of ion species

As mentioned in Section 5.1.3, the initial ratio of H^+ to H_2^+ is assumed to be 10 %. The assumption is based on the rough estimation by the cross sections of the non-dissociative/dissociative ionizations of H_2: the cross section of the non-dissociative ionization is one-order larger than that of dissociative ionization. [55] Thus we assume the density ratio H^+/H_2^+ to be 0.1. The time evolution of H^+ and H_2^+ has calculated based on the reactions listed in Table 4.1. However as discussed in Section 5.1.5 A, the dissociation degree is fixed to be constant in this study. Therefore it is important to develop the model

which solves the time evolution of density for ions and neutrals more self-consistently.

C. Ion-neutral collisions

The present model does not take the ion-neutral collision processes into account. The collision processes may affect some of the results provided in this paper. For example, the spatial profile of electron density may change. The spatial profile of electron is generally affected by the ion density profile, e.g., due to ambipolar diffusion. The region where ionization takes place is localized near the coil edges so that the spatial distribution of ions also localizes. Since these localized ions might be distributed uniformly due to diffusion by collision processes, the electrons might be also distributed more uniformly (see Figs. 5.4 (e) and (f) for example) if the collision processes for ions are taken into account.

D. Effect of H_3^+

It is reported that the distribution of H_2^+ especially in the sheath region is affected by the existence of H_3^+ in the parallel plate capacitive discharge [73]. We do not consider the effect of H_3^+ in this paper. However as for the comparison with the results in Ref. [73], it is difficult to compare directly due to two significant differences between our study and the results of the reference. The first difference is the reference focuses the purely capacitively coupled plasma while our study focuses RF-ICP. The other difference is that the geometry of the reference is completely different from ours, i.e., the reference dealt with the parallel plate while we focus RF-ICP with the cylindrical geometry.

In order to include H_3^+, the collision between H_2^+ and H_2 must be taken into account. Thus the inclusion of ion-neutral collision processes is important from this aspect too, which is left for our future work.

E. Database of the collision cross sections

The collision cross sections that the present model considers are mainly taken from Ref. [55]. The data set of the cross sections is also available in Ref. [74]. The use of cross sections provided in Ref. [74] may change the results. For example, the cross section of dissociative ionization of H_2 is slightly higher than that provided in Ref. [55]. The sensitivity of the results on the cross section data will be needed in the future. The qualitative feature obtained in this paper, however, seems not to be changed largely.

5.1.6   Conclusion and Future Study

The E-to-H mode transition in the hydrogen plasma discharge has been reproduced by the kinetic modeling. The simulation results have shown that the time variations of power dissipated in the plasma, plasma density and kinetic energy are strongly affected by the mode transition. The spatial profile of the electron density also reflects the dynamics of E-mode and H-mode plasmas.

Our model has allowed us to investigate the mode transition from a kinetic point of view. Especially the drastic fall of the kinetic energy of electron during the transition can be observed by the kinetic model. Also, it has been shown that the EEDFs deviate from the Maxwellian distribution and is affected by the sheath formation during the transition. These results indicate the importance of kinetic modeling for the physical understanding of the E-to-H transition in the hydrogen RF ICP.

The above conclusions, however, are based on the various simplifications and assumptions, which are summarized and discussed in Section 5.1.5. These effects will be studied more in detail in the future for more realistic simulation. Also, we plan to extend our model to take into account the effect of the external matching circuit, three dimensional geometry aiming to simulate practical geometries.

5.2   Publication-4: Numerical Analysis of Effects of Ion-Neutral Collision Processes on RF ICP Discharge [75]

5.2.1   Abstract

Discharge process of a Radio Frequency (RF) Inductively Coupled Plasma (ICP) has been modeled by an ElectroMagnetic Particle-in-Cell Monte Carlo Collisions method (EM PIC-MCC). Although the simulation was performed by our previous model so as to investigate the discharge mode transition of the RF ICP from a kinetic point of view, the model neglected the collision processes of ions (H^+, H_2^+) with neutral particles. In this study, the RF ICP discharge process has been investigated by the latest version of the model which takes the ion-neutral collision processes into account. The basic characteristics of the discharge mode transition provided by the previous model have been verified by the comparison between the previous and the present results. As for the H-mode discharge regime, on the other hand, the ion-neutral collisions play an important role in evaluating the growth of the plasma. Also, the effect of the ion-neutral collisions on the kinetic feature of the plasma has been investigated, which has highlighted the importance of the kinetic perspective for the modeling of the RF ICP discharge.

5.2.2   Introduction

Radio Frequency (RF) Inductively Coupled Plasmas (ICPs) have long been utilized for industrial applications, e.g., material processing [1], medical devices [76], particle injectors for accelerators [26] and heating devices for the fusion plasmas [34]. The present study focuses on hydrogen RF ICP in particular because of the increasing demand of negative hydrogen ion (H^-) sources in the accelerator and the fusion fields.

It is well known that the RF ICPs show two distinct discharge modes depending on their operational plasma density [3, 4]. When the plasma density is low, the plasma is operated in the E-mode discharge which is sustained by the electrostatic (capacitive) field due to the voltage drop between the RF antenna terminals. As the plasma density increases, the capacitive field is shielded due to the Debye shielding so that the inductive field produced by the RF current, in turn, starts to sustain the discharge. The discharge is called the H-mode.

The discharge parameters (plasma density/temperature, power deposition, etc.) of the E- and H-mode plasmas significantly differ from each other. The operation of the plasma is

required to be optimized in response to the mode transition. However, the optimization of the RF ICP tends to be a delicate process because its operation depends on the parameters whose behavior are too complex to be predicted, e.g., the discharge mode, the power coupled to the plasma and the plasma density/temperature. This complexity calls for huge R&D efforts on the H^- source development.

To obtain the detailed insight into complex discharge process of RF plasmas, a number of analytic/numerical/experimental studies have been carried out [9, 11, 15–17, 62]. Some of those previous studies have indicated that the kinetic treatment of the RF plasma is mandatory to describe the RF discharge. For example, the electron energy distribution function (EEDF) F_e of the RF plasma can show a non-Maxwellian shape in a specific discharge condition [16], which is difficult to treat by simple analytic/fluid models. We have worked on the development of a particle-based numerical model of a hydrogen RF ICP discharge in an attempt to reduce R&D efforts on the H^- development by examining the RF ICP discharge from a kinetic point of view.

Our numerical model has experienced step-by-step upgrades so as to make our model credible and realistic [52, 61, 69–71]. The recent upgrade, which is reported in Ref. [61], has enabled the model to simulate the E- and H-mode discharges, which is one of the notable features of our numerical model. The E-to-H mode transition of a RF ICP discharge has been investigated by the model from a kinetic point of view. The results obtained by the model have provided detailed information of the RF ICP discharge, such as the spatiotemporal behavior of the discharge parameters before/after the mode transition. All the parameters that we have examined exhibit clear change in their spatiotemporal behavior due to the mode transition.

As for the kinetic energy of the plasma, for example, the results have indicated that the effect of the discharge mode transition arises in a different way depending on the particle species. The time evolution of the volume-averaged kinetic energy of the electron clearly shows the discharge mode as its oscillation reflects the magnitude of the electric field which is coupled to the plasma at the moment. The drastic drop in the oscillation can be seen after the E-to-H mode transition, which reflects the fact that the magnitude of the inductive field is weaker than that of the capacitive one. Also, the simulation results have shown that the EEDF of the plasma in the E-mode can be characterized by its large deviation from the Maxwell distribution and it gradually relaxes to the Maxwell distribution as the plasma density increases towards the H-mode regime. On the other hand, the kinetic energy of ions (H^+ and H_2^+) does not respond to the RF field when the plasma is in the E-mode. As the plasma density increases enough to change into H-mode, the kinetic energy of the ions increases to more than 20 eV. This is because the plasma starts to form a plasma sheath which accelerates the ions towards the chamber wall.

Although we have concluded that the previous model reasonably reproduces the E- and H-

mode discharge and the transition, the collision processes of the ions have been neglected for the simplification. The purpose of the present study is to add such collision processes to our model so as to verify the conclusion we have previously provided in Ref. [61]. This article reports the simulation results from the latest version of our model that includes the ion-neutral collisions and the investigation of the effect of the collision processes, which provides further insight into the RF ICP discharge.

In Section 5.2.3, we summarize the model and the ion-neutral collision processes which are newly taken into account. The results calculated by the upgraded model will be provided in Section 5.2.4 while being compared with ones calculated by the previous model. Our future work related to the model development and the conclusion of this paper are referred in Section 5.2.5.

5.2.3   Model

A numerical simulation code for the cylindrical hydrogen RF-ICP discharge has been developed based on an ElectroMagnetic Particle-in-Cell Monte Carlo Collisions (EM PIC-MCC) method. The simulation code comprises the 2D EM field model and the 2D3V plasma dynamics model. Those two models are solved alternately so as to calculate self-consistently both the motion of the plasma enforced by the electric/magnetic fields and the fields which are produced by the plasma. In this section, we explain our simulation code in the order of (1) geometric feature of the system, (2) the 2D EM field model, (3) the 2D3V plasma dynamics model (4) collision processes of the charged particles and (5) the input parameters. Most parts of the model are the same as the previous model explained in Ref. [61] except for the collision processes of ions which are summarized in (4).

(1) Geometric feature of the system: The schematic drawing of the plasma chamber and the RF antenna is shown in Fig. 5.8. The radii of the plasma chamber r_c and the surrounding RF antenna r_{ant} are determined with reference to that of the CERN's Linac4 H$^-$ source. [26] Our model assumes the translational symmetry ($\partial/\partial z = 0$) in cylindrical coordinates so the plasma chamber and the RF coil are infinitely long in the z-direction. Therefore, the particle loss in the z-direction may be underestimated compared to the actual plasma.

(2) 2D EM field model: One of the notable features of our model is the EM field solver that enables the model to simulate both the E- and H-mode discharges. The EM solver mainly calculates Faraday's law and Ampére's law and takes into account the current density j_{RF} in the RF antenna and the plasma current density $j_{pl.}$,

$$\nabla \times \boldsymbol{E} = -\frac{\partial \boldsymbol{B}}{\partial t}, \tag{5.11}$$
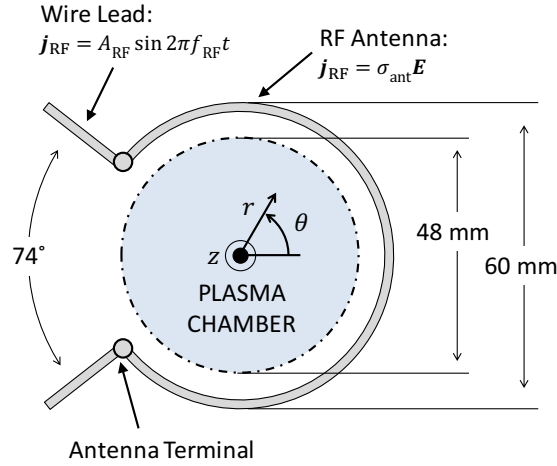
Fig. 5.8   The schematic drawing of the plasma chamber and the RF antenna [75].

$$\nabla \times \boldsymbol{B} = \mu_0 \boldsymbol{j} + \varepsilon_0 \mu_0 \frac{\partial \boldsymbol{E}}{\partial t}. \tag{5.12}$$

The input current I_{RF} is given on both sides of the wire lead shown in Fig. 5.8, which is defined as sinusoidal signal and expressed as

$$I_{\text{RF}} = I_0 \sin 2\pi f_{\text{RF}} t, \tag{5.13}$$

where I_0 and f_{RF} are the amplitude of the current and the frequency of the RF current, respectively. The current density in the antenna $\boldsymbol{j}_{\text{RF}}$ is calculated by Ohm's law so that the voltage drop between the antenna terminals and the resultant electric field can be taken into account self-consistently:

$$j_{\text{RF}} = \begin{cases} \sigma_{\text{ant}} E, & \text{on the antenna} \\ \pm A_{\text{RF}} \sin 2\pi f_{\text{RF}} t, & \text{on the wire leads} \end{cases} \tag{5.14}$$

where σ_{ant} is the conductivity of the RF antenna and A_{RF} is the coefficient corresponds to the amplitude of input current I_0. It can be assumed that σ_{ant} is constant in the RF range as long as the antenna is made of a typical metal ($\sigma \approx 10^7 \text{S/m}$) since the charge in the antenna relaxes within much shorter time than one RF cycle. The model of plasma current density $j_{\text{pl.}}$ in Eq. (5.12) is calculated from the plasma dynamics model, which will be explained later.

The Maxwell's equations, Eqs. (5.11) and (5.12), are integrated in time and space in accordance with the Finite Difference Time Domain (FDTD) method [47]. Since Eqs. (5.11) and (5.12) are solved in the cylindrical coordinates, the model employs a cylindrical version of the Yee cell to discretize the equations spatially. The simulation domain is 5 times larger

than the antenna radius so that the EM waves that are numerically reflected at the boundary of the domain diminishes before returning back to the antenna and plasma. The present model employs the Bayliss-Turkel radiation boundary condition for the radial boundary [51].

As Eqs. (5.11) and (5.12) do not include the Gauss's law for electricity, an additional correction process is required so as to calculate the electrostatic field properly [49]. The model corrects the calculated electric field $\tilde{E}$ to E_c which accurately satisfies Gauss's law. When the potential due to E_c differs from $\tilde{E}$ by $\delta\phi$,

$$E_c = \tilde{E} - \nabla\delta\phi, \tag{5.15}$$

As E_c is given by Gauss's law,

$$\nabla \cdot E_c = \frac{\rho}{\varepsilon_0}, \tag{5.16}$$

where ρ is the charge density. Combining Eqs. (5.15) and (5.16), we obtain the Poisson's equation for the potential difference $\delta\phi$,

$$\nabla^2\delta\phi = \nabla \cdot \tilde{E}_c - \frac{\rho}{\varepsilon_0}. \tag{5.17}$$

The Poisson's equation is also discretized in the same manner as Eqs. (5.11) and (5.12) and solved based on the Successive Over-Relaxation (SOR) method. Gauss's law for magnetism, on the other hand, can be readily satisfied without being solved directly. It is satisfied automatically as long as the divergence of magnetic field $\nabla \cdot B$ is initially set to be zero as it is independent of time. One can find the independence by taking the divergence of Faraday's law Eq. (5.11):

$$\nabla \cdot (\nabla \times E) = -\nabla \cdot \frac{\partial B}{\partial t} \tag{5.18}$$

$$\Rightarrow \frac{\partial}{\partial t}(\nabla \cdot B) = 0. \tag{5.19}$$

(3) 2D3V plasma dynamics model: Our model is able to calculate the motion of the charged particles in RF plasma by using the Boris-Buneman method [49]:

$$m_s\frac{dv_s}{dt} = q_s(E + v_s \times B) + (\text{collision}), \tag{5.20}$$

where s denotes the species of the charged particle. The charged particles that our simulation code tracks are electrons, hydrogen atomic ions and hydrogen molecular ions (e^-, H^+ and

H_2^+, respectively). Each of them is tracked until they reach the chamber wall or are lost by the destructive collision process. Although it is reported that H_3^+ exists in specific RF plasmas [73], we neglect its existence in this study. This is because the data of the collision processes of H_3^+ are not as abundant as for the other particle species.

The electric and magnetic fields which are required to integrate Eq. (5.20) in time are evaluated from the four grid points closest to the particle by first-order interpolation. The contribution of the parameters loaded on the four closest grids is computed by multiplying the weighting function $W(r, \theta)$, which is determined based on the volume-based interpolation. The weighting function W is corrected in accordance with the Verboncoeur volume method that is employed so as to lessen the error which arises due to the interpolation in the curvilinear coordinate [60].

The plasma current $j_{\mathrm{pl.}}$ of a grid point $W(r_i, \theta_j)$ is calculated from the sum of the velocity of the charged particles in the cell:

$$j_{\mathrm{pl.}}(r_i, \theta_j) = \sum_{\mathrm{s}} \sum_{k=1}^{N_{\mathrm{s}}} q_{\mathrm{s}} v_{\mathrm{s},k} W(r, \theta), \tag{5.21}$$

where N_{s} is the number of test particles. The contribution of a charged particle to the grid point is multiplied by the same weighting function W mentioned above.

(4) Collision processes of the charged particles: The change in the momentum of a particle due to the elastic/inelastic collisions is calculated at every 10 time steps that Eq. (5.21) is integrated. The frequency of the collision calculation is determined to be much smaller than the total collision frequency of the particle. The collision processes are modeled based on the Monte Carlo Null-Collision method [48]. Tables 4.3 and 4.2 show the collision processes that have newly been added to the present model. The electron-electron ($e^- $-$e^-$) Coulomb collision process, on the other hand, is not taken into account, which may play an important role for RF-ICP discharges [52]. Thus one has to note that the present model is not applicable to a specific plasma parameter range where the e^--e^- Coulomb collision occurs enough to affect the plasma parameter.

(5) Input parameters: The input parameters for the simulation shown in the following section are listed in Table 5.2. The time step and the size of the Yee cell are determined not to violate the Courant-Friedrichs-Lewy (CFL) condition. Also, the time step Δt is chosen to be small enough to resolve all the phenomena which are of interest. The collisions are evaluated every 10 time steps, which means $\Delta t_{\mathrm{coll}} = 10\Delta t = 5 \times 10^{-12}$ s. We have confirmed that the smaller choice of the collision time step does not change the simulation results.

In the initial state, the plasma is seeded uniformly through the chamber to satisfy the charge

neutrality in each cell:

$$n_{0e} = n_{0H^+} + n_{0H_2^+},$$ (5.22)

where n_{0e}, n_{0H^+} and $n_{0H_2^+}$ denote the initial density of electron, H^+ and H_2^+, respectively. The ratio of n_{0H^+} to $n_{0H_2^+}$ is 10 %. The determination of the ratio is discussed in Ref. [61].

The present model treats the neutral gas as a background. It is assumed that the pressure p_{H_2} and the temperature T_{H_2} of the H_2 gas are fixed with respect to time and space. This assumption is valid when the gas pressure is high because the discharge process that has been simulated is in the regime where the plasma density is negligibly smaller than the density of the background gas ($\approx 10^{21}/m^3$). Furthermore, the ignorance of the the the e^--e^- Coulomb collisions can be justified due to the high pressure condition because the collisions with neutral gas become the dominant ones.

On the other hand, the vibrational excitation/de-excitation processes of $H_2(v)$ and also the population change due to such processes are taken into account. It has been assumed that the all the molecules are initially in the ground state and the population change is treated as a volume averaged value. The density regime which we investigate in this study ($n_e \approx 10^{16}/m^3$ at most), however, is so low that the population change in $H_2(v \neq 0)$ is negligibly small. This model of the $H_2(v)$ population is mandatory for the simulation in the higher density regime ($n_e > 10^{17}/m^3$) because the vibrationally excited molecules play a key role in the H^- production.

The input values for the atom (T_H, n_H and n_H/n_{H_2}) listed in Table 5.2 are determined in reference to the experimental results. In Ref. [77], the molecular and atomic temperatures have been measured in the lower pressure regime ($p_{H_2} = 0.1$ - 1 Pa). It has been shown that the atomic temperature tends to be higher than the molecular temperature in the lower pressure regime, and those two temperatures approach each other as the pressure increases. Therefore, we have assumed that the atomic temperature is the same as the molecular temperature in the present discharge condition ($p_{H_2} = 15$ Pa).

The dissociation degree is about 2.5 % in the lower density regime and increases to 10 % in the H-mode [78]. We have confirmed that the simulation results do not significantly change in the dissociation range of 0 - 10 %.

5.2.4   Results

5.2.4.1 Temporal Behavior of Discharge Parameters

The power dissipated in the plasma P_{diss} ($\equiv \int j_{pl.} \cdot E dV$) has been calculated for the two cases with and without the ion-neutral collision processes, which has been shown in Fig. 5.9. One can see that the time trend of P_{diss} clearly changes where $t = 0.16\,\mu s \equiv t_{EH}$. This clear change
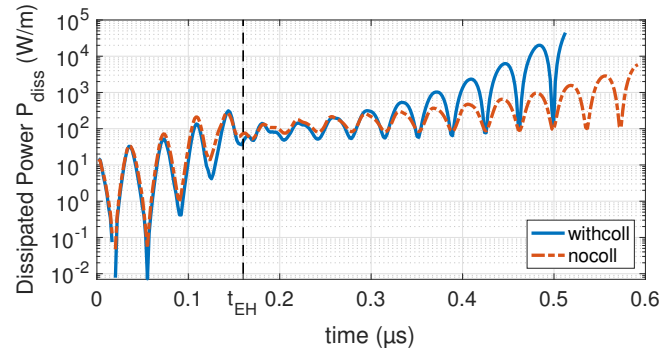
Fig. 5.9   The difference in the dissipated power due to the ion-neutral collision processes [75].

represents the discharge mode transition as was discussed in the previous paper [61]: the decrease in the amplitude of the oscillation of P_{diss} at $t = t_{\mathrm{EH}}$ is due to the replacement of the strong capacitive field with the weak inductive field. Note that the temporal features of P_{diss} are not significantly affected by the ion-neutral collision, especially before/around the mode transition. The change due to the ion-neutral collisions gradually becomes obvious as the

Table 5.2   List of Input Parameters.

Parameter	Symbol	Value
Frequency of input current	f_{RF}	13.56 MHz
Amplitude of input current	I_0	$6.9 \times 10^3 \mathrm{A/m}$
Radial width of the cell	Δr	2 mm
Azimuthal width of the cell	$\Delta \theta$	12°
Time step	Δt	5×10^{-13} s
Time step for collision evaluation	Δt_{coll}	5×10^{-12} s
Initial density of electron	$n_{0\mathrm{e}}$	$1 \times 10^{12} /\mathrm{m}^3$
Initial temperature of electron	$T_{0\mathrm{e}}$	300 K
Weight of the test particle	-	5×10^5
H_2 pressure	p_{H_2}	15 Pa
H_2 temperature	T_{H_2}	300 K
H temperature	T_{H}	300 K
H density	n_{H}	$0.1 n_{\mathrm{H}_2}$
Dissociation degree of H_2 gas	$n_{\mathrm{H}}/n_{\mathrm{H}_2}$	10 %
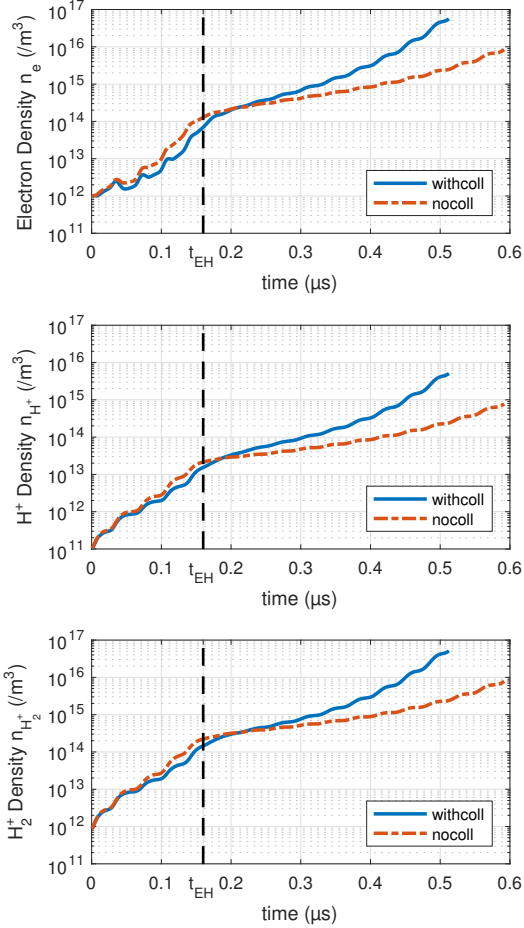
Fig. 5.10 The difference in the average density due to the ion-neutral collision processes [75].
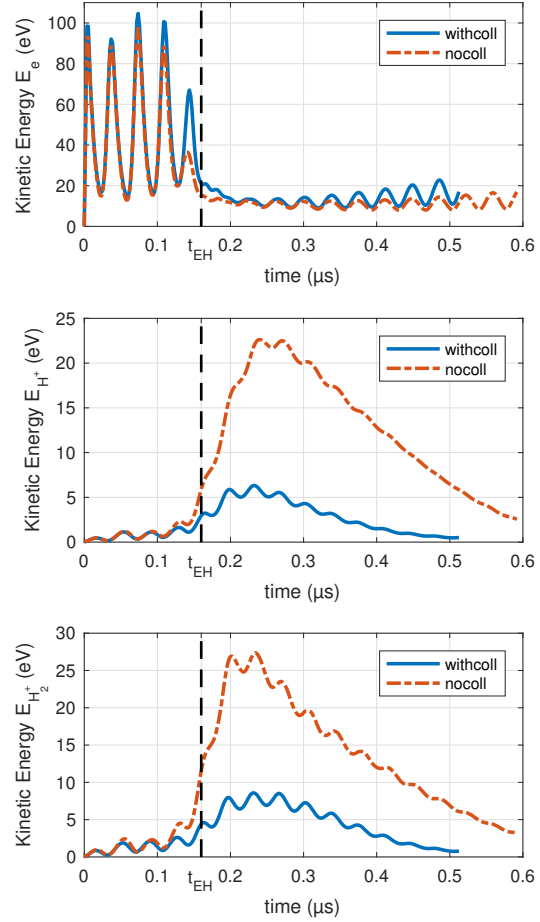
Fig. 5.11 The difference in the averaged kinetic energy due to the ion-neutral collision processes [75].

time goes by after the mode transition. This change makes the difference in other discharge parameters (the density and the kinetic energy of the plasma) and its cause will be explained by discussing the spatiotemporal profile of the plasma below. We hereby define the plasma is in the E-mode where $t < t_{\rm EH}$ and is in the H-mode where $t > t_{\rm EH}$.

The time evolution of the spatially averaged density $n_{\rm s}$ (s = e$^-$, H$^+$, H$_2^+$) for each particle species is shown in Fig. 5.10 with and without the ion-neutral collisions. The time evolution of the density is rather understandable as it reflects somewhat the time evolution of $P_{\rm diss}$ in Fig. 5.9. This is because a large portion of the power dissipated in the plasma is consumed for the ionization, which determines the growth rate of the plasma. As seen from Fig. 5.10, the increasing rate of the density decreases at $t = t_{\rm EH}$ as $P_{\rm diss}$ also decreases at the same time. The increasing rate of the density with ion-neutral collision is getting larger than that without

ion-neutral collision. This tendency of the density after the mode transition is reflected by the same tendency in P_{diss} shown in Fig. 5.9.

The time evolution of the kinetic energy E_{s} for each particle species averaged over the calculation domain is shown in Fig. 5.11. Large difference due to ion collision processes cannot be seen in the E-mode. In the H-mode, the difference in the kinetic energy appears differently depending on the particle species.

As for the kinetic energy of electron E_{e} (top figure in Fig. 5.11), the drastic drop of the kinetic energy at $t = t_{\mathrm{EH}}$ takes place. It is caused by the mode transition. This drastic drop is independent of the effect of the ion-neutral collision as expected. On the other hand, after the mode transition, the amplitude of the kinetic energy in the H-mode increases more rapidly when the ion-neutral collision is included. This is also explained by the time evolution of P_{diss} in Fig. 5.9.

The kinetic energy of the heavy particles $E_{\mathrm{H^+}}$ and $E_{\mathrm{H_2^+}}$ (shown in bottom and middle in Fig. 5.11, respectively) increases after the mode transition, which is due to the formation of the plasma sheath. Soon after the mode transition, the sheath thickness is comparable with the chamber radius. Thus most of the ions in the chamber are accelerated by the sheath without any brake when the ion-neutral collisions are ignored. This leads to the large increase in $E_{\mathrm{H^+}}$ and $E_{\mathrm{H_2^+}}$ as shown in Fig. 5.11. When the ion-neutral collision is taken into account, the peak values of $E_{\mathrm{H^+}}$ and $E_{\mathrm{H_2^+}}$ drastically decreases. This is because the collisions are frequent enough to weaken the sheath acceleration. The discussion on the spatiotemporal profile of the potential can be found in Ref. [61].

5.2.4.2 Spatiotemporal Behavior of the Plasma

The difference in the discharge parameters (P_{diss}, n_{s} and E_{s} where s = e$^-$, H$^+$, H$_2^+$) shown in Figs. 5.9 - 5.11 due to the ion collisions is significant when the plasma is in the H-mode. The cause of the difference can be explained by the spatial profile of the plasma. Figure 5.12 shows the time evolution of the spatial profile of the electron density.

Soon after the mode transition (the top figure in Fig. 5.12), the spatial profile of the electron density shows no significant difference due to the ion collisions. One can see that the electrons localize in the region where the ionization process frequently takes place in the E-mode. The localized profile gradually expands towards the wall as the plasma grows. The ion collisions affect the expansion speed as shown in the second - fourth figures in Fig. 5.12. The difference in the expansion speed with and without ion-neutral collision leads to the difference in the power couple to the plasma, i.e., P_{diss} shown in Fig. 5.9. We have specified the most dominant collision process that contributes to the difference; the charge transfer between H$_2$ and H$_2^+$ is about 75 % of the whole ion-neutral collision events.
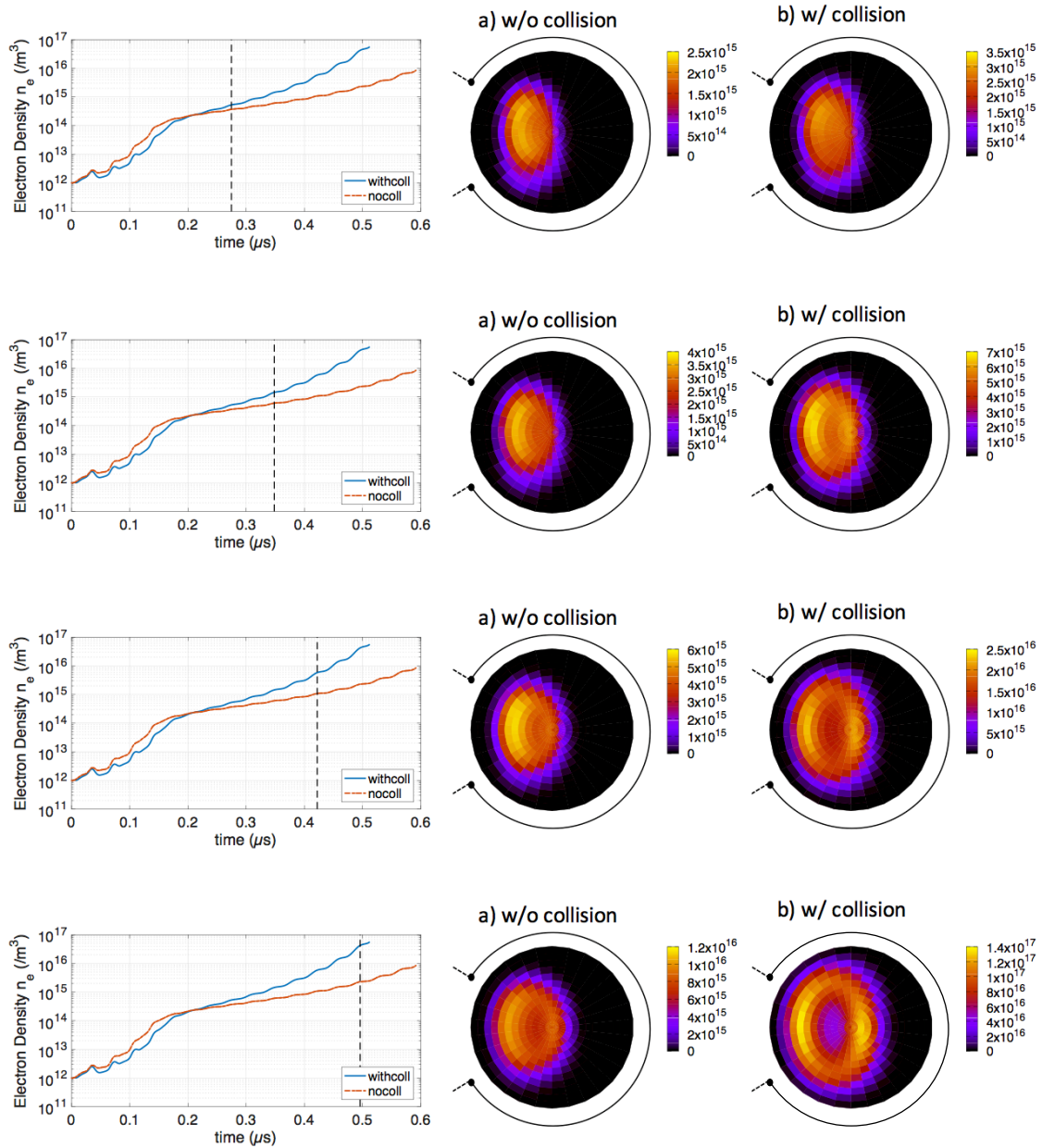
Fig. 5.12   The effect of the ion-neutral collision processes on the spatiotemporal behavior of the electron density. The left figure is the time evolution of the volume averaged electron density, and the sub-figures (a) and (b) are the spatial profile of the electron density without and with the ion-neutral collisions, respectively. The sub-figures (a) and (b) in each row relate to the time shown by a dashed line on the left that row [75].
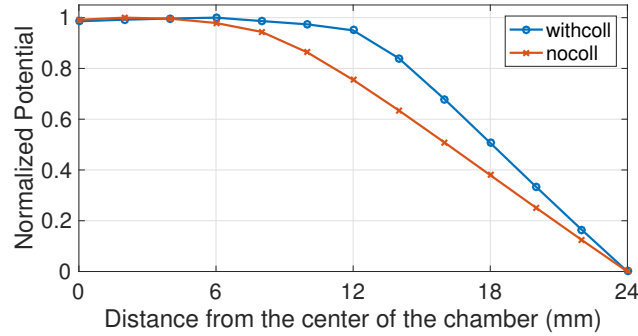
Fig. 5.13   The typical potential profiles in the H-mode from the center to the wall. The potentials are normalized by the peak values of each case [75].

The plasma sheath is one of the factors that determines the spatial distribution that we have discussed: For example, the sheath thickness affects the area where the bulk plasma can distribute. Therefore, the difference in the collisional and collision-less sheath is also important in order to investigate the ion-neutral collision effect on the discharge parameters.

The spatiotemporal behavior of the electrostatic potential has shown in Figs 5.13 and 5.14. Figure 5.13 shows the radial distribution of the potential difference from the center to the chamber wall at $\theta = \pi$. The profile is a typical one in the H-mode and normalized by the peak value of each case. Figure 5.13 shows the time evolution of the potential difference from the center to the wall of the chamber.

From Fig. 5.13, it has been shown that the sheath becomes narrow when the ion-neutral collision taken into account. The area where the bulk plasma distributes becomes larger due to the narrower sheath. The broader distribution leads to the better coupling with the inductive field and the larger power dissipation (P_{diss} shown in Fig. 5.9). Most of the power is dissipated by the electron so that the increase in P_{diss} enhances the ionization by the electron. As a result, the increase in the plasma density becomes more rapid as shown in Fig. 5.10.

The decrease in the sheath thickness (the narrowing effect) due to the ion-neutral collision can be verified by a theoretical approach. We roughly estimate the thickness of the collisional sheath by a simple 1D analysis as follows (the detailed discussion can be found in Ref. [79] and the brief summary is in Ref. [4]).

In the collisional sheath, the ion velocity can be given by $u_s = qE/m_i\nu$ (ν denotes the ion-neutral collision frequency) so that the ion current density J_0 is given by

$$J_0 = \frac{q^2 n_i}{m_i \nu} E. \tag{5.23}$$
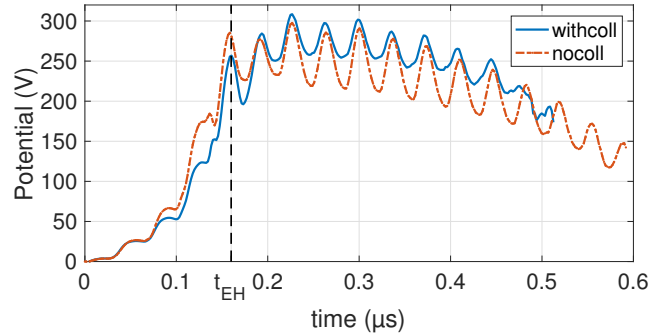
Fig. 5.14   Time evolution of the potential difference from wall to the center [75].

Assuming the electron-free ion sheath, one can obtain the Poisson's equation,

$$\frac{dE}{dx} = \frac{J_0 m_i v}{\varepsilon_0 q E}. \tag{5.24}$$

On the boundary condition of $E(0) = \phi(0) = 0$, Eq. (5.24) becomes,

$$\frac{d\phi}{dx} = \sqrt{\frac{2J_0 m_i v}{\varepsilon_0 q}x} \Rightarrow \phi = \frac{2}{3}\sqrt{\frac{2J_0 m_i v}{\varepsilon_0 q}}x^{\frac{3}{2}}. \tag{5.25}$$

In the case that the potential is V_0 at the sheath edge of $x = s$, i.e., $\phi(s) = V_0$, the sheath thickness s is given as

$$s = \left(\frac{9\varepsilon_0 q V_0{}^2}{8J_0 m_i v}\right)^{\frac{1}{3}}. \tag{5.26}$$

The collisions slow down the ion so that their residence time in the sheath region increases. Hence, the contribution of the ions to the space charge increases, which consequently narrows the sheath. The brief discussion above, which has led to Eq. (5.26), shows the narrowing effect of the collision. The narrowing effect also explains the decrease in the peak values of E_{H^+} and $E_{H_2^+}$ we have discussed above: the fraction of ions which are accelerated in the sheath decreases due to the decrease of the sheath thickness.

As for the difference due to the ion-neutral collision shown in Fig. 5.14, one can see that the amplitude of the oscillation becomes smaller due to ion-neutral collisions. This tendency is reasonable, which we assume is caused by the better confinement of ions. The ion-neutral collisions prevent from ion current to flow towards the wall and decrease the increase the wall potential. Therefore, the ion-neutral collision lessens the response of the potential to the RF field.

Fig. 5.15   The example EEPF and its exponential fittings. The EEPF is calculated from the EEDF normalized by the electron density n_e [75].

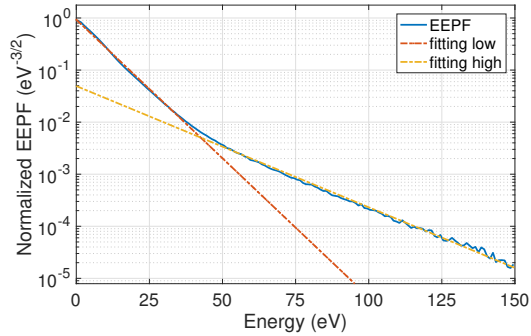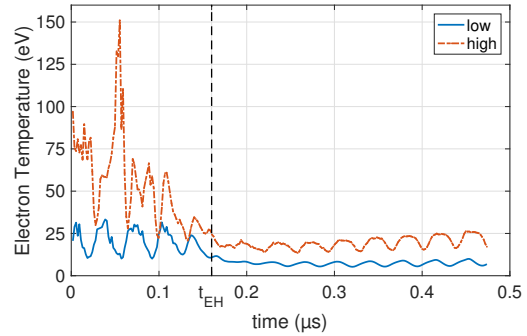Fig. 5.16   The time evolution of the estimated temperatures. High and low temperatures are shown in solid and broken line, respectively [75].

5.2.4.3 Kinetic Behavior During the Mode Transition

It is also necessary to discuss the effect of the ion-neutral collision processes on the kinetic features of the plasma. Note that the energy distribution functions, which are presented below, are calculated in the central region where $r < 0.5r_c$ and $\pi/2 < \theta < 3\pi/2$ so as to exclude the sheath region.

As for the EEDF, we already discussed it in the previous paper and the same can be concluded from the present result as well: it shows the bi-Maxwellian distribution and the deviation in the high energy component is larger in the E-mode than in the H-mode. We have conducted a further investigation on the time evolution of two electron temperatures of bi-Maxwellian EEDF. Two temperatures have been estimated from the electron energy probability function (EEPF) $f_e(\varepsilon)$ ($\equiv F_e / \sqrt{\varepsilon}$) under the assumption that $f_e(\varepsilon < 40\text{eV})$ and $f_e(\varepsilon > 50\text{eV})$ follow different Maxwellian distributions whose temperatures are $T_{e,\text{low}}$ and $T_{e,\text{high}}$, respectively. The two exponential fitting curves and the EEPF are shown in Fig. 5.15 for the typical case for example. Although two temperatures have been estimated also for both cases with and without the ion-neutral collision, one case is presented because we cannot see a significant quantitative difference as is expected, except for the early stage of the discharge where the temperature estimation is subject to statistical noise due to the small number of test particles.

The time evolution of the two estimated temperatures is shown in Fig. 5.16. One can see that both temporal behaviors of $T_{e,\text{low}}$ and $T_{e,\text{high}}$ qualitatively agree with each other and those are similar to that of the spatially averaged kinetic energy of electron shown in Fig. 5.11. The temperature $T_{e,\text{high}}$ is 2 - 3 times larger than $T_{e,\text{low}}$ except for the second peak in the E-mode. The oscillation of the two temperatures drastically drops due to the mode transition
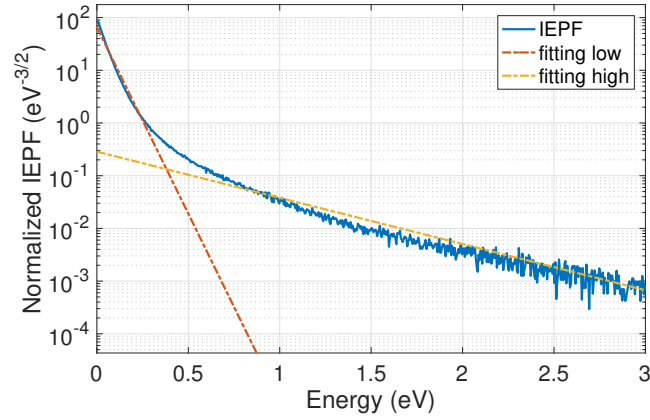
Fig. 5.17   The example IEPF $f_{H_2^+}$ and its exponential fittings. The IEPF is calculated from the IEDF normalized by the ion density $n_{H_2^+}$ [75].
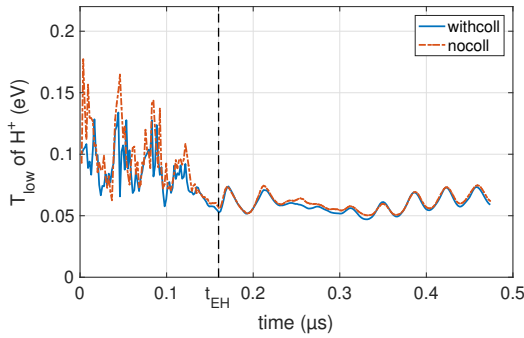
Fig. 5.18   The time evolution of T_{low} of the low temperature component of H^+, which has been calculated with and without ion-neutral collisions [75].
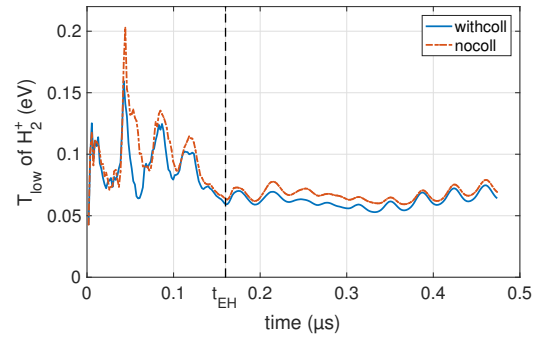
Fig. 5.19   The time evolution of T_{low} of the low temperature component of H_2^+, which has been calculated with and without ion-neutral collisions [75].

and gradually increases as the plasma grows. In the H-mode, $T_{e,low}$ remains below 10 eV and its oscillation is small while $T_{e,high}$ is oscillating around 20 eV with the amplitude of 5 - 10 eV. The threshold energy for the non-dissociative ionization of hydrogen molecules with electrons is more than 10 eV, which is the most dominant ionization process in this discharge condition. It can be suggested that the high energy component may play an important role in the growth of the plasma, and the kinetic perspective is therefore mandatory to describe the RF ICP discharge.

We have also investigated the ion energy probability functions (IEPF) f_{H^+} and $f_{H_2^+}$ to see the kinetic behavior of the ions, which we have not seen in detail in the previous work. The results indicate that both f_{H^+} and $f_{H_2^+}$ show bi-Maxwellian as the EEPF does. The shapes of f_{H^+} and $f_{H_2^+}$ are almost the same as each other and the typical IEPF $f_{H_2^+}$ is shown in Fig. 5.17. As we have estimated $T_{e,low}$ and $T_{e,high}$ above, the temperatures of the low and high energy

Fig. 5.20 The time evolution of T_{high} of the low temperature component of H^+, which has been calculated with and without ion-neutral collisions [75].
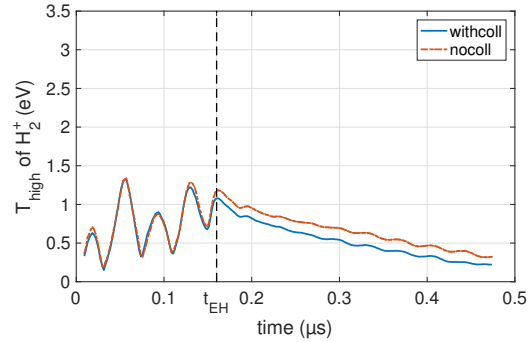
Fig. 5.21 The time evolution of T_{high} of the low temperature component of H_2^+, which has been calculated with and without ion-neutral collisions [75].

components of ions are estimated from the IEPF where $\varepsilon < 0.2$ eV and $\varepsilon > 1$ eV, respectively.

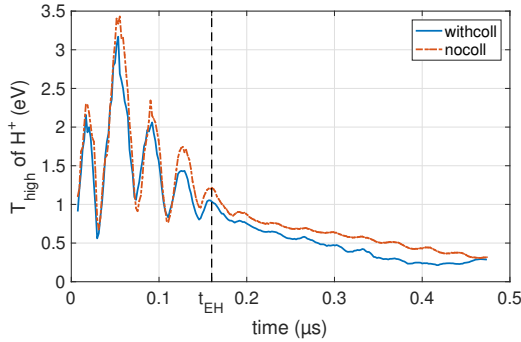As for T_{low} of H^+ and H_2^+ shown in Figs. 5.18 and 5.19, the temporal behavior is different from that of the spatially averaged kinetic energy E_{H^+} and $E_{H_2^+}$ shown in Fig. 5.11. As we mentioned above, the increase in E_{H^+} and $E_{H_2^+}$ after the mode transition represents increase in the convective energy of ion due to the acceleration by the sheath potential. The same increase cannot be seen in T_{low} of H^+ and H_2^+. This difference is because of the region where the IEPF is calculated. As it excludes the sheath region, the IEPF does not include the convective component and then T_{low} of H^+ and H_2^+ represents only the thermal energy of the ions.

In the E-mode, T_{low} of H_2^+ seems to respond the RF field as it oscillating in almost the same frequency as the RF field while it is hard to see the similar trend in T_{low} of H_2^+ due to the large statistical noise. In the H-mode, both T_{low} of H^+ and H_2^+ are in the range of 0.05 - 0.08 eV, which is almost the same order as the background gas temperature. This is because that the low energy component of the IEPF is dominated by the newly-birthed ions from the background gas molecules: the most frequent ionization process that yields H^+ and H_2^+ is the dissociative and non-dissociative ionization processes between electron and neutral, respectively. This also explains the reason why no significant difference can be seen due to the ion-neutral collision processes.

The temperatures T_{high} of H^+ and H_2^+ are estimated from the high energy component of the IEPF, which are shown in Figs. 5.20 and 5.21. The temporal behaviors of T_{high} of H^+ and H_2^+ are qualitatively the same with each other. Both temperatures show the RF oscillation in the E-mode and the amplitude of T_{high} of H^+ is larger than the other one. This may be simply because of the difference in the mass. As the mass of H^+ is smaller, H^+ responds more easily to the RF fields than the other and so does T_{high} of H^+. In the H-mode, the amplitude of the oscillation drastically decreases because the inductive field is weaker than the capacitive

one and not strong enough to make T_{high} of H^+ and H_2^+ respond. Both temperatures T_{high} of H^+ and H_2^+ approach to the range of the background gas temperature as T_{low} does. The temporal behavior of T_{high} seems not to be affected by the ion-neutral collision. The ion-neutral collision affects to reduce T_{high} of H^+ and H_2^+ by 0.15 - 0.2 eV and the slight increase in T_{high} of H^+ can be seen where $t > 0.4\mu\text{s}$. We assume the increase is because of the larger increase in P_{diss} due to the effect of the ion-neutral collisions. Since the respond of H_2^+ to the RF field is slower than H^+, it can be expected that the same increase in T_{high} of H_2^+ will occur in the later period where we have not simulated in this study. On the other hand, no significant effect can be seen in the E-mode.

From the results of T_{low} and T_{high} of H^+ and H_2^+, it has been shown that the temporal behaviors of T_{low} and T_{high} differ from each other especially in the E-mode and during the mode transition. On the other hand, both T_{low} and T_{high} approach to the background gas temperature so that the bi-Maxwellian assumption may no longer be necessary to apply. Therefore, it can be suggested that the kinetic perspective is of importance, under the present discharge condition at least, to describe the dynamics of the ion in the E-mode plasma and during the mode transition while it is not so important in the H-mode at the relatively high gas pressure condition.

5.2.5   Conclusion

The effect of the ion-neutral collision on the RF ICP discharge has been numerically investigated. The conclusion of our previous paper, which we have confirmed without taking the ion-neutral collision into account, has been verified by the comparison between the two simulation results with and without the ion-neutral collision.

The time trends of the volume-averaged discharge parameters, i.e., the power deposition, the density and the kinetic energy of the plasma, are not significantly affected by the ion collision: the sudden changes at the specific timing due to the discharge mode transition have been observed in the both cases with and without the ion collision. The simulation results have also indicated that the EEDF during the E-mode discharge can be characterized by the large deviation from the Maxwellian while the deviation becomes smaller in the H-mode. This feature of the EEDF is also the same as what we have observed without taking the ion-neutral collision into account as expected. As far as the basic characteristics of the E-to-H mode transition are concerned, there is no significant change due to the ion-neutral collision.

However, the comparison between the two cases with and without the ion-neutral collision has provided the further insight into the RF discharge that had not been obtained in the previous work. The effect of the ion-neutral collision on the RF ICP discharge can be summarized as follows:

1. No significant difference in the E-mode discharge can be seen, while the H-mode plasma is clearly affected by ion-neutral collision processes. This is because the behavior of the E-mode plasma is characterized mainly by that of the electron. On the other hand, the dynamics of the ion plays a key role in the H-mode as the plasma starts to show the collective behavior due to the manifestation of the quasi-neutrality.

2. The H-mode plasma is spread out through the chamber in a shorter time. This effect is important to discuss the RF discharge because the area that the plasma distributes determines the amount of the inductive power coupled to the plasma. This is the reason that the growth rate of the plasma density becomes larger when the ion-neutral collision is included.

3. We have investigated the kinetic features of the RF ICP. It has been confirmed that the energy distribution functions of electrons and ions are bi-Maxwellian regardless of the presence of the ion-neutral collision. This feature is obvious especially in the E-mode and during the mode transition. Therefore, it has been suggested that the kinetic treatment is mandatory to model the discharge mode transition of the RF ICPs at least under the present discharge condition.

4. As is expected, no significant effect of the ion-neutral collision on both the low/high temperature components of the EEDF can be seen. On the other hand, the ion-neutral collision reduces the high energy component of the IEDF. As for the low energy component of the IEDF, it is not so affected by the ion-neutral collision and has almost the same temperature as the birth energy of ionization. These features are valid in the present discharge condition. In the higher density regime, it can be expected that the ion-neutral collision may affect the IEDF. Further investigation is mandatory to discuss the expectation of the higher density regime, which is more difficult to simulate due to the massive calculation cost.

The present study has been carried out under the assumption that the degree of the ionization is small enough for neutrals to be treated as a stable background. However, the ion sources for the fusion or the accelerator are usually operated in the low gas pressure regime where our assumption is no longer valid. The model of the neutral background will be improved in the future work in order to make our model applicable to more practical discharge condition.

Chapter 6

Conclusion

We have presented our numerical studies on the hydrogen ion sources with the RF-ICP. The studies have been carried out to develop insight into the operation of the RF-ICP. Specifically, we have studied the RF-ICP by two models, (1) the theoretical equivalent circuit model and (2) the particle-based model of the hydrogen RF-ICP discharge.

In Chapter 1, we have described the physical property of the RF-ICP and its application. The scope of this thesis has also been defined in this chapter.

The theoretical model of the equivalent circuit of the RF-ICP has been explained in Chapter 2. This model is applied to the RF system of the CERN's Linac4 H$^-$ source. The comparison between the model and the measurement has indicated that the model is useful to predict qualitatively the behavior of the plasma impedance, especially for the plasma resistance. Using this model, we have confirmed the utility of the frequency tuning, which has been performed in the RF system in order to compensate the impedance change due to the plasma formation. Although the present model is not quantitative enough to predict the plasma impedance and to optimize the RF system control, the model is still useful to direct the system design.

Aiming to develop more detailed model for the plasma impedance calculation, we have developed the particle-based model which is able to analyze its discharge process from a kinetic point of view. The detailed description of the model has been presented in Chapter 4. The model, RF-code, is composed of the electromagnetic field model and the plasma dynamics model. By coupling these two model, the behavior of the plasma and the electromagnetic field can be simulated self-consistently. Furthermore, the model takes the capacitive (electrostatic) field into account, which is due to the high RF potential applied to the RF antenna. This enables us to simulate the discharge mode transition between E- and H-mode.

In Chapter 5, the discharge process of hydrogen RF-ICP is numerically analyzed by using the model introduced in Chapter 4. It has been confirmed that the model is able to reproduce the E-to-H discharge mode transition. In addition, Energy Distribution Functions (EDFs) of electron and ions is analyzed from a kinetic view of point. The EDFs deviate from the

Maxwell distribution in the thermal equilibrium. This indicates the importance of the kinetic perspective to investigate the RF-ICP discharge.

In the future work, it is expected that this model enables us to calculate the impedance of RF-ICP with the non-equilibrium EDFs. This model will be the basis for the further study of the impedance matching between RF system and RF-ICP, which takes the kinetic effect into account.

Bibliography

[1] J Hopwood. Review of inductively coupled plasmas for plasma processing. *Plasma Sources Science and Technology*, 1(2):109, 1992.

[2] K.A. MacKinnon M.Sc. Lxvi. on the origin of the electrodeless discharge. *The London, Edinburgh, and Dublin Philosophical Magazine and Journal of Science*, 8(52):605–616, 1929.

[3] Michael A. Lieberman and Allan J. Lichtenberg. *Inductive Discharges*, pages 461–489. John Wiley & Sons, Inc., 2005.

[4] Pascal Chabert and Nicholas Braithwaite. *Physics of Radio-Frequency Plasmas*. Cambridge University Press, 2011.

[5] N. Contaxes and Albert J. Hatch. High‐frequency fields in solenoidal coils. *Journal of Applied Physics*, 40(9):3548–3550, 1969.

[6] Gerald S. Harmon. The high‐frequency electric and magnetic fields of a solenoid. *Journal of Applied Physics*, 69(11):7400–7405, 1991.

[7] Katja Henjes. Electric and magnetic fields in solenoidal coils from statics to mhz frequencies. *Journal of Applied Physics*, 79(1):21–29, 1996.

[8] J. Amorim, H. S. Maciel, and J. P. Sudano. High‐density plasma mode of an inductively coupled radio frequency discharge. *Journal of Vacuum Science & Technology B: Microelectronics and Nanometer Structures Processing, Measurement, and Phenomena*, 9(2):362–365, 1991.

[9] E Kawamura, D B Graves, and M A Lieberman. Fast 2d hybrid fluid-analytical simulation of inductive/capacitive discharges. *Plasma Sources Science and Technology*, 20(3):035009, 2011.

[10] E Kawamura, M A Lieberman, A J Lichtenberg, and D B Graves. Two-dimensional simulation of inductive–capacitive transition instability in an electronegative plasma. *Plasma Sources Science and Technology*, 21(4):045014, 2012.

[11] U Kortshagen, N D Gibson, and J E Lawler. On the e - h mode transition in rf inductive discharges. *Journal of Physics D: Applied Physics*, 29(5):1224, 1996.

[12] Min-Hyong Lee and Chin-Wook Chung. On the e to h and h to e transition mechanisms in inductively coupled plasma. *Physics of Plasmas*, 13(6):063510, 2006.

[13] Hyo-Chang Lee, Dong-Hwan Kim, and Chin-Wook Chung. Discharge mode transition and hysteresis in inductively coupled plasma. *Applied Physics Letters*, 102(23):234104, 2013.

[14] S Mattei, K Nishida, S Mochizuki, A Grudiev, J Lettry, M Q Tran, and A Hatayama. Kinetic simulations and photometry measurements of the e-h transition in cylindrical inductively coupled plasmas. *Plasma Sources Science and Technology*, 25(6):065001, 2016.

[15] Y Miyoshi, Zoran Lj Petrovic, and Toshiaki Makabe. Optical computerized tomography of the e-h transition in inductively coupled plasmas in ar and ar-cf 4 mixtures. *Journal of Physics D: Applied Physics*, 35(5):454, 2002.

[16] S. V. Singh, P. Kempkes, and H. Soltwisch. Electron energy distribution function close to the mode transition region in an inductively coupled gaseous electronics conference reference cell. *Applied Physics Letters*, 89(16):161501, 2006.

[17] M M Turner and M A Lieberman. Hysteresis and the e-to-h transition in radiofrequency inductive discharges. *Plasma Sources Science and Technology*, 8(2):313, 1999.

[18] M Abdel-Rahman, V Schulz von der Gathen, and T Gans. Transition phenomena in a radio-frequency inductively coupled plasma. *Journal of Physics D: Applied Physics*, 40(6):1678, 2007.

[19] T Czerwiec and D B Graves. Mode transitions in low pressure rare gas cylindrical icp discharge studied by optical emission spectroscopy. *Journal of Physics D: Applied Physics*, 37(20):2827, 2004.

[20] E. F. Jaeger, L. A. Berry, J. S. Tolliver, and D. B. Batchelor. Power deposition in high - density inductively coupled plasma tools for semiconductor processing. *Physics of Plasmas*, 2(6):2597–2604, 1995.

[21] Michael D Logue, Hyungjoo Shin, Weiye Zhu, Lin Xu, Vincent M Donnelly, Demetre J Economou, and Mark J Kushner. Ion energy distributions in inductively coupled plasmas having a biased boundary electrode. *Plasma Sources Science and Technology*, 21(6):065009, 2012.

[22] Fabienne Marcastel. CERN's Accelerator Complex. La chaîne des accélérateurs du CERN, Oct 2013. General Photo.

[23] L Arnaudon, P Baudrenghien, M Baylac, G Bellodi, Y Body, J Borburgh, P Bourquin, J Broere, O Brunner, L Bruno, C Carli, Friedhelm Caspers, S M Cousineau, Y Cuvet, C De Almeida Martins, T Dobers, T Fowler, R Garoby, F Gerigk, B Goddard, K Hanke, M Hori, M Jones, K Kahle, Willi Kalbreier, T Kroyer, D Küchler, A M Lombardi, L A López-Hernandez, M Magistris, M Martini, S Maury, E Page, M Paoluzzi, M Pasini, U Raich, C Rossi, J P Royer, E Sargsyan, J Serrano, R Scrivens, M Silari, M Timmins, W Venturini-Delsolaro, M Vretenar, R Wegner, W Weterings, and T Zickler.

Linac4 technical design report. Technical Report CERN-AB-2006-084. CARE-Note-2006-022-HIPPI, CERN, Geneva, Dec 2006. revised version submitted on 2006-12-14 09:00:40.

[24] J. Lettry, D. Aguglia, P. Andersson, S. Bertolo, A. Butterworth, Y. Coutron, A. Dallocchio, E. Chaudet, J. Gil-Flores, R. Guida, J. Hansen, A. Hatayama, I. Koszar, E. Mahner, C. Mastrostefano, S. Mathot, S. Mattei, Ø. Midttun, P. Moyret, D. Nisbet, K. Nishida, M. O'Neil, M. Ohta, M. Paoluzzi, C. Pasquino, H. Pereira, J. Rochez, J. Sanchez Alvarez, J. Sanchez Arias, R. Scrivens, T. Shibata, D. Steyaert, N. Thaus, and T. Yamamoto. Status and operation of the linac4 ion source prototypes. *Review of Scientific Instruments*, 85(2):02B122, 2014.

[25] J. Lettry, D. Aguglia, J. Alessi, P. Andersson, S. Bertolo, A. Butterworth, Y. Coutron, A. Dallocchio, N. David, E. Chaudet, D. Fink, J. Gil-Flores, M. Garlasche, A. Grudiev, R. Guida, J. Hansen, M. Haase, A. Hatayama, A. Jones, I. Koszar, T. Lehn, C. Machado, C. Mastrostefano, S. Mathot, S. Mattei, Ø. Midttun, P. Moyret, D. Nisbet, K. Nishida, M. O'Neil, M. Paoluzzi, J. Sanchez Alvarez, R. Scrivens, T. Shibata, D. Steyaert, N. Thaus, and A. Zelenski. Cern's linac4 h − sources: Status and operational results. *AIP Conference Proceedings*, 1655(1):030005, 2015.

[26] J. Lettry, D. Aguglia, J. Alessi, P. Andersson, S. Bertolo, S. Briefi, A. Butterworth, Y. Coutron, A. Dallocchio, N. David, E. Chaudet, D. Faircloth, U. Fantz, D. A. Fink, M. Garlasche, A. Grudiev, R. Guida, J. Hansen, M. Haase, A. Hatayama, A. Jones, I. Koszar, J.-B. Lallement, A. M. Lombardi, C. Machado, C. Mastrostefano, S. Mathot, S. Mattei, P. Moyret, D. Nisbet, K. Nishida, M. O'Neil, M. Paoluzzi, R. Scrivens, T. Shibata, D. Steyaert, N. Thaus, and G. Voulgarakis. Linac4 h − ion sources. *Review of Scientific Instruments*, 87(2):02B139, 2016.

[27] J. Lettry, D. Aguglia, S. Bertolo, S. Briefi, A. Butterworth, Y. Coutron, A. Dallocchio, N. David, E. Chaudet, U. Fantz, D. Fink, M. Garlasche, A. Grudiev, R. Guida, J. Hansen, M. Haase, A. Hatayama, A. Jones, T. Kalvas, I. Koszar, J.-B. Lallement, A. Lombardi, F. di Lorenzo, C. Machado, C. Mastrostefano, S. Mathot, S. Mattei, P. Moyret, K. Nishida, M. O'Neil, M. Paoluzzi, U. Raich, F. Roncarolo, R. Scrivens, D. Steyaert, N. Thaus, and G. Voulgarakis. Cern's linac4 cesiated surface h − source. *AIP Conference Proceedings*, 1869(1):030002, 2017.

[28] R. F. Welton, M. P. Stockli, Y. Kang, M. Janney, R. Keller, R. W. Thomae, T. Schenkel, and S. Shukla. Ion source antenna development for the spallation neutron source. *Review of Scientific Instruments*, 73(2):1008–1012, 2002.

[29] M. M. Paoluzzi, M. Haase, J. Marques Balula, and D. Nisbet. Cern linac4 h − source and spl plasma generator rf systems, rf power coupling and impedance measurements. *AIP Conference Proceedings*, 1390(1):265–271, 2011.

[30] H.U. Eckert and AEROSPACE CORP EL SEGUNDO CALIF LAB OPERATIONS. *The Induction Arc, a State-of-the Art Review*. Defense Technical Information Center, 1972.

[31] R. S. Hemsworth, A. Tanga, and V. Antoni. Status of the iter neutral beam injection system (invited). *Review of Scientific Instruments*, 79(2):02C109, 2008.

[32] R. Hemsworth, H. Decamps, J. Graceffa, B. Schunke, M. Tanaka, M. Dremel, A. Tanga, H.P.L. De Esch, F. Geli, J. Milnes, T. Inoue, D. Marcuzzi, P. Sonato, and P. Zaccaria. Status of the iter heating neutral beam system. *Nuclear Fusion*, 49(4):045006, 2009.

[33] U. Fantz, P. Franzen, W. Kraus, H. D. Falter, M. Berger, S. Christ-Koch, M. Fröschle, R. Gutser, B. Heinemann, C. Martens, P. McNeely, R. Riedl, E. Speth, and D. Wünderlich. Low pressure and high power rf sources for negative hydrogen ions for fusion applications (iter neutral beam injection) (invited). *Review of Scientific Instruments*, 79(2):02A511, 2008.

[34] U. Fantz, P. Franzen, W. Kraus, M. Berger, S. Christ-Koch, H. Falter, M. Fröschle, R. Gutser, B. Heinemann, C. Martens, P. McNeely, R. Riedl, E. Speth, A. Stäbler, and D. Wünderlich. Physical performance analysis and progress of the development of the negative ion rf source for the iter nbi system. *Nuclear Fusion*, 49(12):125007, 2009.

[35] U. Fantz, C. Hopf, D. Wünderlich, R. Friedl, M. Fröschle, B. Heinemann, W. Kraus, U. Kurutz, R. Riedl, R. Nocentini, and L. Schiesko. Towards powerful negative ion beams at the test facility elise for the iter and demo nbi systems. *Nuclear Fusion*, 57(11):116007, 2017.

[36] ITER – the way new energy. `https://www.iter.org`. Accessed: 2018-01-11.

[37] K. Nishida, S. Mochizuki, M. Ohta, M. Yasumoto, J. Lettry, S. Mattei, and A. Hatayama. Equivalent circuit of radio frequency-plasma with the transformer model. *Review of Scientific Instruments*, 85(2):02B117, 2014.

[38] A. Grudiev, J. Lettry, S. Mattei, M. Paoluzzi, and R. Scrivens. Numerical simulation of electromagnetic fields and impedance of cern linac4 h − source taking into account the effect of the plasma. *Review of Scientific Instruments*, 85(2):02B134, 2014.

[39] K. Nishida, S. Mattei, S. Briefi, A. Butterworth, A. Grudiev, M. Haase, A. Jones, M. M. Paoluzzi, G. Voulgarakis, A. Hatayama, and J. Lettry. Experimental investigation of plasma impedance in linac4 h − source. *AIP Conference Proceedings*, 1869(1):030038, 2017.

[40] G. Voulgarakis, J. Lettry, S. Mattei, B. Lefort, and V. J. Correia Costa. Autopilot regulation for the linac4 h − ion source. *AIP Conference Proceedings*, 1869(1):030012, 2017.

[41] A. Butterworth, A. Grudiev, J. Lettry, K. Nishida, M. Paoluzzi, and C. Schmitzer. Rf low-level control for the linac4 h − source. *AIP Conference Proceedings*,

1655(1):030007, 2015.

[42] Matthias Kronberger, Elodie Chaudet, Gilles Favre, Jacques Lettry, Detlef Küchler, Pierre Moyret, Mauro Paoluzzi, Laurent Prever ‐ Loiri, Claus Schmitzer, Richard Scrivens, and Didier Steyaert. Magnetic cusp configuration of the spl plasma generator. *AIP Conference Proceedings*, 1390(1):255–264, 2011.

[43] D. Wünderlich, S. Dietrich, and U. Fantz. Application of a collisional radiative model to atomic hydrogen for diagnostic purposes. *Journal of Quantitative Spectroscopy and Radiative Transfer*, 110(1):62 – 71, 2009.

[44] S. Briefi, S. Mattei, J. Lettry, and U. Fantz. Influence of the cusp field on the plasma parameters of the linac4 h − ion source. *AIP Conference Proceedings*, 1869(1):030016, 2017.

[45] E. Mahner, P. Chiggiato, J. Lettry, S. Mattei, M. O'Neil, H. Neupert, C. Pasquino, and C. Schmitzer. Gas injection and fast pressure-rise measurements for the linac4 h − source. *AIP Conference Proceedings*, 1515(1):425–432, 2013.

[46] S. Briefi, D. Fink, S. Mattei, J. Lettry, and U. Fantz. Determination of discharge parameters via oes at the linac4 h − ion source. *Review of Scientific Instruments*, 87(2):02B104, 2016.

[47] Kane Yee. Numerical solution of initial boundary value problems involving maxwell's equations in isotropic media. *IEEE Transactions on Antennas and Propagation*, 14(3):302–307, May 1966.

[48] K. Nanbu. Probability theory of electron-molecule, ion-molecule, molecule-molecule, and coulomb collisions for particle modeling of materials processing plasmas and cases. *IEEE Transactions on Plasma Science*, 28(3):971–990, Jun 2000.

[49] C.K. Birdsall and A.B. Langdon. *Plasma Physics via Computer Simulation*. Series in Plasma Physics and Fluid Dynamics. Taylor & Francis, 2004.

[50] R. Courant, K. Friedrichs, and H. Lewy. Über die partiellen Differenzengleichungen der mathematischen Physik. *Mathematische Annalen*, 100:32–74, 1928.

[51] Alvin Bayliss and Eli Turkel. Radiation boundary conditions for wave-like equations. *Communications on Pure and Applied Mathematics*, 33(6):707–725, 1980.

[52] S. Mochizuki, S. Mattei, T. Shibata, K. Nishida, A. Hatayama, and J. Lettry. Initial results of a full kinetic simulation of rf h − source including coulomb collision process. *AIP Conference Proceedings*, 1655(1):020016, 2015.

[53] Shintaro MOCHIZUKI, Stefano MATTEI, Kenjiro NISHIDA, Akiyoshi HATAYAMA, and Jacques LETTRY. Numerical analysis of electron energy distribution function and its effects on the H⁻ production in linac4 H⁻ source. *Plasma and Fusion Research*, 11:2406044–2406044, 2016.

[54] S. J. Buckman and M. T. Elford. Momentum transfer cross sections: Datasheet

from landolt-börnstein - group i elementary particles, nuclei and atoms · volume 17a: "interactions of photons and electrons with atoms" in springermaterials (http://dx.doi.org/10.1007/10547143_3), 2000. accessed 2017-12-09.

[55] R.K. Janev, W.D. Langer, K.J. Evans, and D.E.J. Post. *Elementary Processes in Hydrogen-Helium Plasmas: Cross Sections and Reaction Rate Coefficients*. Springer Series on Atomic, Optical, and Plasma Physics. Springer-Verlag, 1987.

[56] S. J. Buckman, M. Brunger, and M. T. Elford. 6.2 integral elastic cross sections: Datasheet from landolt-börnstein - group i elementary particles, nuclei and atoms · volume 17c: "interactions of photons and electrons with molecules" in springermaterials (http://dx.doi.org/10.1007/10874891_5), 2003. accessed 2017-12-09.

[57] R. K. Janev, D. Reiter, and U. Samm. *Collision processes in low-temperature hydrogen plasmas*, volume 4105 of *Berichte des Forschungszentrums Jülich*. Forschungszentrum, Zentralbibliothek, Jülich, 2003. Record converted from VDB: 12.11.2012.

[58] INTERNATIONAL ATOMIC ENERGY AGENCY. *Atomic and Plasma–Material Interaction Data for Fusion*. Number 8 in Atomic and Plasma–Material Interaction Data for Fusion. INTERNATIONAL ATOMIC ENERGY AGENCY, Vienna, 1999.

[59] H R Skullerud. The stochastic computer simulation of ion motion in a gas subjected to a constant electric field. *Journal of Physics D: Applied Physics*, 1(11):1567, 1968.

[60] J.P. Verboncoeur. Symmetric spline weighting for charge and current density in particle simulation. *Journal of Computational Physics*, 174(1):421 – 427, 2001.

[61] K. Nishida, S. Mattei, S. Mochizuki, J. Lettry, and A. Hatayama. Kinetic modeling of e-to-h mode transition in inductively coupled hydrogen plasmas. *Journal of Applied Physics*, 119(23):233302, 2016.

[62] K Chandrakar. The transition from the first to the second stage of the ring discharge. *Journal of Physics D: Applied Physics*, 11(13):1809, 1978.

[63] A. Ando, T. Matsuno, T. Funaoi, N. Tanaka, K. Tsumori, and Y. Takeiri. H − beam extraction from a cesium seeded field effect transistor based radio frequency negative hydrogen ion source. *Review of Scientific Instruments*, 83(2):02B122, 2012.

[64] D. Wünderlich, P. McNeely, L. Schiesko, U. Fantz, P. Franzen, and NNBI-Team. Modeling the particle transport and ion production in a rf driven negative hydrogen ion source for iter nbi. *AIP Conference Proceedings*, 1515(1):12–21, 2013.

[65] G. Fubiani and J. P. Boeuf. Role of positive ions on the surface production of negative ions in a fusion plasma reactor type negative ion source—insights from a three dimensional particle-in-cell monte carlo collisions model. *Physics of Plasmas*, 20(11):113511, 2013.

[66] F. Taccogna, P. Minelli, and N. Ippolito. Particle model of full-size iter-relevant negative ion source. *Review of Scientific Instruments*, 87(2):02B306, 2016.

[67] K. Miyamoto, S. Okuda, A. Hatayama, M. Hanada, and A. Kojima. Study of beam optics and beam halo by integrated modeling of negative ion beams from plasma meniscus formation to beam acceleration. *Applied Physics Letters*, 102(2):023512, 2013.

[68] Dass Sudhir, M. Bandyopadhyay, and A. Chakraborty. Physics-electrical hybrid model for real time impedance matching and remote plasma characterization in rf plasma sources. *Review of Scientific Instruments*, 87(2):02B312, 2016.

[69] T. Hayami, S. Yoshinari, R. Terasaki, A. Hatayama, and A. Fukano. Analysis of discharge initiation in a rf hydrogen negative ion source. *AIP Conference Proceedings*, 1390(1):339–347, 2011.

[70] S. Mattei, M. Ohta, A. Hatayama, J. Lettry, Y. Kawamura, M. Yasumoto, and C. Schmitzer. Rf plasma modeling of the linac4 h − ion source. *AIP Conference Proceedings*, 1515(1):386–393, 2013.

[71] M. Ohta, S. Mattei, M. Yasumoto, A. Hatayama, and J. Lettry. Numerical study of the inductive plasma coupling to ramp up the plasma density for the linac4 h − ion source. *Review of Scientific Instruments*, 85(2):02B113, 2014.

[72] G. Fubiani and J. P. Boeuf. Plasma asymmetry due to the magnetic filter in fusion-type negative ion sources: Comparisons between two and three-dimensional particle-in-cell simulations. *Physics of Plasmas*, 21(7):073512, 2014.

[73] P Diomede, M Capitelli, and S Longo. Effect of discharge voltage on capacitively coupled, parallel plate rf hydrogen plasmas. *Plasma Sources Science and Technology*, 14(3):459, 2005.

[74] R. CELIBERTO, R.K. JANEV, A. LARICCHIUTA, M. CAPITELLI, J.M. WADEHRA, and D.E. ATEMS. Cross section data for electron-impact inelastic processes of vibrationally excited molecules of hydrogen and its isotopes. *Atomic Data and Nuclear Data Tables*, 77(2):161 − 213, 2001.

[75] K. Nishida, S. Mattei, J. Lettry, and A. Hatayama. Numerical analysis of effects of ion-neutral collision processes on rf icp discharge. *Journal of Applied Physics*, 123(4):043305, 2018.

[76] Mounir Laroussi. Low temperature plasma-based sterilization: Overview and state-of-the-art. *Plasma Processes and Polymers*, 2(5):391–400, 2005.

[77] Cameron M Samuell and Cormac S Corr. Atomic and molecular hydrogen gas temperatures in a low-pressure helicon plasma. *Plasma Sources Science and Technology*, 24(4):045003, 2015.

[78] M Abdel-Rahman, V Schulz von der Gathen, T Gans, K Niemi, and H F Döbele. Determination of the degree of dissociation in an inductively coupled hydrogen plasma using optical emission spectroscopy and laser diagnostics. *Plasma Sources Science and Technology*, 15(4):620, 2006.

[79] M S Benilov. The child–langmuir law and analytical theory of collisionless to collision-dominated sheaths. *Plasma Sources Science and Technology*, 18(1):014005, 2009.

Acknowledgement

Firstly, I would like to express my biggest thank to my supervisor, Professor Akiyoshi Hatayama. His enthusiasm for plasma physics, sincere and passionate attitude about our research, many things have been taught from him. Sometimes discussion with him went too far, which was almost controversy so that I became offensive and rude during the discussion. Nevertheless, he always tried to support me with patience, kindness and passion. No matter how much I appreciate here, it will never be enough to express my thanks for all the things that he has done for me. I should say I was very lucky to have him as a supervisor.

I would like to thank Associate Professor Kohei Yokoi, Professor Kenji Yasuoka and Associate Professor Nobuhiko Nakano of Keio University for their helpful comments. This dissertation would not be accomplished without their help.

The work presented in this dissertation has been carried out with huge supports from CERN people. Dr. Jacques Lettry, my advisor at CERN, gave me many instructions during the internship. It was a great honor to work with him. I was feeling that my experimental skills and knowledge was improving day by day thanks to him. Dr. Stefano Mattei has worked on numerical modeling work with us. His advice often directed my numerical modeling. I would like to thank Dr. Stefan Briefi (of University of Augsburg), Dr. Andy Butterworth, Dr. Alexej Grudiev and all the CERN people, who helped me during my time at CERN. My gratitude also goes to the faculties and the staffs of the Global Environmental System Leaders (GESL) program for giving me such a great opportunity to study at CERN.

My friends and colleagues of Hatayama lab were also indispensable to me. I spent a long time with Mr. Shu Nishioka and Mr. Shohei Yamoto in my PhD life. I am happy that we could finish our PhD together. Mr. Sho Yoshinari, Mr. Takahiro Hayami, Mr. Yasufumi Kawamura, Mr. Masatoshi Yasumoto, Mr. Masatoshi Ohta and Mr. Shintaro Mochizuki are the former lab members who worked on the development of the RF-code. I am grateful for their extensive efforts. My gratitude also goes to all the lab members and former members for making my campus life fruitful.

Lastly, I would like to say many thanks to my family who support me in daily life.

LIST OF PUBLICATIONS

Publications

1. K. Nishida, S. Mattei, J. Lettry and A. Hatayama, "*Numerical analysis of effects of ion-neutral collision processes on RF ICP discharge,*" Journal of Applied Physics, **123**, 043305, 2018.

2. S. Mattei, K. Nishida, M. Onai, J. Lettry, M. Q. Tran and A. Hatayama, "*A fully-implicit Particle-In-Cell Monte Carlo Collision code for the simulation of inductively coupled plasmas,*" Journal of Computational Physics, **350**, 891-906, 2017.

3. K. Nishida, S. Mattei, S. Briefi, A. Butterworth, A. Grudiev, M. Haase, A. Jones, M. Paoluzzi, G. Voulgarakis, A. Hatayama and J. Lettry, "*Experimental Investigation of Plasma Impedance in Linac4 H⁻ Source*", AIP Conference Proceedings, **1869**, 030038, 2017.

4. S. Mattei, K. Nishida, M. Onai, J. Lettry, M. Q. Tran and A. Hatayama, "*Numerical simulation of the RF plasma discharge in the Linac4 H⁻ ion source,*" AIP Conference Proceedings, **1869**, 030018, 2017.

5. D. Rauner, S. Mattei, S. Briefi, U. Fantz, A. Hatayama, J. Lettry, K. Nishida and M.Q. Tran, "*Investigation of the RF-efficiency of inductively coupled hydrogen plasmas at 1 MHz,*" AIP Conference Proceedings, **1869**, 030035, 2017.

6. J. Lettry D. Aguglia, S. Bertolo, S. Briefi, A. Butterworth, Y. Coutron, A. Dallocchio, N. David, E. Chaudet, U. Fantz, D. Fink, M. Garlasche, A. Grudiev, R. Guida, J. Hansen, M. Haase, A. Hatayama, A. Jones, I. Koszar, J.-B. Lallement, A. Lombardi, F. di Lorenzo, C. Machado, C. Mastrostefano, S. Mathot, S. Mattei, P. Moyret, K. Nishida, M. O'Neil, M. Paoluzzi, R. Scrivens, D. Steyaert, N. Thaus, G. Voulgarakis, "*CERN's Linac4 Cesiated Surface H⁻ Source,*" AIP Conference Proceedings, **1869**, 030002, 2017.

7. S. Mattei, K. Nishida, A. Grudiev, J. Lettry, M. Q. Tran and A. Hatayama, "*Kinetic simulations and photometry measurements of the E-H transition in cylindrical inductively coupled plasmas,*" Plasma Sources Science and Technology, **25**, 065001, 2016.

8. <u>K. Nishida</u>, S. Mattei, S. Mochizuki, J. Lettry and A. Hatayama, "*Kinetic Modeling of E-to-H Mode Transition in Inductively Coupled Hydrogen Plasmas,*" Journal of Applied Physics, **119**, 233302, 2016.

9. S. Mochizuki, S. Mattei, <u>K. Nishida</u>, A. Hatayama and J. Lettry, "*Numerical Analysis of Electron Energy Distribution Function and Its Effects on the H^- Production in Linac4 H- Source,*" Plasma and Fusion Research, **11**, 2406044, 2016.

10. T. Shibata, <u>K. Nishida</u>, S. Mochizuki, S. Mattei, J. Lettry, A. Hatayama, A. Ueno, H. Oguri, K. Ohkoshi, K. Ikegami, A. Takagi, H. Asano, and F. Naito, "*Numerical study of plasma generation process and internal antenna heat loadings in J-PARC RF negative ion source,*" Review of Scientific Instruments, **87**, 02B128, 2016.

11. S. Mochizuki, S. Mattei, <u>K. Nishida</u>, A. Hatayama and J. Lettry, "*Analysis of electron energy distribution function in the Linac4 H^- source,*" Review of Scientific Instruments, **87**, 02B108, 2016.

12. J. Lettry, D. Aguglia, J. Alessi, P. Andersson, S. Bertolo, S. Briefi, A. Butterworth, Y. Coutron, A. Dallocchio, N. David, E. Chaudet, D. Faircloth, U. Fantz, D. A. Fink, M. Garlasche, A. Grudiev, R. Guida, J. Hansen, M. Haase, A. Hatayama, A. Jones, I. Koszar, J.-B. Lallement, A. M. Lombardi, C. Machado, C. Mastrostefano, S. Mathot, S. Mattei, P. Moyret, D. Nisbet, <u>K. Nishida</u>, M. O'Neil, M. Paoluzzi, R. Scrivens, T. Shibata, D. Steyaert, N. Thaus, and G. Voulgarakis, "*Linac4 H^- ion sources,*" Review of Scientific Instruments, **87**, 02B139, 2016.

13. A. Butterworth, A. Grudiev, J. Lettry, <u>K. Nishida</u>, M. Paoluzzi and C. Schmitzer, "*RF Low-Level Control for the Linac4 H^- Source,*" AIP Conference Proceedings, **1655**, 030007, 2015.

14. T. Shibata, S.Mattei, <u>K. Nishida</u>, J. Lettry and A. Hatayama, "*Numerical and Experimental Study of Atomic Transport and Balmer line intensity in Linac4 Negative Ion Source,*" AIP Conference Proceedings, **1655**, 020008, 2015.

15. S. Mochizuki, S. Mattei, T. Shibata, <u>K. Nishida</u>, A. Hatayama and J. Lettry, "*Initial results of a full kinetic simulation of RF H^- source including Coulomb collision process,*" AIP Conference Proceedings, **1655**, 020016, 2015.

16. J. Lettry D. Aguglia, J. Alessi, P. Andersson, S. Bertolo, A. Butterworth, Y. Coutron, A. Dallocchio, N. David, E. Chaudet, D. Fink, J. Gil-Flores, M. Garlasche, A. Grudiev, R. Guida, J. Hansen, M. Haase, A. Hatayama, A. Jones, I. Koszar, T. Lehn, C. Machado, C. Mastrostefano, S. Mathot, S. Mattei, Ø. Midttun, P. Moyret, D. Nisbet, <u>K. Nishida</u>, M. O'Neil, M. Paoluzzi, J. Sanchez Alvarez, R. Scrivens, T. Shibata, D. Steyaert, N. Thaus, A. Zelenski, "*CERN's Linac4 H^- Sources: Status*

and Operational Results," AIP Conference Proceedings, **1655**, 030005, 2015.

17. <u>K. Nishida</u>, S. Mochizuki, M. Ohta, M. Yasumoto, J. Lettry, S. Mattei and A. Hatayama, "*Equivalent circuit of radio frequency-plasma with the transformer model,*" Review of Scientific Instruments, **85**, 02B117, 2014.

18. J. Lettry, D. Aguglia, P. Andersson, S. Bertolo, A. Butterworth, Y. Coutron, A. Dallocchio, E. Chaudet, J. Gil-Flores, R. Guida, J. Hansen, A. Hatayama, I. Koszar, E. Mahner, C. Mastrostefano, S. Mathot, S. Mattei, Ø. Midttun, P. Moyret, D. Nisbet, <u>K. Nishida</u>, M. O'Neil, M. Ohta, M. Paoluzzi, C. Pasquino, H. Pereira, J. Rochez, J. Sanchez Alvarez, J. Sanchez Arias, R. Scrivens, T. Shibata, D. Steyaert, N. Thaus and T. Yamamoto, "*Status and operation of the Linac4 ion source prototypes,*" Review of Scientific Instruments **85**, 02B122, 2014.

19. T. Yamamoto, T. Shibata, M. Ohta, M. Yasumoto, <u>K. Nishida</u>, A. Hatayama, S. Mattei, J. Lettry, K. Sawada and U. Fantz, "*Modeling of neutrals in the Linac4 H^- ion source plasma: Hydrogen atom production density profile and H_α intensity by collisional radiative model,*" Review of Scientific Instruments **85**, 02B118, 2014.

20. A. Hatayama, T. Shibata, S. Nishioka, M. Ohta, M. Yasumoto, <u>K. Nishida</u>, T. Yamamoto, K. Miyamoto, A. Fukano and T. Mizuno, "*Kinetic modeling of particle dynamics in H^- negative ion sources,*" Review of Scientific Instruments, **85**, 02A510, 2014.